# Strain-Rate Effects in Quartz Sand

Andrew D. Barr MEng

*Thesis submitted to*

The University of Sheffield
Department of Civil and Structural Engineering

*for the degree of*

Doctor of Philosophy

August 2016

# Abstract

Soil-filled wire and geotextile gabions are commonly used to construct defensive infrastructure in military bases, where the attenuating properties of soil are used to protect personnel and key assets from the effects of blast and fragmentation. The behaviour of soils in these extreme loading regimes is not well understood, and so designers require data at these high pressures and strain rates in order to develop robust soil constitutive models and adapt to new threats.

The one-dimensional compression of three sandy soils was compared under quasi-static loading to axial stresses of 800 MPa. Trends in behaviour were identified with respect to the particle size distributions of the soils, and were found to correspond to the relationships observed at lower stresses. Split Hopkinson pressure bar (SHPB) experiments were used to investigate the strain rate dependence of this behaviour. Measurements of radial stress indicated that an increase in the axial stiffness of the soils between strain rates of $10^{-3}\,s^{-1}$ and $10^{3}\,s^{-1}$ was likely due to radial inertial effects.

Potential sources of error were identified in the SHPB experiments, leading to the implementation of a dispersion-correction algorithm, which improved the measurement of axial stresses. Analysis of the electromagnetic activity around the specimen isolated the cause of erroneous radial stress measurements.

Quasi-static experiments were used to investigate the effect of moisture content on soil stiffness at high pressures, and SHPB experiments at the same moisture contents were used to consider the effect of strain rate on the quasi-static behaviour. Recovery SHPB experiments were designed to enable reliable post-test particle size analyses to be performed, and the range of moisture contents was expanded to investigate the change in soil behaviour on reaching full saturation.

Reduced triaxial compression experiments were used to define the yield surface of a sand to a mean stress of 400 MPa. The high-pressure compression and yield strength data was used to calibrate LS-DYNA soil models, and the performance of the models was assessed through modelling of the SHPB experiments.

# Acknowledgements

This might be harder to keep to one page than the abstract...

Firstly, thank you to my supervisor, Dr Sam Clarke, whose generous support and friendship has made this research a genuinely enjoyable and rewarding experience. Few students are lucky enough to have a supervisor so interested in their work and dedicated to their development as a researcher.

I am also thankful to Dr Mihail Petkovski, Professor Andy Tyas and Alan Hindle, whose guidance and technical input made the experiments in this thesis possible. Andy is additionally responsible for my growing obsession with dispersion (see Chapter 4) – this is more an assignment of blame than a thank you.

My CASE studentship was sponsored by Blastech Ltd., and in particular I'm grateful to Dr Jim Warren for the value added to my studies by involvement in and exposure to blast and impact research in a broader form. Thanks also to the technical staff at Blastech, who accommodated and aided my experimental work on many occasions.

The Blast and Impact Dynamics group may be new, but it has a strong starting line up. Thank you to Sam for LS-DYNA help and many productive conversations, to Ben for many productive distractions, and to Kit for many productive days of desk sharing. Thank you also to Nicola for making me feel like a table football superstar.

For the hours not spent in the University, I am immensely grateful for the support of family, friends and my wonderful wife, Alannah. Spending time with you makes life worth living.

Finally, thank you to Steve and the team at Hasbean. Because life's too short for bad coffee.

*Andrew Barr*
*18$^{th}$ August 2016*

# Contents

# List of Figures

# List of Tables

# List of symbols

*Subscripts for stress, strain and displacement*

| | |
|---|---|
| 0 | Initial condition |
| 1, 2 | Related to the front and back bar–specimen interfaces in SHPB experiments |
| $i$, $r$, $t$ | Related to the incident, reflected and transmitted waves in SHPB experiments |
| $r$, $\theta$, $a$ | Radial, circumferential and axial directions in cylindrical coordinates |
| $s$ | Related to the bulk specimen response in SHPB experiments |
| $v$ | Volumetric (strain) |
| $x$, $y$, $z$ | Principal directions in Cartesian coordinates |

*Greek alphabet*

| | |
|---|---|
| $\gamma$ | Wave number, $2\pi/\lambda$ |
| $\varepsilon$ | Strain |
| $\dot{\varepsilon}$ | Strain rate |
| $\lambda$ | Wavelength |
| $\nu$ | Poisson's ratio |
| $\rho$ | Bulk density |
| $\rho_d$ | Dry density |
| $\rho_s$ | Particle density |
| $\sigma$ | Stress |
| $\sigma'$ | Effective stress |
| $\tau$ | Shear stress |
| $\phi$ | Angle of shearing resistance |
| $\Phi_B$ | Magnetic flux |
| $\psi$ | Angle of dilation |
| $\omega$ | Angular frequency |

*Latin alphabet*

| | |
|---|---|
| $a$ | Bar radius |
| $A$ | Area (Amplitude in §4.2) |
| $B$ | Magnetic field strength |
| $c$ | Velocity |
| $c'$ | Cohesion intercept |
| $c_0$ | One-dimensional elastic wave speed |
| $c_\omega$ | Phase velocity |
| $d$ | Diameter |
| $e$ | Void ratio ($V_v/V_s$) |
| $E$ | Young's modulus |
| $\mathscr{E}$ | Electromotive force (EMF) |
| $f$ | Frequency |
| $F$ | Gauge factor |
| $G$ | Shear modulus |
| $i$ | Imaginary unit |
| $I_3$ | Third stress invariant |
| $J_0$ | Bessel function of the first kind, order 0 |
| $J_1$ | Bessel function of the first kind, order 1 |
| $J_2$ | Second deviatoric invariant |
| $J_3$ | Third deviatoric invariant |
| $K$ | Bulk modulus |
| $l$ | Length |
| $M$ | Constrained modulus ($\sigma_a/\varepsilon_a$ when $\varepsilon_r = 0$) |
| $M_s$ | Mass of soil |
| $M_w$ | Mass of water |
| $p$ | Mean principal stress |
| $P$ | Pressure |
| $q$ | Deviator stress |
| $r$ | Radius |
| $S_r$ | Saturation ratio ($V_w/V_v$) |
| $t$ | Time |
| $u$ | Pore pressure |
| $u, v, w$ | Displacements in x, y and z directions in Cartesian coordinates |
| $V$ | Volume (Voltage in §2.3) |
| $V_s$ | Volume of solids |
| $V_v$ | Volume of voids |
| $V_w$ | Volume of water |
| $w$ | Moisture content ($M_w/M_s$) |

Chapter 1

# Introduction

## 1.1 Background

This research forms part of the Dstl-sponsored and QinetiQ-led Force Protection Engineering (FPE) research programme, which investigates protective materials and structures that can be used by military fortifications designers (Warren et al. 2013). The Underpinning Research element of this programme aims to enhance the understanding of how materials used in FPE perform under a wide range of loading conditions. FPE structures are currently designed through a combination of traditional engineering design, numerical simulation and experimental trials, but full-scale trials with explosives and firearms can be expensive and time-consuming. One of the goals of the FPE programme is to sufficiently understand the protective materials, and develop sufficiently robust material models, so that solutions can be designed to defend against future threats quickly and cost-effectively.

Soil-filled wire and geotextile gabions (Hesco Concertainers) are commonly used to construct perimeter walls and other defensive infrastructure in military bases, where they serve to protect personnel and key assets from the effects of blast and fragmentation. The attenuating properties of soil make it a highly effective defence against such threats, and as it is readily available in many locations, large structures can be erected at relatively low cost. However, 'soil' is an incredibly variable material, and its high-strain-rate behaviour is not well understood. In addition, properties such as moisture content, particle size distribution, particle shape, mineralogy and initial porosity can greatly affect a soil's mechanical properties, and hence its protective ability. In order to develop robust constitutive models to adapt to new soils and new threats, fortifications designers require high-pressure data on the behaviour of soils over a wide range of strain rates and ground conditions.

## 1.2 Scope and objectives

A fortifications designer building in a new location will require data which is representative of the local soil in order to calibrate the constitutive model. The natural variability of soils would make it very difficult and time-consuming to characterise all possible soils, and so this study focuses on the most commonly encountered soil type: quartz sands. The main aim of this study is to provide quantitative information on the mechanical behaviour of three sandy soils under intense loading. The selected particle size distributions will additionally enable a qualitative extrapolation to the behaviour of soils outside the examined range.

Blast events and fragment impacts on soil structures involve both compaction and shearing of the soil, and a constitutive model will need to represent both of these behaviours, neither of which are currently well-defined at the high pressures and strain rates required. This thesis is primarily concerned with the effects of strain rate and moisture content on the compaction behaviour of soils, although a novel methodology for the definition of high-pressure yield surfaces is also introduced in Chapter 6.

The main aims of this thesis are therefore:

- To compare the high-pressure, quasi-static compaction behaviour of sandy soils with respect to their varying particle size distributions;
- To investigate whether a strain-rate dependence alters this behaviour at high strain rates; and
- To quantify the effect of changing moisture content on this behaviour.

## 1.3 Thesis outline

The remainder of this thesis is organised into chapters as follows:

**Chapter 2: Literature review**

This chapter presents an overview of published literature relevant to the study of strain rate effects in soils. The main variables which affect the quasi-static and high-strain-rate behaviour of sand under one-dimensional compression are identified, and high-strain-rate testing is introduced with a discussion of the split Hopkinson pressure bar. Existing numerical models of dynamic events in soils are also discussed.

**Chapter 3: Strain-rate dependence in three sandy soils**

High-pressure quasi-static and high-strain-rate experiments are designed and implemented to investigate the effect of strain rate and moisture content on the behaviour of three sandy soils. The results are analysed in terms of the compressibility of the dry soils under quasi-static loading, the effect of strain rate on the behaviour the dry soils, and the effect of moisture content on the strain-rate sensitivity of the medium sand.

**Chapter 4: Dispersion and electromagnetic effects on SHPB measurements**

This chapter discusses sources of error in the analysis of SHPB experiments which were highlighted in Chapter 3. The effects of dispersion in pressure bar signals are analysed, and a first-mode correction algorithm is implemented, which is shown to improve the interpretation of specimen stresses significantly. The effect of electromagnetic activity on radial stress measurements is also investigated.

**Chapter 5: Recovery tests on medium sand**

The SHPB experiments in Chapter 3 are developed to allow recovery of the specimen after a single stress pulse, enabling the effect of moisture content on particle breakage to be analysed. Moisture contents are chosen so that some specimens reach full saturation during the experiment, allowing the effect of pore water loading to be analysed.

**Chapter 6: High-pressure compression and yield strength data for numerical modelling**

The mac$^{2T}$ apparatus is used to provide high-pressure compaction and yield surface data for the calibration of soil models. Data generated for a sand is used to assess the ability of the 'soil' models in finite-element code LS-DYNA, and validation experiments are performed by modelling the split Hopkinson pressure bar experiments.

**Chapter 7: Conclusions and future work**

This chapter summarises the main conclusions of the current work, and identifies opportunities for further research.

Chapter 2

# Literature review

## 2.1 Introduction

This chapter presents an overview of published literature relevant to the study of strain rate effects in soils. This includes a description of the main experimental methods used in high-strain-rate testing, with particular focus on the use and experimental limitations of the split Hopkinson pressure bar. A discussion of existing experimental work is then provided, focussing on variables which affect the quasi-static and high-strain-rate behaviour of sand under one-dimensional compression, and highlighting investigations which directly consider strain-rate effects. The use of numerical modelling in developing and utilising material models for soils at high strain rates is introduced, particularly in relation to the finite-element code LS-DYNA, along with a review of key examples from the literature. A final summary relates the state-of-the-art in the published literature to the current work.

## 2.2 Strain rate

Modelling the response of materials during blast and impact events requires an understanding of how they behave over a wide range of strain rates, as the rate of deformation can bring about different modes of material response. For example, metals such as copper, aluminium and magnesium exhibit a significant increase in yield strength at high strain rates (Davies and Hunter 1963). Approximate definitions of various strain-rate regimes are represented in Figure 2.1, which also provides examples of phenomena which might occur in soils over this range; these definitions will be used to refer to strain-rate regimes throughout this work.

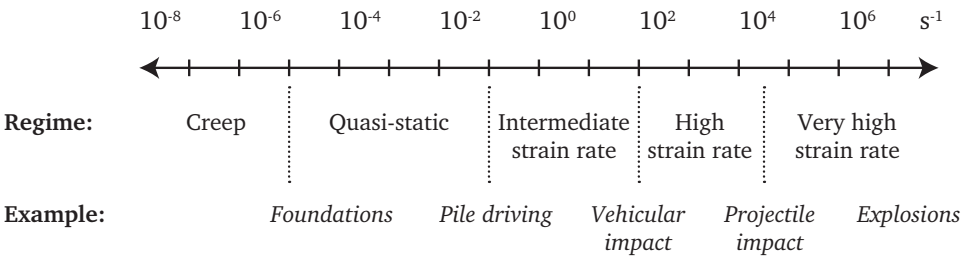


**Figure 2.1:** Strain rate regimes and examples of phenomena in soils.

Most civil engineering applications of soils reside in the creep and quasi-static strain-rate regimes ($<10^{-1}\,s^{-1}$), where the system can be assumed to be in stress equilibrium. Increments of compressive stress can be provided by a hydraulic loading frame or simple masses, and accurate measurements of stress and strain are easily made. The strain rates associated with low-velocity impacts ($10^{-1}\,s^{-1}$ to $10^{2}\,s^{-1}$) can be achieved using specialised hydraulic frames or a drop weight apparatus. While measurements of stress and strain remain relatively simple at these strain rates, the onset of inertial effects means that care must be taken in analysing the data.

Testing at the high strain rates characteristic of blast and impact events has required the development of specialised experimental methods, as the aggressive test conditions and the transient nature of the loading make the use of conventional measurement techniques difficult. High-strain-rate conditions ($10^{2}\,s^{-1}$ to $10^{4}\,s^{-1}$) involve events which are so rapid that the propagation of stress waves through the material becomes important. Such conditions are often achieved experimentally using the split Hopkinson pressure bar (SHPB), which is one of the focuses of this work and is explained in detail in the next section. Very high strain rates ($>10^{4}\,s^{-1}$) can be achieved a using flyer plate experiments, where the impact of a high-velocity flyer can be intense enough to set up a shock wave in the specimen.

## 2.3 Split Hopkinson pressure bar

The modern SHPB technique is named after Bertram Hopkinson, who developed a method for measuring the pressure produced by the impact of bullets or the detonation of explosives (Hopkinson 1914). In the original Hopkinson pressure bar, the pressure from the impact or explosion was transmitted along a long steel bar and passed into a shorter bar acting as a momentum trap, whose movement could be used to infer the magnitude and duration of the pressure wave.

This technique was developed further by Davies (1948), who fitted a single bar with a condenser unit connected to a cathode-ray oscilloscope to record the movement of the bar with time, and developed the theory of stress wave propagation in bars to include dispersive effects (see §2.3.3). Kolsky (1949) used two such bars in series with a material specimen placed between them, so that when a transient pressure was applied at one end of the system the stress pulse in each bar could be recorded, and the dynamic stress–strain response of the specimen deduced. While the condenser units are now usually replaced by semiconductor strain gauges, the experimental basis of this system of two Hopkinson pressure bars—the split Hopkinson pressure bar or Kolsky bar—remains unchanged in modern compression SHPB setups.

The following sections describe the methodology of compression SHPB tests, how data from the tests is processed and interpreted, and the experimental assumptions this analysis is based on.

### 2.3.1 Methodology and theory

An idealised compression SHPB test is depicted in Figure 2.2. The specimen is placed between two long, cylindrical bars held in linear bearings, termed the incident and transmitter bars, then a stress pulse is applied by firing a shorter striker bar onto the end of the incident bar. It is ensured that the stress pulse does not exceed the proportional limit of the pressure bars, so that only elastic waves are produced. To measure the longitudinal stress waves generated during the test, the bars are fitted with strain gauges connected to a Wheatstone bridge circuit, the output of which is recorded by an oscilloscope. The length of the bars and the position of the strain gauges is chosen so that stress pulses do not overlap at the point of recording.

The events of the test are described below with reference to Figure 2.2, where it will be assumed that all bars are of the same material, and that the bars and specimen have the same diameter.

1) When the striker bar impacts the end of the incident bar, a compressive stress wave is formed, propagating to the right in the incident bar, and to the left in the striker bar. When the left-going stress wave in the striker bar reaches the free surface at its left face, it is reflected as a tension wave of the same magnitude, reducing the stress in the bar to zero and relieving the compressive contact between the striker and incident bars. The result is a right-going compressive stress wave which is twice the length of the striker bar.

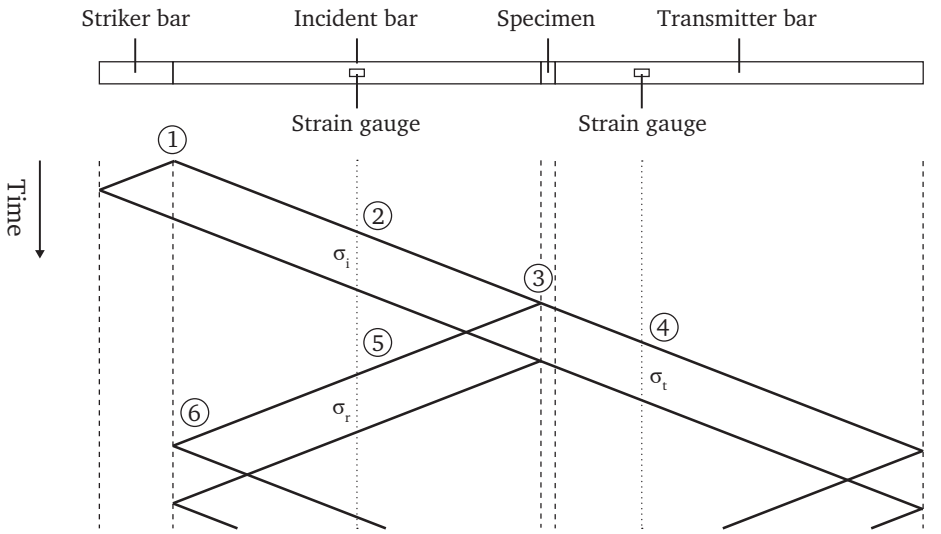


**(a)**

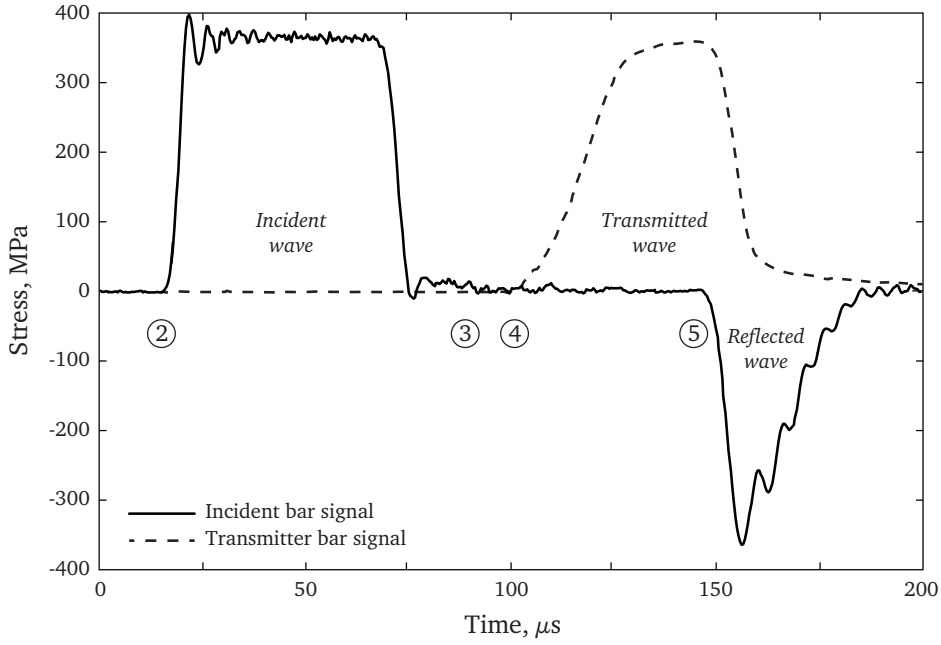


**(b)**

**Figure 2.2:** Stress waves in a split Hopkinson pressure bar test: a) Lagrange diagram of wave propagation and interactions, b) Typical strain gauge signals for a SHPB test on sand.

2) This compressive pulse continues along the incident bar, and is detected by the strain gauge. This is the incident wave, $\sigma_i$.

3) When the incident wave arrives at the interface between the incident bar and the specimen, part of the wave continues into the specimen and part is reflected at the surface in tension. These are the transmitted wave, $\sigma_t$, and reflected wave, $\sigma_r$, respectively. The magnitudes of the transmitted and reflected waves depends on the relative impedance, $\rho c_0$, of the bars and specimen.

4) The transmitted wave continues through the specimen and into the transmitter bar, where the stress wave is detected by the strain gauge.

5) The reflected wave propagates back down the incident bar and is detected by the strain gauge.

6) At this point all the information needed for the experiment has been collected, though the stress waves will continue to oscillate up and down the bars.

The stress pulses measured in the bar during the experiment can be used to infer the stress and strain histories of the two ends of the specimen by using one-dimensional elastic wave theory, which assumes that the stress waves in the bar propagate as longitudinal waves with velocity $c_0 = \sqrt{E/\rho}$ (Kolsky 1963).

Consider the propagation of an elastic stress wave along a dimension $x$ in a bar with density $\rho$ and Young's modulus $E$. Taking a small length of the bar, $\delta x$, if the stress on one face is $\sigma_x$ the stress on the other face will be $\sigma_x + (\partial \sigma_x / \partial x)\delta x$. If the resulting displacement is $u$, then using Newton's second law of motion

$$A \frac{\partial \sigma_x}{\partial x} \delta x = \rho A \, \delta x \cdot \frac{\partial^2 u}{\partial t^2} \tag{2.1}$$

As the bar is behaving elastically, this can be rearranged to give the one-dimensional wave equation

$$\rho \frac{\partial^2 u}{\partial t^2} = E \frac{\partial^2 u}{\partial x^2} \tag{2.2}$$

Recalling that all waves are assumed to travel at a velocity $c_0 = \sqrt{E/\rho}$, this equation can also be expressed as

$$\frac{\partial^2 u}{\partial t^2} = c_0^2 \frac{\partial^2 u}{\partial x^2} \tag{2.3}$$

The general solution to the partial differential equation can be expressed as

$$u = f(x + c_0 t) + g(x - c_0 t) \tag{2.4}$$

where $f$ and $g$ are functions corresponding to waves travelling with negative and positive velocity, respectively. Taking the example of a wave travelling in the direction of decreasing $x$, $u = f(x + c_0 t)$, and differentiating with respect to $x$ and $t$:

$$\frac{\partial u}{\partial x} = f'(x + c_0 t) \tag{2.5}$$

$$\frac{\partial u}{\partial t} = c_0 f'(x + c_0 t) \tag{2.6}$$

and so, combining Equations 2.5 and 2.6,

$$\frac{\partial u}{\partial t} = c_0 \frac{\partial u}{\partial x} \tag{2.7}$$

Since $\partial u / \partial x$ refers to elastic strains, Equation 2.7 can be expressed in terms of stress:

$$\frac{\partial u}{\partial t} = c_0 \left( \frac{\sigma_x}{E} \right) = \frac{\sigma_x}{\rho c_0} \tag{2.8}$$

where it is shown that particle velocity varies linearly with stress. The time integral of this expression then provides the displacement of the bar:

$$u = \frac{1}{\rho c_0} \int_0^t \sigma_x \, \mathrm{d}t \tag{2.9}$$

To find the stresses acting at the bar ends, the signals recorded by the strain gauges are translated along the time axis by a time

$$t_{\text{shift}} = \frac{l_{\text{offset}}}{c_0} \tag{2.10}$$

where $l_{\text{offset}}$ is distance from the strain gauge to the specimen end of the bar. At the incident bar–specimen interface the stress in the bar can be found through superposition of the incident and reflected waves

$$\sigma_1 = \sigma_i + \sigma_r \tag{2.11}$$

while at the specimen–transmitter bar interface the stress in the bar depends only on the transmitted wave

$$\sigma_2 = \sigma_t \tag{2.12}$$

The mean axial stress along the length of the specimen is then

$$\sigma_s = \frac{\sigma_1 + \sigma_2}{2} \tag{2.13}$$

From Equation 2.9 the displacements of the incident and transmitter bars at the specimen interfaces are

$$u_1 = \frac{1}{\rho c_0} \int_0^t \sigma_i + \sigma_r \, \mathrm{d}t \tag{2.14}$$

$$u_2 = \frac{1}{\rho c_0} \int_0^t \sigma_t \, \mathrm{d}t \tag{2.15}$$

As the specimen is confined between the two bars, the mean axial strain along the length of the specimen can be found as

$$\varepsilon_s = \frac{u_1 - u_2}{l_{s,0}} \tag{2.16}$$

where $l_{s,0}$ is the original length of the specimen. There is now sufficient information to describe the axial stress–axial strain response of the specimen.

### 2.3.2 Limitations of the SHPB method

Interpretation of the results from a SHPB experiment, as described above, assumes that stresses and strains occur uniformly along the length of a specimen; in reality, propagation of the stress wave through the specimen is hindered by axial and radial inertia, so that the stresses acting at its ends are prevented from equalising. This is an important consideration in soils, where the wave speed is on the order of $300\,\mathrm{m\,s^{-1}}$, an order of magnitude lower than the $5000\,\mathrm{m\,s^{-1}}$ common in steel pressure bars: the low wave velocity, and the attenuation associated with compressibility, can lead to large stress differences along the length of the specimen (Felice 1986).

If the time taken for the wave to travel through the specimen is small in comparison to the length of the stress pulse being applied, many reflections can take place within the specimen during the experiment, so that stress equilibrium can be achieved. A short transit time can be ensured by reducing the length of the specimen. Song and Chen (2004) tested rubber specimens of varying lengths and observed that stress equilibrium improved as the specimen length was decreased, as demonstrated in Figure 2.3. For soils in particular, Felice et al.

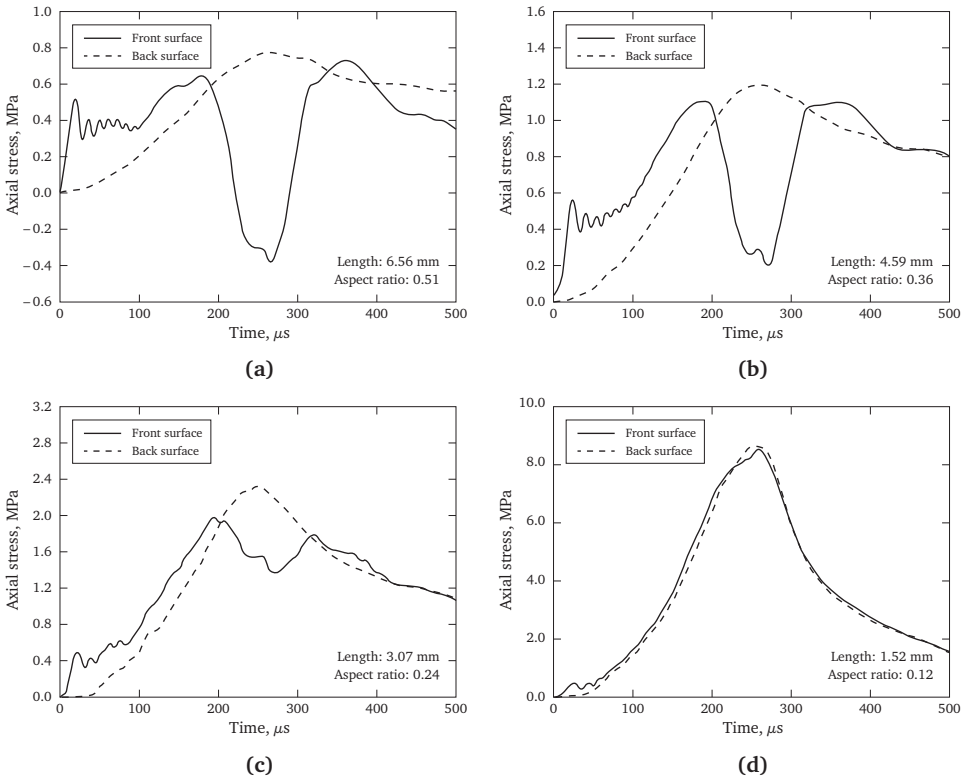


**Figure 2.3:** The effect of specimen length on stress equilibration in SHPB tests on silicone rubber (Song and Chen 2004).

(1987) concluded that a specimen aspect ratio (length:diameter) of 0.2 would satisfy the assumption of stress uniformity.

An alternative solution to achieve stress equilibrium is to change the shape of the incident pulse so that the leading edge ramps up more gradually. This was the method used by Nemat-Nasser et al. (1991) and Frew et al. (2005), who placed thin metallic disks between the striker and incident bars. The striker bar impact caused the disks to deform plastically, increasing the rise time of the incident pulse.

A further consideration in SHPB experiments is the presence of friction effects between the pressure bars and the specimen. If present, a specimen tested in uniaxial compression will appear to be stiffer, as work will have to be done to overcome the friction at the bar–specimen interface. This lateral restraint will also cause the specimen to barrel rather than deforming uniformly along its length, complicating interpretation of the experimental results (Gray III 2000). Cohesionless soils are usually laterally restrained during SHPB tests using a rigid cylinder or ring, which prevents barrelling, but has the potential to introduce

an axial friction effect. Felice et al. (1987) conducted confined SHPB tests on clayey silty sand, and concluded that lateral friction effects did not significantly affect the stress–strain response of the specimens. Through variation of the specimen length they also observed that at an aspect ratio of 0.2 the confining cylinder did not introduce significant axial friction effects.

### 2.3.3 Limitations of one-dimensional wave theory

As mentioned previously, one-dimensional wave theory assumes that all longitudinal waves in the bar propagate at a velocity $c_0$. The theory also requires that plane transverse sections of the bar remain plane, and that stresses act uniformly across these sections. As a wave passes along a bar, however, the bar will expand and contract radially with compressive and tensile axial strains in keeping with the bar's Poisson's ratio. This radial motion affects the distribution of stresses over the bar cross-section, so that plane sections become distorted (Kolsky 1963).

The effect of this deviation from the idealised conditions can be observed from the three-dimensional wave equations derived by Pochhammer (1876) and Chree (1889), which were applied to the case of longitudinal waves in a cylindrical bar by Bancroft (1941). Rather than travelling uniformly at a velocity $c_0$, longitudinal waves were shown to propagate at a specific phase velocity $c_\omega$, which is a function of wavelength and the bar's diameter, one-dimensional wave speed and Poisson's ratio:

$$(x-1)^2\varphi(ha)-(\beta x-1)[x-\varphi(ka)]=0 \tag{2.17}$$

where

$$\begin{aligned}
\beta &= (1-2\nu)/(1-\nu)\\
x &= (c_\omega/c_0)^2(1+\nu)\\
h &= \gamma(\beta x-1)^{\frac{1}{2}}\\
k &= \gamma(2x-1)^{\frac{1}{2}}\\
\varphi(y) &= yJ_0(y)/J_1(y)
\end{aligned}$$

$$\begin{aligned}
c_\omega &\;-\; \text{Phase velocity}\\
c_0 &\;-\; \text{One-dimensional elastic wave velocity}\\
a &\;-\; \text{Bar radius}\\
\nu &\;-\; \text{Poisson's ratio}\\
\gamma &\;-\; \text{Wave number, } 2\pi/\lambda\\
\lambda &\;-\; \text{Wavelength}\\
J_n(y) &\;-\; \text{Bessel function of the first kind, of order } n
\end{aligned}$$

This equation has an infinite number of roots corresponding to different modes of propagation in the bar, the first three of which are shown in Figure 2.4. This relationship shows that while low-frequency waves propagate at approximately $c_0$, the phase velocity decreases with increasing frequency, particularly when the wavelength is approximately equal to the diameter of the bar.

The complex waveforms produced during a SHPB experiment contain a broad spectrum of frequency components, and the consequence of this frequency-dependence is that the stress wave disperses as it propagates down the bar. This effect is shown in Figure 2.5, which depicts the dispersion of a trapezoidal wave in a stainless steel pressure bar. The high-frequency wave components associated with the 'sharp' features in the signal lag behind the low-frequency components, so that the sharp features become rounded and oscillations are introduced to parts of the signal which were previously linear.

Dispersion of the stress pulse is accompanied by a frequency-dependent variation in stress and strain across the bar cross-section (Davies 1948). As shown in Figure 2.6, as the frequency of the forcing function increases strains measured on the bar surface decrease with respect to the strain at the bar axis. At high frequencies the axial strain on the bar surface becomes very small, and at even higher frequencies is of the opposite sign to the strain at the bar axis, imposing a limit on the frequencies which can be measured using surface strain gauges.

As a result of these effects, a signal recorded on the surface of the bar at some distance from the specimen will not accurately describe the specimen response, and so a number of authors have developed methods of correcting pressure bar signals to account for this. Gorham (1983) used the fast Fourier transform (FFT) to convert strain signals into the frequency domain, where the phase angle of each Fourier component could be corrected based on the phase velocity derived from the Pochhammer–Chree equations. Tyas and Watson (2001) extended this method to account for the stress variation over the bar cross-section by applying an additional correction to the amplitude of each Fourier component. Such corrections currently assume that all waves propagate in the first mode, but have been shown to offer a significant improvement in timeshifting signals over the frequency-independent assumptions made in one-dimensional wave theory (Tyas and Pope 2005).

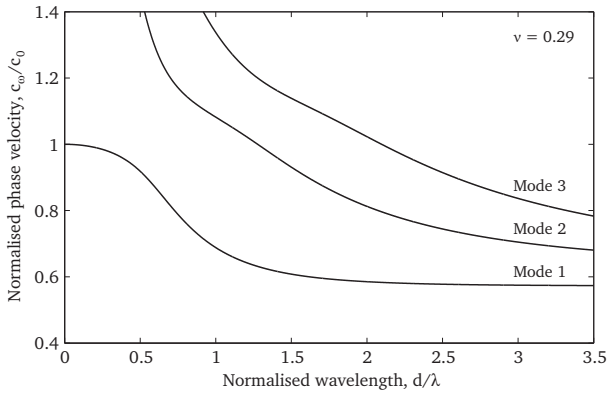


**Figure 2.4:** Relationship of phase velocity to wavelength for the first three modes of propagation of a longitudinal wave in a cylindrical bar for $\nu = 0.29$.

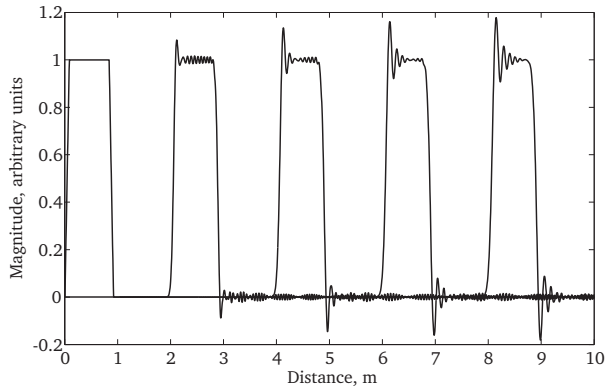


**Figure 2.5:** Dispersion of a trapezoidal wave in a cylindrical steel pressure bar. Recordings are shown at 2 m increments.

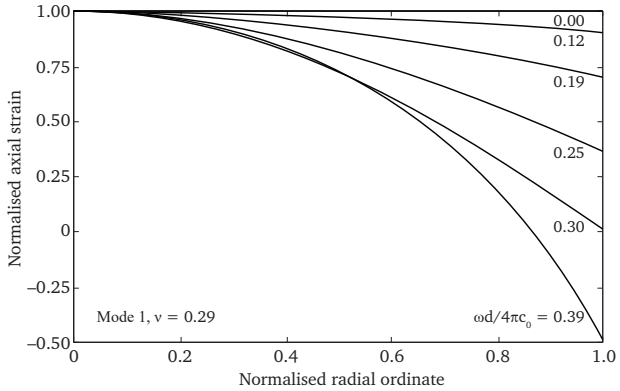


**Figure 2.6:** Distribution of axial strain over bar cross section for an infinite duration single-frequency forcing function, after Tyas and Watson (2000).

## 2.4 One-dimensional compression of sand

The individual particles which make up an engineering soil can exist in a very wide range of sizes, from a fraction of a micrometre to over a metre, as shown in Table 2.1. This study is particularly concerned with sandy soils, where the majority of the particles fall into the range 0.063 mm to 2.0 mm. Even within this narrow range, the particle size distribution and the shape, angularity and surface roughness of the particles in sandy soils can vary greatly: as most soils are formed through the repeated fracture of rocks by weathering and chemical processes, these properties will depend on the soil's mineral origin and the fracture and transport processes which have acted on it.

The most common mineral constituent of sands is silica, usually in the form of quartz ($SiO_2$), though carbonate ($CaCO_3$) sands are common in coastal areas where coral and shellfish are prevalent. The surface of sand particles may also be coated with traces of other minerals such as calcite, limonite or iron oxides, while clay fractions can introduce other silica-based minerals such as kaolinite, montmorillonite and illite (Powrie 2013).

The mineral particles which make up a soil are surrounded by void spaces, which are usually filled with air, water or a mixture of the two. The proportion of parts of this three-phase system can be expressed using the soil properties of void ratio $e$, moisture content $w$ and saturation ratio $S_r$ (Atkinson and Bransby 1978):

$$\text{Void ratio, } e = \frac{\text{Volume of voids}}{\text{Volume of solids}} = \frac{V_v}{V_s} \tag{2.18}$$

$$\text{Moisture content, } w = \frac{\text{Mass of water}}{\text{Mass of solids}} = \frac{M_w}{M_s} \tag{2.19}$$

$$\text{Saturation ratio, } S_r = \frac{\text{Volume of water}}{\text{Volume of voids}} = \frac{V_w}{V_v} \tag{2.20}$$

Void ratio is particularly useful as a normalised measure of compaction in soils, as a void ratio of 0 corresponds to a soil where all void spaces have been closed, and the density is that of the constituent mineral.

| *Soil type* | *Fraction* | *Subfraction* | *Particle size, mm* |
|---|---|---|---|
| Very coarse soil | Boulders | Large boulder | $> 630$ |
| | | Boulder | $200 - 630$ |
| | Cobbles | | $63 - 200$ |
| Coarse soil | Gravel | Coarse gravel | $20 - 63$ |
| | | Medium gravel | $6.3 - 20$ |
| | | Fine gravel | $2.0 - 6.3$ |
| | Sand | Coarse sand | $0.63 - 2.0$ |
| | | Medium sand | $0.2 - 0.63$ |
| | | Fine sand | $0.063 - 0.2$ |
| Fine soil | Silt | Coarse silt | $0.02 - 0.063$ |
| | | Medium silt | $0.0063 - 0.02$ |
| | | Fine silt | $0.002 - 0.0063$ |
| | Clay | | $\leq 0.002$ |

**Table 2.1:** Particle size fractions, from EN ISO 14688–1:2002

### 2.4.1 Quasi-static behaviour

One-dimensional compression of soils refers to loading states where strains are only permitted in the direction of the applied stress. An increase in stress in the soil is initially accommodated through the deformation and rearrangement of the soil particles, then, where the particle strength is exceeded, fracture and further rearrangement. Particle rearrangement becomes more difficult as the void ratio decreases, so that the soil becomes stiffer as it is compressed. In the standard geotechnical model, the relationship between the logarithm of effective stress and void ratio form a straight line at higher stresses: this normal compression line (NCL) is shown in Figure 2.7, where the transition onto the NCL has been related to the onset of particle breakage, which increases with stress (Fukumoto 1992, McDowell 2002). During unloading and reloading, only the deformation of the particles changes, so that the soil behaves more stiffly, but in a largely elastic manner: loading along the NCL is therefore mainly plastic. The NCL and the unloading lines have slopes of $-C_c$ and $-C_s$ respectively, where $C_c$ is the soil's compression index and $C_s$ is the swelling index (Wood 1990).

The stresses produced in blast and impact events are much higher than those in most civil engineering applications, so that particle crushing is more likely to be a major feature of the compression process. Hagerty et al. (1993) tested dry sand to axial stresses of 689 MPa and noted three distinct phases of compression behaviour: 1) particle rearrangement at low stresses, 2) particle crushing and rearrangement at higher stresses, 3) a reduction in particle crushing at very

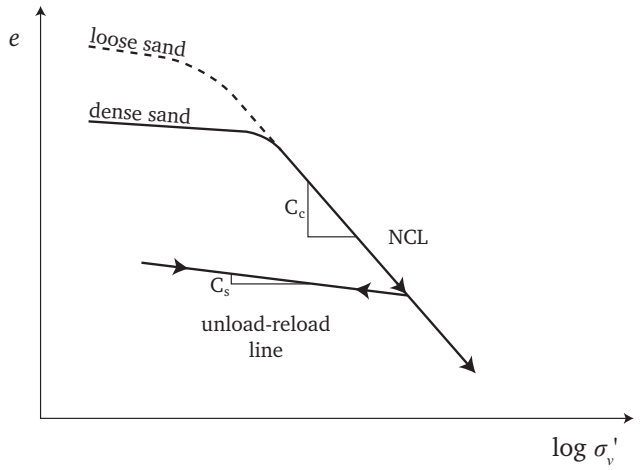


**Figure 2.7:** One-dimensional compression of sand in $e$–$\log \sigma'_v$ space.

high stresses (see Figure 2.8b). This third phase caused the sand response to stiffen to the right of the idealised NCL, and was related to the large number of small particles increasing the number of contacts each particle had with its neighbours (its coordination number), reducing particle shear stresses.

The effect of stress on particle crushing was also investigated at lower stresses by McDowell et al. (1996), who proposed that the relationship of void ratio with the logarithm of stress was due to the development of a fractal particle size distribution. A model was developed where particle strength was determined probabilistically, the likelihood of breakage increasing with stress but decreasing as the coordination number increased. Ben-Nun and Einav (2010) and McDowell and de Bono (2013) have confirmed the development of a fractal geometry in both well- and poorly-graded granular media using discrete-element modelling.

Crushing strength is a function of particle size, so that finer soils exhibit less breakage, and the effect of the coordination number means that less particle breakage occurs in well graded soils than in poorly graded soils (McDowell et al. 1996). Hagerty et al. (1993) showed that the compaction responses of initially loose and dense specimens of the same sand converge on the NCL, with particle breakage initiating in loose soils at lower stresses. For glass specimens, this work also showed that angular particles experienced more crushing than spherical particles. Differences in particle mineralogy will affect the onset of crushing due to differences in the distribution of particle strengths (Yamamuro et al. 1996).

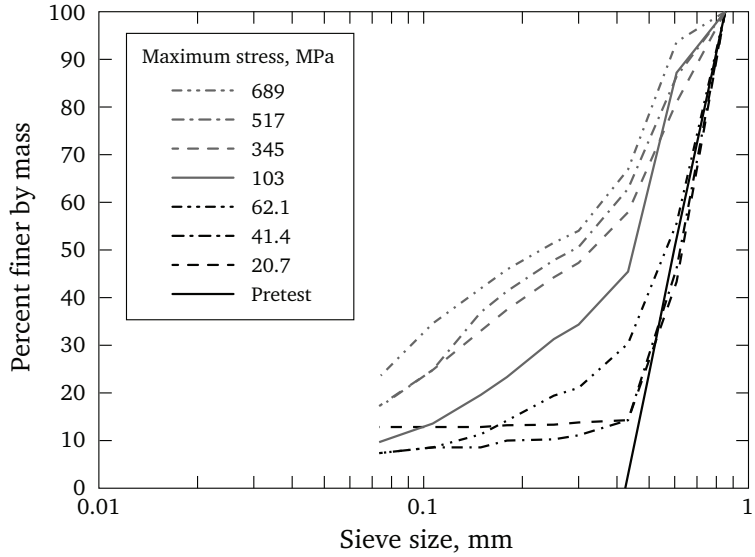


**(a)**

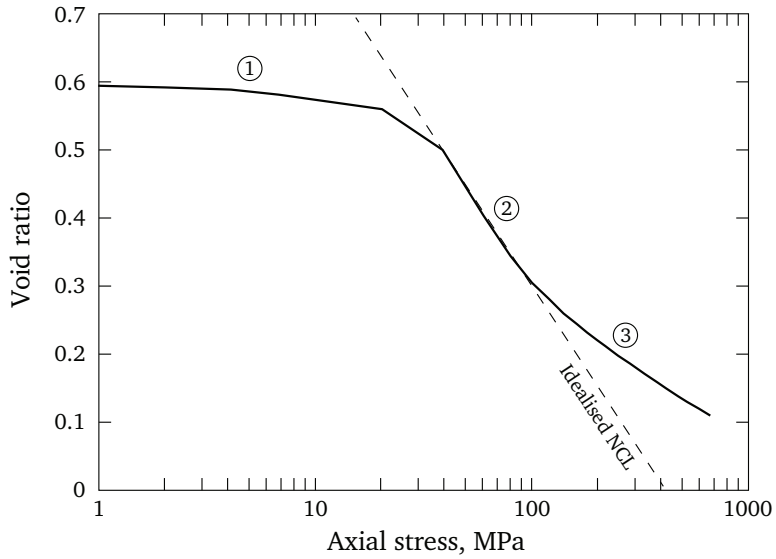


**(b)**

**Figure 2.8:** Evolution of a) particle size distribution and b) compressibility of Ottawa sand under one-dimensional compression, after Hagerty et al. (1993).

The effects of moisture content will form a vital part of a material model for blast and impact loading, and it is well known that an optimum moisture content exists for the compaction of a soil to its maximum dry density – that is, the maximum dry density achieved through particle rearrangement alone (BS 1377–4:1990). However, high-pressure quasi-static tests on sand with varying moisture content do not currently exist in the open literature, despite the growing interest in the effects of moisture content on sands at high strain rates.

### 2.4.2 Strain-rate effects

While high-strain-rate tests on sand have become commonplace over the last decade, much of the work has focused on investigating the effects of factors such as particle size distribution, moisture content and confinement at high strain rates (see §2.4.3). Relatively little complete information is available specifically concerning strain-rate effects, and in particular, whether soil behaviour changes between the quasi-static and high-strain-rate loading regimes. A summary of the literature discussed below is presented in Table 2.2, where key variables are highlighted. As the current work is particularly concerned with the quasi-static and high strain rate regimes, discussion of very high strain rate (e.g. flyer plate) experiments is omitted, except in cases where comparison is also made with these regimes.

Farr (1986) used uniaxial strain devices involving a hydraulically or explosively-driven ram to test four partially saturated soils at strain rates of $10^{-3}\,s^{-1}$ to $10^{3}\,s^{-1}$. The soils tested were a medium carbonate beach sand, a fine/medium quartz sand, a well-graded silty sand, and loess (silt). With peak stresses of 50 MPa to 70 MPa, all of the soils were stiffer when tested at higher strain rates, with increases in constrained modulus ($M = \sigma_a/\varepsilon_a$ when $\varepsilon_r = 0$) ranging from 45% for the quartz sand to 125% for the carbonate sand (Figure 2.9a). The majority of this increase occurred between strain rates of $10^{-3}\,s^{-1}$ and $10^{1}\,s^{-1}$, with a further increase in strain rate having a more limited effect. Particle breakage decreased slightly with increasing strain rate for all soils (Figure 2.9b). As the mineralogy, PSD, angularity, initial density and moisture content of each soil was different, the variation in strain-rate sensitivity between soils can not be attributed to any particular property.

Bragov et al. (2008) tested dry, fine quartz sand using SHPB and plate impact experiments to determine the dynamic response at strain rates of $10^{3}\,s^{-1}$ and $10^{6}\,s^{-1}$, and found no significant change in stiffness over this range. In the SHPB tests the sand was confined in a steel jacket, which was also fitted with a strain

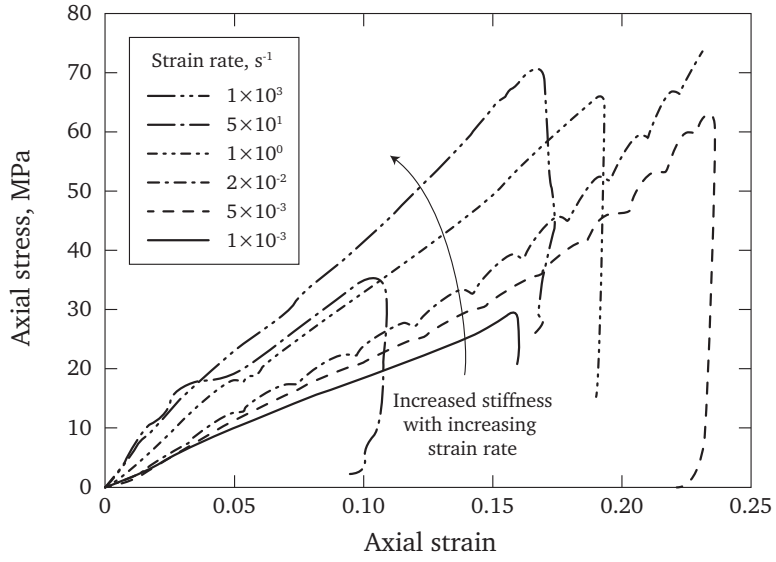


**(a)**

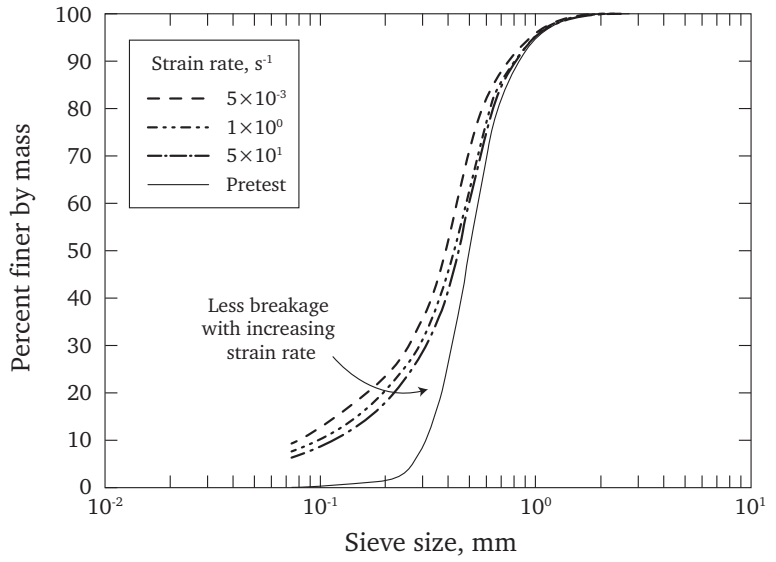


**(b)**

**Figure 2.9:** Effect of strain rate on a) stiffness and b) particle breakage in partially-saturated carbonate beach sand, after Farr (1986). Strain rates are approximate, based on the available data.

| | Specimen | | | | | | | Experiment | | | | |
|---|---|---|---|---|---|---|---|---|---|---|---|---|
| Reference | Material tested | Particle angularity | $D_{50}$ (μm) | $l_{s,nom}$ (mm) | $\rho_d$ (Mg m$^{-3}$) | $w$ (%) | $S_r$ (%) | Test apparatus | Lateral confinement | Peak stress (MPa) | Peak strain rate (s$^{-1}$) | Conclusions |
| Farr (1986) | Quartz sand<br>Carbonate sand<br>Clayey sand<br>Clay | SA*<br>SR/R*<br>–<br>– | 350<br>500<br>300<br>20 | 13<br>13, 23<br>13<br>13 | 1.62<br>1.62<br>1.84<br>1.63 | 5.5<br>5.0<br>3.5<br>11.5 | 23 *<br>19 *<br>21 *<br>47 * | Hydraulically/ explosively-loaded ram | Steel cylinder | 50–70 | $10^{-4}$–$10^{3}$ | Increase in stiffness from lowest to highest strain rate for all materials, from 45% for quartz sand to 125% for carbonate sand. |
| Ross et al. (1986) | Quartz sand<br>Quartz sand<br>Silica flour | –<br>–<br>– | 300<br>600 *<br>< 60 | 50,<br>100,<br>150 | 1.6 | 0–18 | 0–72 * | Quasi-static<br>SHPB | Steel cylinder*<br>Steel cylinder | 2–10<br>2–14 | $2 \times 10^{-4}$<br>– | Increased water content increases stress transmission and wavespeed to an optimum saturation (∼ 50%), then decreases. Smaller grain size increases stress transmission. |
| Felice et al. (1987) | Clayey sand | – | – | 6.35, 12.7 | 1.87 | 7–15 | 45–98 * | SHPB | Steel* cylinder | 240–520 | $4 \times 10^{3}$ | Stiffening of the stress-strain response and earlier lock-up behaviour with increasing saturation. |
| Charlie et al. (1990) | Quartz sand | – | 250 | 101.6 | 1.60 | 0–24 * | 0–95 | Quasi-static<br>SHPB | –<br>Steel cylinder | 10<br>1.5–4.5 | $2 \times 10^{-2}$<br>– | Wavespeed and transmission ratio increasing from 0% to 30/40% saturation, then decreasing from 40–95%. |
| Veyera (1994) | Quartz sand | A/SA<br>SA<br>SR/R | 260<br>190<br>700 | 6.35,12.7 | 1.75 *<br>1.60 *<br>1.72 * | 0–19 *<br>0–25 *<br>0–21 * | 0–100<br>0–100<br>0–100 | SHPB | Steel cylinder | 120–240 | $10^{3}$, $2 \times 10^{3}$ | Little effect of moisture content on pre-saturation response. |
| Bragov et al. (2008) | Quartz sand | – | 200 * | 10 | 1.50 * | 0 | 0 | SHPB<br>Plate impact | Steel/Al ring<br>Copper cell | 80, 150, 500<br>3500 | $10^{3}$ *<br>$10^{6}$ | No significant strain rate effect observed between SHPB and plate impact tests. |
| Martin et al. (2009)<br>Kabir et al. (2010) | Quartz sand | – | 220 | 9.30 | 1.50 | 0–20 | 0–67 * | Quasi-static<br>SHPB | Steel cylinder<br>Steel cylinder | 55<br>15 | $10^{-5}$–$10^{-4}$<br>$4 \times 10^{2}$ shaped | Wet specimens less stiff than the dry specimen, but with no significant change between different moisture contents. |
| Song et al. (2009)<br>Kabir et al. (2010) | Quartz sand | – | 250 * | 9.3 | 1.5 | 0 | 0 | Quasi-static<br>SHPB | Polycarbonate, (Steel), (Polyolefin) | 180 | $10^{-3}$–$10^{1}$<br>$10^{2}$–$10^{3}$ | High-strain-rate tests 20% stiffer than quasi-static, but with large error bars, so no strain-rate effect claimed. Increase in stiffness with increased confinement. |
| Luo et al. (2014) | Quartz sand | SA/SR | 350 | 9 | 1.75 | 0–16.5 | 0–80 | SHPB | Steel cylinder | 350 | $6 \times 10^{2}$ shaped | No significant effect of moisture content on pre-saturation stiffness, particle breakage decreased with increased moisture content. |
| Current work | Quartz sand | SA/SR | 130 | 50<br>5 | 1.50 | 0–5.0 | 0–17 | Quasi-static<br>SHPB | Steel platens<br>Steel ring | 800<br>400 | $10^{-3}$<br>$10^{3}$ | |

– Data not reported  * Estimated from data provided

**Table 2.2:** Summary of literature on strain-rate and moisture effects in sand.

gauge to measure radial stresses. The relationship between the axial and radial stresses measured in the SHPB tests were also used to infer lateral stresses in the plate impact experiments, despite acknowledging the approximately uniaxial stress state at these strain rates.

Song et al. (2009) investigated the effects of strain rate and confinement on the response of a dry, fine quartz sand. Quasi-static and SHPB tests were used to characterise the sand response at a variety of strain rates between $10^{-3}$ $s^{-1}$ and $10^{3}$ $s^{-1}$ using a polycarbonate tube to confine the sample. The mean results suggest that at the highest strain rate the sand was around 20% stiffer than during the slowest quasi-static tests, though the authors reported no strain-rate effect due to the large amount of scatter in the results. SHPB tests using a polycarbonate tube were also compared with specimens confined in steel and polyolefin shrink wrap tubes, with the steel-confined specimens displaying an increase in stiffness and the polyolefin-confined specimens having a drastically reduced stiffness. The reduced stiffness when using polycarbonate suggests that more radial movement was permitted than in tests with a steel tube: the assumption of uniaxial strain may have been violated depending on the magnitude of this movement.

While the results from these investigations are difficult to compare directly, this small pool of existing data suggests that a strain-rate dependence on stiffness is only present when the soil is partially saturated. This could potentially be due to localised loading of the pore water, as increasing strain rates would reduce the opportunity for local pore water movement. The reduction in particle breakage with increasing strain rate in Farr's work could be explained by such pore water loading, however variations in particle breakage have also been observed between quasi-static and plate impact tests on glass microspheres, apparently without an accompanying increase in stiffness (Neal et al. 2014).

### 2.4.3 High-strain-rate behaviour

The split Hopkinson pressure bar has been used by a number of authors to investigate the effects of moisture content on the high-strain-rate response of sand. Ross et al. (1986) and Charlie et al. (1990) focused on the effect on wave speed and stress transmission in long specimens of various quartz sands. In both cases the wave speed and stress transmission in the sand increased from 0% to 40/50% saturation, then decreased with the addition of further water.

A number of authors have also investigated the effect of moisture content on the stiffness of sand at high strain rates. Felice et al. (1987) performed SHPB

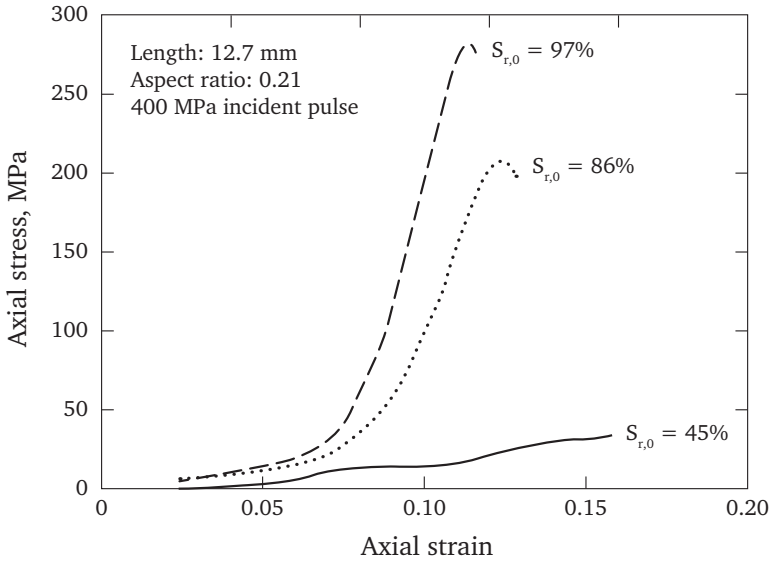


**(a)**

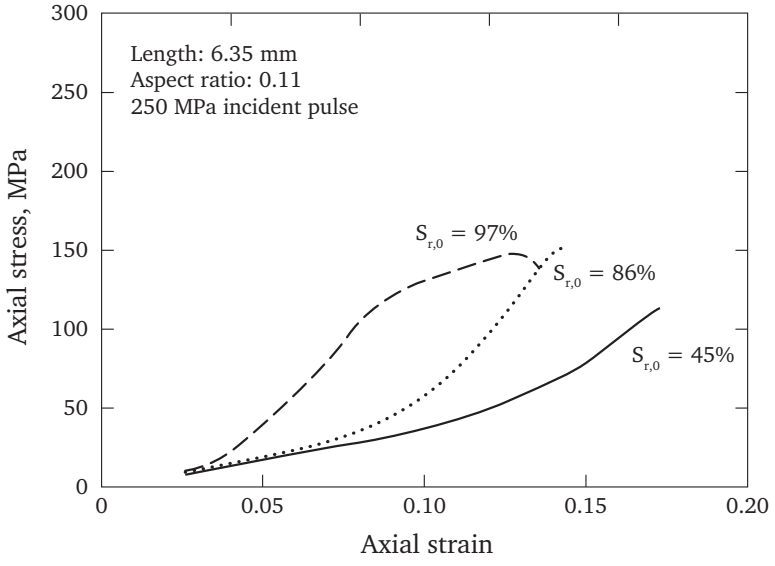


**(b)**

**Figure 2.10:** Effect of initial saturation on behaviour of clayey sand for a) 12.7 mm specimen, incident pulse 400 MPa, and b) 6.35 mm specimen, incident pulse 250 MPa, after Felice et al. (1987).

tests on a dense clayey sand at initial saturation ratios of approximately 45%, 86% and 97%. Specimens of length 12.7 mm and 6.35 mm (aspect ratios of 0.21 and 0.11) were confined in a long, thick cylinder and loaded with incident pulses of approximately 250 MPa and 400 MPa, respectively. The strain rate presumably varied between these test series, but complete information was not provided, with "strain rates up to $4000\,s^{-1}$" quoted. The 12.7 mm 86% and 97% specimens stiffened rapidly on reaching full saturation, and also appeared to be stiffer than the 45% specimen prior to saturation (Figure 2.10a). The 6.35 mm 86% and 97% specimens also stiffened rapidly at saturation, but the strain and stiffness at lock up varied from the longer specimens, and the pre-saturation responses of the specimens appear to be identical (Figure 2.10b). The differences in behaviour are difficult to discern due to the variation of both strain rate and specimen length, and could even be due to interaction with the confining cylinder, which overlapped the incident and transmitter bars by 19 mm.

Veyera (1994) tested three quartz sands with varying grading and angularity between 0% and 100% saturation in 20% increments. At a strain rate of $10^3\,s^{-1}$ the pre-saturation response of all three sands appeared to be relatively unaffected by changes in moisture content, though all soils stiffened rapidly on reaching full saturation. Tests were also carried out at a strain rate of $2 \times 10^3\,s^{-1}$, but while the higher strain rate results appear to be generally stiffer, the authors noted that the data was not sufficient to make a detailed comparison.

Martin et al. (2009) tested a fine silica sand by varying the saturation ratio at increments between 0% and 67%. All of the wet specimens behaved less stiffly than the dry specimen but, with large variations from test to test, there seemed to be no significant difference in the behaviour at these various moisture contents. The author related the reduction in stiffness to the added water lubricating the contact points between sand particles, aiding compaction. These tests were conducted at relatively low axial stresses (15 MPa), so no lock-up behaviour was observed and the response remained largely linear.

Luo et al. (2014) varied the moisture content of a dense fine/medium sand to achieve initial saturation ratios between 0% and 80%. The specimens above 20% initial saturation reached full saturation during loading to axial stresses of approximately 300 MPa and stiffened rapidly, but little pre-saturation difference in stiffness was observed between specimens (Figure 2.12a). Particle breakage decreased with the increasing moisture content, which suggests that

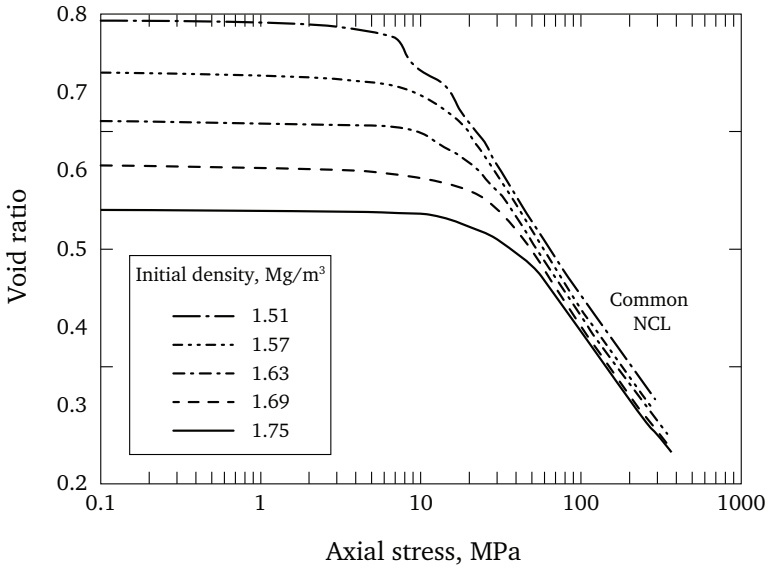


**Figure 2.11:** Effect of initial density on compressibility of dry quartz sand in SHPB experiments, after Luo et al. (2011).

the loading of pore water resulted in more favourable loading of the soil skeleton (Figure 2.12b).

A possible explanation for the difference in the pre-saturation responses in these investigations could be that added moisture aids the rearrangement of particles in loose specimens, reducing the stiffness (Martin et al. 2009), but has little effect in denser specimens, where there is less opportunity for rearrangement prior to the onset of particle crushing (Veyera 1994, Luo et al. 2014).

Luo et al. (2011) investigated the effect of the initial density at high strain rates, testing a dry fine/medium quartz sand at densities between $1.51\,\mathrm{Mg\,m^{-3}}$ and $1.75\,\mathrm{Mg\,m^{-3}}$. Pulse shaping was used, with peak strain rates between $610\,\mathrm{s^{-1}}$ and $675\,\mathrm{s^{-1}}$. While the authors reported a significant effect in $\sigma_x$–$\varepsilon_x$ space, the results replicate the quasi-static phenomena discussed above when plotted in $e$–$\log\sigma'_x$ space. The specimens converged on the NCL, with initially loose specimens joining the NCL at lower stresses, as shown in Figure 2.11.

The effects of particle size and particle size distribution in quasi-static testing have also been replicated in the high-strain-rate regime: well-graded soils tend to be less compressible than uniform soils and experience less particle breakage (Huang et al. 2013, Farr 1990), and finer soils are less compressible and experience less particle breakage than coarse soils (Luo et al. 2014).

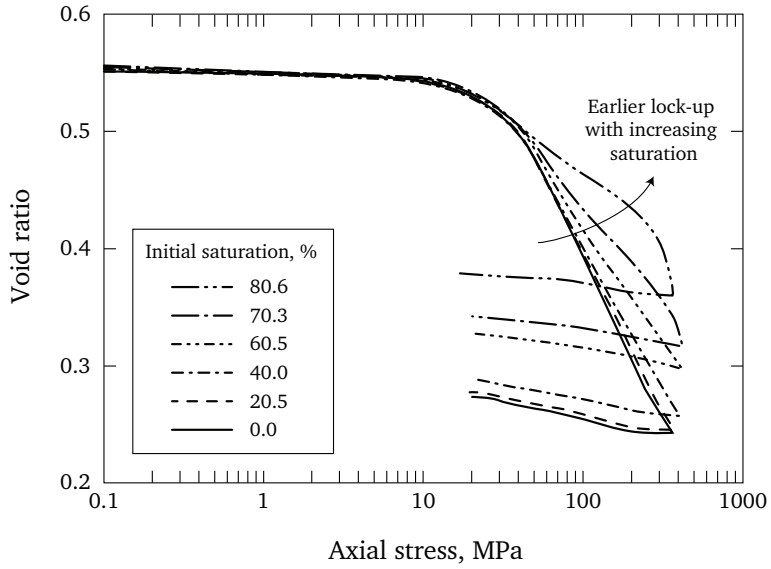


**(a)**

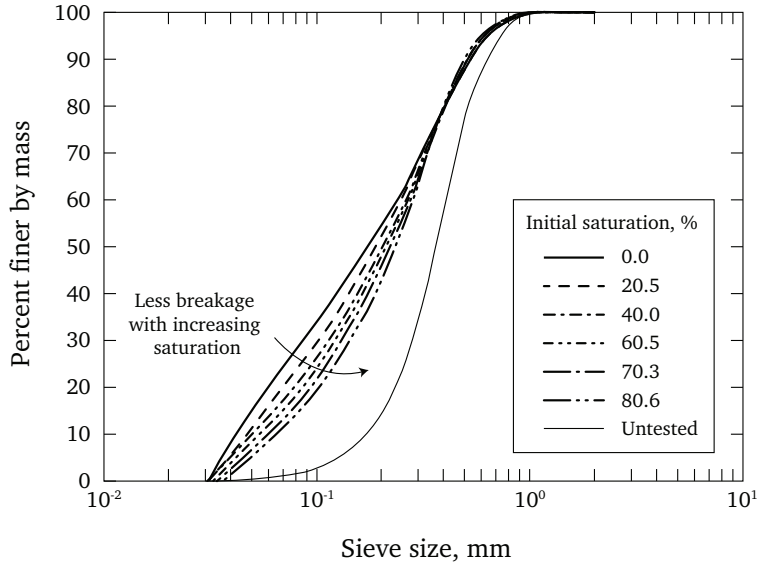


**(b)**

**Figure 2.12:** Effect of moisture content on a) compressibility and b) particle breakge of quartz sand at high strain rates, after Luo et al. (2014).

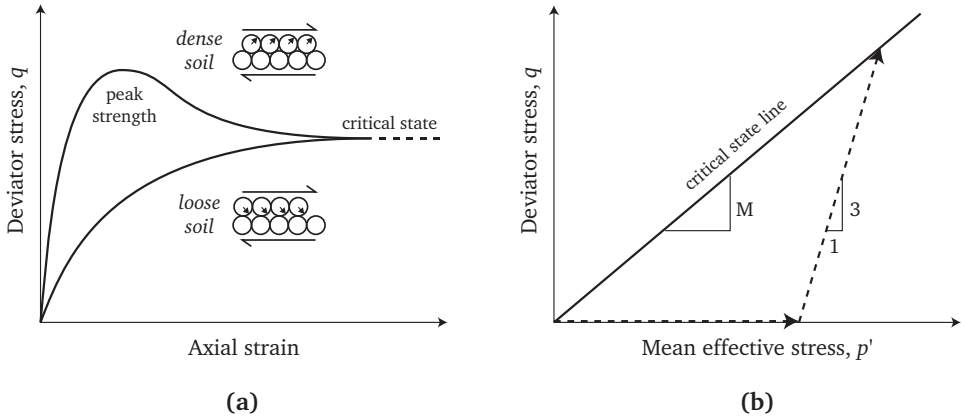


**Figure 2.13:** Shear behaviour of soils in conventional quasi-static experiments: a) shearing to a critical state, b) stress path in a drained conventional triaxial compression (CTC) test and the critical state line.

## 2.5 Shear behaviour of sand

While this work is primarily concerned with the compaction behaviour of sand under one-dimensional compression, a complete description of a soil for modelling purposes also requires an understanding of its shear behaviour at high strain rates, as loading from a blast or impact event will almost always contain a sizeable deviatoric component.

Shear strength in soil is the result of friction at the contacts between particles. In an initially loose soil, the application of shear strain causes the particles to move into a more dense arrangement, resulting in contraction of the soil. Similarly, an initially dense soil moves towards a looser particle arrangement under shear strain, resulting in expansion. The result of this dilatancy in soils is shown in Figure 2.13a, where the additional energy required for expansion causes dense soils to exhibit a higher shear resistance than loose under a given confining stress, up to a peak strength. At larger strains, both dense and loose soils reach a critical state, where the soil is shearing at a constant volume under a constant deviator stress. Characteristics such as dilatancy rates and peak strengths can be predicted using the state parameter, $\psi$, which considers how far, in terms of $e$, the soil is from a steady state in $e$–$p'$ space (Been and Jefferies 1985).

The shear behaviour of a soil at quasi-static strain rates is often assessed using the conventional triaxial compression (CTC) test. In a CTC test a cylindrical soil specimen in a rubber membrane is placed in a triaxial cell, which is filled with a pressurised fluid. This fluid applies a hydrostatic stress to the specimen, after

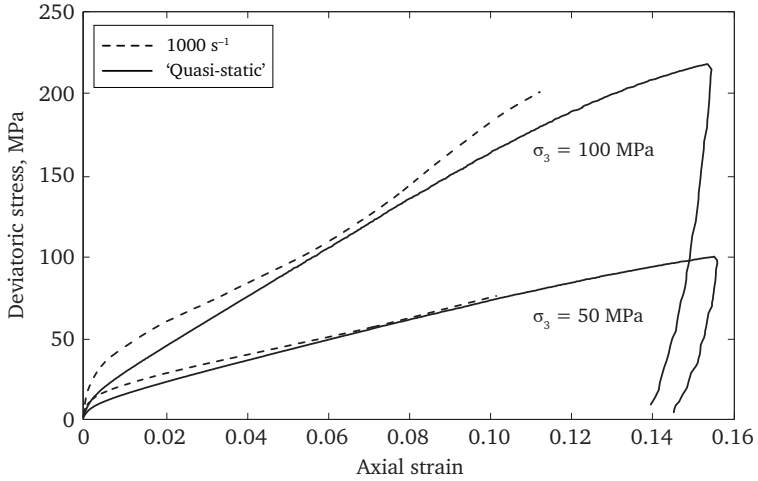


**Figure 2.14:** Strain rate effect on triaxial behaviour of dry quartz sand, after Martin et al. (2013).

which a deviatoric stress is applied axially by a piston until the critical state is reached, as shown by the stress path in Figure 2.13b. By performing the test at a variety of confining stresses, the critical state line (CSL) can be established, which defines the strength of the soil at any mean effective stress (Wood 1990).

Frew et al. (2010) developed a triaxial SHPB with pressure vessels fitted around the specimen and transmitter bar ends, which allowed hydrostatic loading to be followed by a high-strain-rate deviatoric phase. This apparatus was used by Martin et al. (2013) to characterise the shear response of sand at confining stresses between 25 MPa and 150 MPa and strain rates of 500 $s^{-1}$ and 1000 $s^{-1}$, where increasing stiffness was observed with increasing confining stress. The results were also compared with existing quasi-static data to assess the effect of strain rate, as shown in Figure 2.14. For confining stresses of 50 MPa and 100 MPa little change in shear strength was observed.

While this suggests that there is no strain rate dependence on shear strength, the use of a dynamic CTC test is not necessarily representative of the loading in a blast or impact event, where a soil may deform uniaxially before developing significant lateral confinement. This confinement is also influenced by the inertia of the surrounding soil, and quantification of this inertial effect in a soil specimen would require a departure from the CTC approach to allow confining stress to develop passively (Barr et al. 2016).

## 2.6 Numerical modelling at high strain rates

Full-scale trials of blast and ballistic events can be expensive and time-consuming, and so it is increasingly common to model these events use numerical techniques, where parametric studies can be carried out quickly, and the behaviour of any part of the model can be obtained easily. Transient, non-linear events such as explosions and impacts are often modelled using explicit dynamics software such as LS-DYNA or Autodyn, which incorporate the Finite Element Method (FEM). In FEM a complex problem is broken down into *parts*, typically representing each material in the model, whose mechanical properties are described using an appropriate constitutive model. Each part is subdivided into *elements* using a *mesh*, and explicit time integration used to calculate the solution over each element at small time intervals (Hallquist 2007).

The accuracy of the solution depends partly on modelling considerations such as the geometry and resolution of the mesh and how contacts betweens parts are treated, but ultimately a part will behave as defined by its constitutive model. For this reason it is important that material models are robust and well validated against experimental data (Church et al. 2014). In practice, this means basing the material model on simple experimental characterisation of the material, and then comparing the solution to a more complex problem with the data from a physical experiment. Disagreement between the experiment and the model will suggest that the model does not accurately represent the material, and it is not sufficient to arbitrarily alter the input until the results are deemed to match, as the model will be unable to predict the material response in other test configurations.

### 2.6.1 Simulation of dynamic events in soil

Modelling soils using FE methods usually involves treating the soil as a continuum with uniform bulk properties. In the last decade there has been a great increase in the use of Discrete Element Modelling (DEM), as originally proposed by Cundall and Strack (1979), which considers the movement and behaviour of individual particles in the soil, and explicitly models the contacts between the particles (O'Sullivan 2014). These properties give DEM the potential to be used to research fundamental soil behaviour, but a detailed understanding of the inter-particle friction and particle fracture is also required to obtain accurate results, and computational limitations currently restrict its use to modelling small numbers of particles.

Since particles are not modelled explicitly in a continuum model, it relies on a constitutive model to capture the important bulk properties, which can usually be attained using standard geotechnical tests. LS-DYNA and Autodyn have a number of built-in material models which can be used to model the behaviour of soil, varying from the simple definition of a compressibility curve and yield surface to more complex models incorporating pore water effects, strain softening and hardening and strain-rate effects. Most FE studies in the open literature which involve soil at high strain rates are related to buried explosive events, but FE models have also been used to assess aircraft and spacecraft crashworthiness and to evaluate DEM models of soil systems.

Heymsfield et al. (2010) used LS-DYNA's *Soil and Foam* model (`*MAT_005`) to model contingency landings of the Orion capsule onto sand and clayey sand. This simple model incorporates a compressibility curve, yield surface and elastic constants, and was populated with data from relatively low-stress (<490 kPa) quasi-static soil tests. Soils were characterised at the experimental moisture content of 12%. Full-scale drop tests were compared with the model using recordings of fuselage acceleration and crater depths, and good agreement was achieved, particularly in the case of the sand.

Wang (2001) simulated the detonation of a 100 g C4 charge buried in dry sand using *Soil and Foam with Failure* (`*MAT_014`), which is identical to *Soil and Foam* (`*MAT_005`) except for the definition of a failure pressure where the material's tensile strength is removed. The compressibility of the soil was defined to 4.1 GPa with reference to unpublished material tests, though, as this model uses a quadratic-defined yield surface, it is not clear whether the deviatoric response was also characterised to the high pressures experienced during the explosive event. The results of the numerical model were compared with experimental data for burial depths of 0 mm and 30 mm, where overpressure measurements had been collected 300 mm and 700 mm above the soil. The pressure profile predicted by LS-DYNA consistently underestimated the peak overpressure, but greatly overestimated the positive phase duration, leading to larger impulses than in the physical experiments.

Fiserova (2006) modelled the loading on a mine-impulse pendulum from explosives buried in a cohesive silty sand in Autodyn. Separate EOSs for solid particles, air and water were applied according to the proportion of each phase, although both the solid phase EOS and the yield surface were extrapolated from two triaxial tests with confining pressures less than 2 MPa. The simulated impulse from surface-laid charges was insensitive to moisture content and so under-predicted the experimental impulse (Figure 2.15a). The impulse from

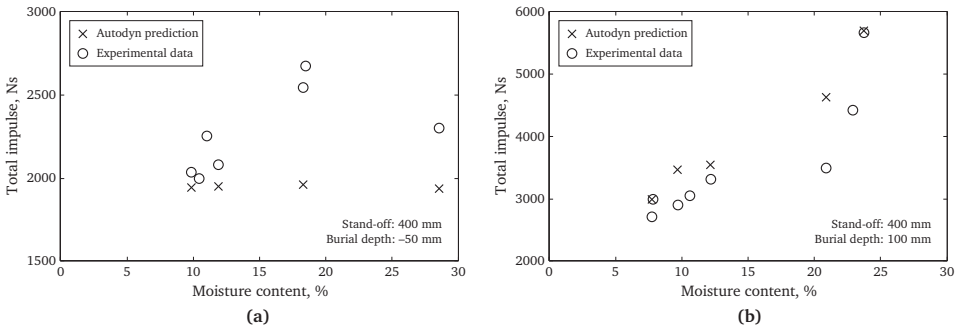


**Figure 2.15:** Experimental results and numerical predictions for impulse from charges buried in silty sand at depths of a) −50 mm and b) 100 mm, after Fiserova (2006).

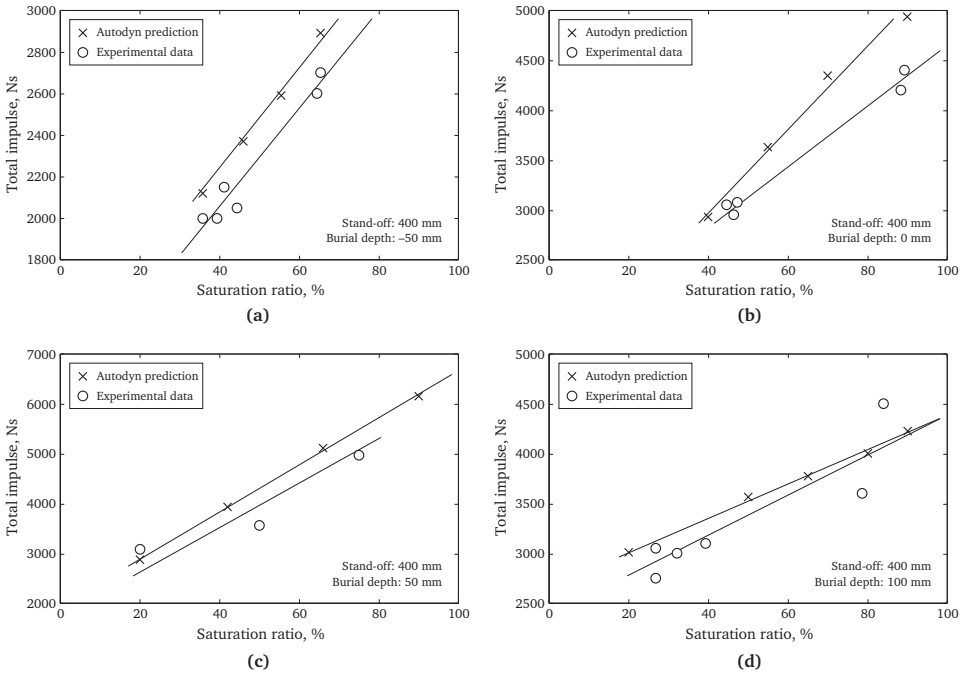


**Figure 2.16:** Experimental results and numerical predictions for impulse from charges buried in sand at depths of a) −50 mm, b) 0 mm, c) 50 mm and d) 100 mm, after Grujicic et al. (2008). Possible trend lines have been added to aid interpretation.

buried charges more closely followed the experimental trend, although large variations exist in the experimental data at higher moisture contents.

Grujicic et al. (2008) adapted a sand model developed by Laine and Sandvik (2001) to account for variations in moisture content by linearly interpolating between data for a dry sand and saturated sand. An equation of state was defined using flyer plate data, and a Mohr–Coulomb yield surface with a Tresca limit was implemented, although it is not clear how this was calibrated. The loading from a buried explosive on a mine-impulse pendulum was modelled in Autodyn for unsaturated sand, where predictions of total impulse were in moderate agreement with the experimental results, as shown in Figure 2.16. Larger errors in the predictions of flush-buried and surface-laid detonations were explained as being due to the modelling of the explosive rather than the sand, suggesting that loading errors may also be present in the shallow-buried cases, where better prediction was claimed.

An et al. (2011) developed a three-phase viscoplastic material model for use in LS-DYNA, which included separate equations of state for the soil skeleton, pore water and pore air: the volume change in each phase was calculated at a particular pressure, then the proportion of solid particles, water and air were used to update the bulk modulus and density of the soil. This material model was used to simulate the detonation of a 100 g C4 charge buried in sand, which was characterised quasi-statically to provide the model parameters. Only dry and saturated cases were considered (two-phase soils), where the model provided good predictions of ejecta height and shock-front arrival time and pressure when compared with experimental results, particularly in the case of saturated sand.

Jayasinghe et al. (2013) simulated the response of an aluminium pile to the detonation of a charge buried in saturated sand using *FHWA Soil* (`*MAT_147`), and compared the deformation of the pile to the results of centrifuge tests by another author. The *FHWA Soil* model includes parameters for soil saturation, strain hardening, strain softening and viscoplasticity, but while these were all implemented many of chosen parameter values were quoted without justification, and the soil was not characterised beyond the generic classification of 'saturated sand'. In particular, a strain rate effect on soil strength was incorporated without reference to its validity or the derivation of the required parameters. Comparisons were made between the centrifuge and LS-DYNA model in terms of the peak pressures in the soil and the deflection of the pile, where the modelled event underestimated the peak pressures in the soil at the stand-offs of interest: this is reportedly due to not modelling the charge with a casing as in

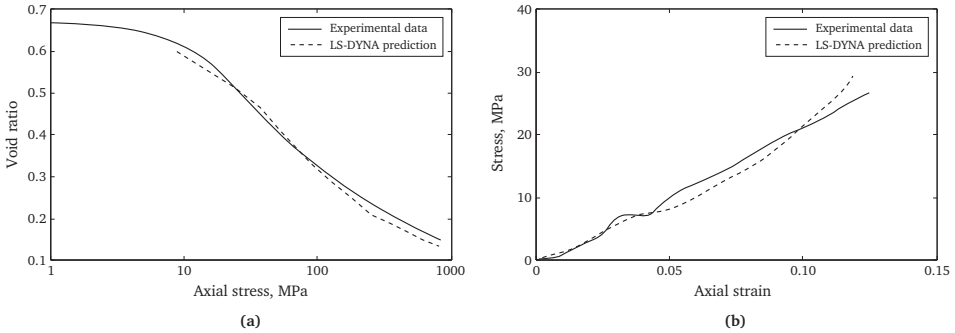


**Figure 2.17:** a) Simulation of quasi-static one-dimensional compression of sand, and b) Simulation of a confined SHPB experiment on sand, after Fang et al. (2014).

the centrifuge tests. Despite the variation in peak pressure, the peak deflection of the piles was in good agreement with the centrifuge results, but with variation in the deflected shape.

Fang et al. (2014) developed a method for generating three-dimensional sand specimens for DEM with distributions of particle shape and size, and demonstrated its use with quasi-static and dynamic tests in LS-DYNA. The individual particles were modelled using the *Johnson-Holmquist Concrete* model (`*MAT_111`), a pressure-dependent model which includes parameters for permanent crushing and strain-rate dependence, though the authors do not reference material tests or precedent for the model parameters chosen to populate the model.

A DEM sand specimen was used to replicate the quasi-static one-dimensional compression tests reported by Yamamuro et al. (1996). A good correlation with the experimental results was claimed (Figure 2.17a), though it is not clear which of the three sands tested by Yamamuro et al. was being considered, or which material properties influenced the generation of the sand specimen. The coefficient of friction between the sand particles was chosen as 0.3 with reference to 'the research', but without discussion of why this value was relevant for the selected soil.

LS-DYNA was also used to model SHPB tests on dry sand by Kabir et al. (2010), also reported in Song et al. (2009) as above. This model replicated the experimental stress-strain behaviour at low stresses, but then began to stiffen excessively above 20 MPa (Figure 2.17b). Again no reference was made to the generation of the sand specimen, and while the modelled SHPB did not appear to include a striker bar, no explanation of the of the initiation of the incident pulse was provided.

Most of these studies are not directly comparable, but it can be seen that models with a rigorously-defined soil material model are more likely to accurately predict the soil response, while models with less evidence of characterisation can be made to match a final deflection or a peak pressure, for example, but can not accurately predict the response over the whole time or volume of interest. A common issue with many of the above studies is a lack of soil shear strength data at the high pressures being modelled: this is addressed as part of the modelling work presented in Chapter 6.

## 2.7 Summary

This chapter introduced the value of the split Hopkinson pressure bar in investigating the behaviour of materials at high strain rates, and highlighted important experimental considerations when testing soils, where the specimen length-to-diameter ratio should be chosen carefully to reduce the effects of lateral inertia in the specimen, and friction effects at the specimen boundaries. The assumptions made in one-dimensional wave theory were shown to be violated for high-frequency stress pulses, as dispersive effects become important. Methods were introduced which allow the correction of frequency-dependent effects, offering an improved way of timeshifting signals with high-frequency components.

The quasi-static behaviour of soils under one-dimensional compression was discussed in terms of particle deformation, rearrangement and crushing, and the dominance of these regimes used to describe soil response in $e$–$\log \sigma'_a$ space. Particle crushing increases with stress, but decreases with coordination number, and large or angular particles are more susceptible to fracture than small or well-rounded particles. There are currently no studies on the effect of moisture content on quasi-static compressibility to high stresses.

The limited existing data on strain-rate effects in soils suggests that stiffness increases with strain rate only in partially-saturated soils, possibly due to pore water loading. A series of tests on the same soil is required to discern the influence of moisture content on such a strain rate effect, which may also help explain the mechanism behind variations in particle breakage.

Moisture appears to aid the rearrangement of particles in loose sands at high strain rates, but has little effect on dense sands until pore water begins to sustain significant loading and lock-up behaviour is observed. The effects of initial density and particle size and distribution appear to replicate the trends seen in quasi-static tests.

Numerical modelling using FEM was introduced as a valuable tool for predicting dynamic events in soil, where parameters such as deflections and stress states can be obtained over the entire field of interest, provided that the material models which define the behaviour of the model parts are sufficiently robust. A lack of high-pressure shear strength data was identified as a source of error in many of the existing studies.

The aim of the current work will be to investigate the effect of moisture content on the behaviour of quartz sand between quasi-static and high strain rates, which will require high-pressure quasi-static characterisation at varying moisture contents alongside SHPB testing. The mechanism behind any strain-rate dependence will be analysed with the aid of particle size analysis and modelling in LS-DYNA.

Chapter 3

# Strain-rate dependence in three sandy soils

## 3.1 Introduction

This chapter presents experiments on the effect of strain rate and moisture content on the behaviour of three sandy soils. The methodology of quasi-static (mac$^{2T}$) and dynamic (SHPB) one-dimensional compression tests is described. The results are analysed in terms of the compressibility of the dry soils under quasi-static loading, the effect of strain rate on the behaviour the dry soils, and the effect of moisture content on the strain-rate sensitivity of the medium sand. Suitable experimental modifications are identified to improve the understanding of the soil behaviour observed in this test series.

## 3.2 Material characterisation

The three soils can be defined using EN ISO 14688–1:2002 soil descriptions as:

- Light brown silty fine and medium SAND (‘sandy loam’);
- Pinkish light brown fine and medium SAND (‘medium sand’);
- Light brownish yellow coarse SAND (‘coarse sand’).

For brevity the soils will be referred to using the short names noted in parentheses. Medium sand is the main focus of this work, with additional experiments on sandy loam and coarse sand used to assess the sensitivity of any observed strain-rate effects to changes in soil properties. Table 3.1 provides an overview of these soil properties, which were derived using the methods described in the following sections.

| | Sandy loam | Medium sand | Coarse sand |
|---|---|---|---|
| Primary mineral | Quartz | Quartz | Quartz |
| $\rho_s$, $\mathrm{Mg\,m^{-3}}$ | 2.65 | 2.65 | 2.65 |
| | | | |
| $D_{10}$, µm | 40 | 130 | 520 |
| $D_{50}$, µm | 200 | 250 | 740 |
| $D_{60}$, µm | 240 | 280 | 790 |
| $C_u$ | 6.0 | 2.2 | 1.5 |
| | | | |
| Particle sphericity | Medium–High | Medium–High | Low–High |
| Angularity | SR–SA | SR–SA | WR–SR |
| Surface texture | Rough | Rough | Smooth |

**Table 3.1:** Overview of soil properties.

### 3.2.1 Particle density

The particle density, $\rho_s$, is the density of the solid mineral particles, and is used with the bulk dry density, $\rho_d$, to calculate the void ratio of a soil with the relation

$$e = \frac{\rho_s}{\rho_d} - 1 \tag{3.1}$$

The particle density of each soil was established by comparing the masses of a volume of water and the same volume of a soil–water suspension, as described in BS 1377–2:1990 §8.2. The particle density of all three soils was calculated to be $2.65\,\mathrm{Mg\,m^{-3}}$, which is the density of quartz.

### 3.2.2 Particle shape

The shape of the sand-sized particles in the soils were assessed qualitatively with an optical microscope (Figure 3.1) using the descriptors provided in EN ISO 14688–1:2002, where

- Sphericity describes how well the shape of a particle approximates a sphere, where low-sphericity particles tend to be elongated along one axis;
  [*low* < *medium* < *high*]
- Angularity describes the shape of particle edges and corners, regardless of whether or not the overall shape is regular;
  [*well rounded* < *rounded* < *subrounded* < *subangular* < *angular*]


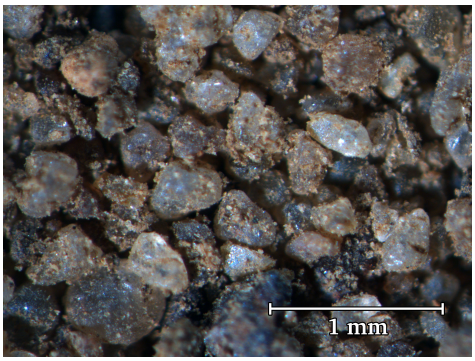


**(a)** Sandy loam (most silt removed)

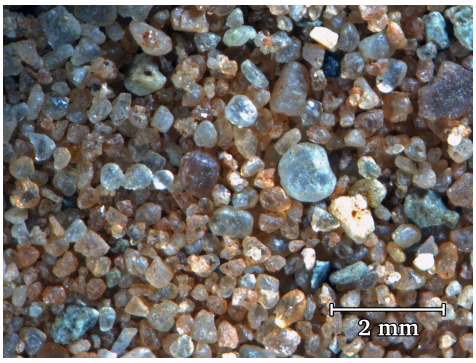


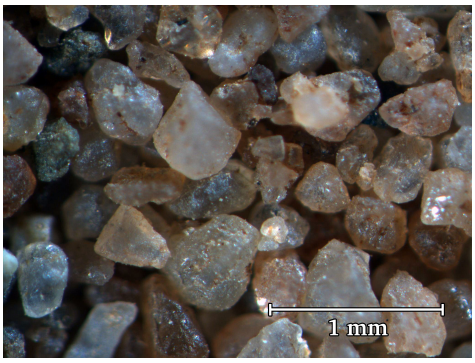


**(b)** Medium sand

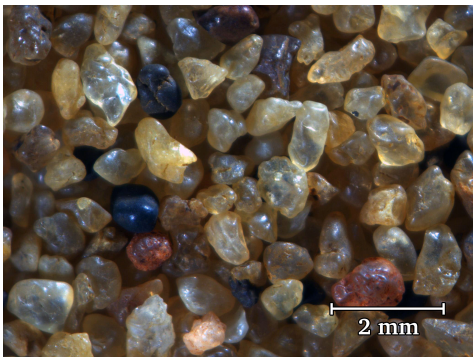


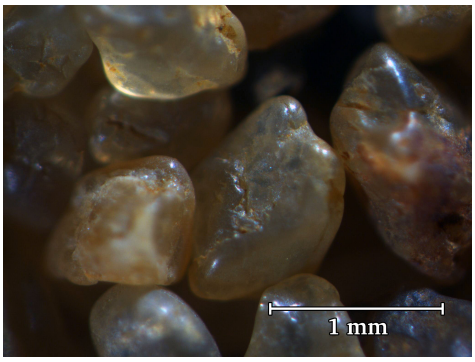


**(c)** Coarse sand

**Figure 3.1:** Optical microscope images of a) sandy loam, b) medium sand and c) coarse sand.

- Surface texture describes the texture of the particle faces. [*rough/smooth*]

In the sandy loam most of the sand particles are of medium to high sphericity, are subrounded to subangular, and have a rough surface texture. Similarly, in the medium sand the majority of particles have a medium to high sphericity, are subrounded to subangular, and have a rough surface texture. The particles in the coarse sand vary from low to high sphericity, and are well-rounded to subrounded. They have a relatively smooth surface texture, but with pitting on some particles.

### 3.2.3 Particle size distribution

The particle size distributions (PSDs) of the three soils were assessed using a Malvern Mastersizer 3000 particle size analyser fitted with a dry dispersion unit. Particle size histograms of each soil are shown in Figure 3.2, and are represented in the cumulative form more familiar to geotechnical works in Figure 3.3. The Mastersizer measures the scattering of light caused by a dispersed specimen, and calculates the size of individual particles by analysing this data using the Mie theory of light scattering. Application of Mie theory requires a knowledge of the refractive index of the material being tested, which was assumed to be that of quartz (1.544) for all three soils.

The Mastersizer 3000 is capable of measuring particle sizes from 10 nm to 3.5 mm at 100 logarithmically-spaced intervals, and records a single size value for each particle, which is the diameter of a sphere of equivalent volume. The concept of equivalent volume differs from the approach used in standard geotechnical sieving, where the ability of a low-sphericity particle to pass a sieve is dependent on its intermediate dimension, and particles are counted by mass instead of volume. The size of a low-sphericity particle measured using sieve analysis will differ from the size measured using laser diffraction (Figure 3.4), and so the PSD of a soil containing low-sphericity and medium-sphericity particles will vary between methods. This is shown for the medium sand in Figure 3.3, where the PSD obtained through laser diffraction is coarser than the PSD from sieve analysis. The results will also vary due to the difference in counting by mass or volume but, as the majority of the particles in each soil have the same particle density, the effect is unlikely to be significant. The Mastersizer 3000 includes a result emulation tool, which can emulate sieve data through the application of user-defined factors, but these factors are defined manually for each specimen type and, since they are related to a specific distribution of particle

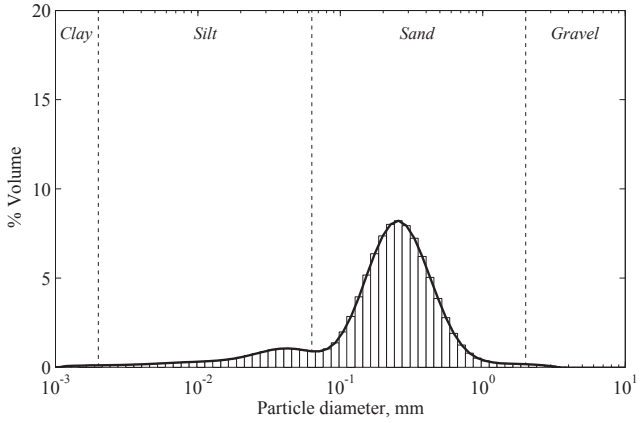


**(a)** Sandy loam

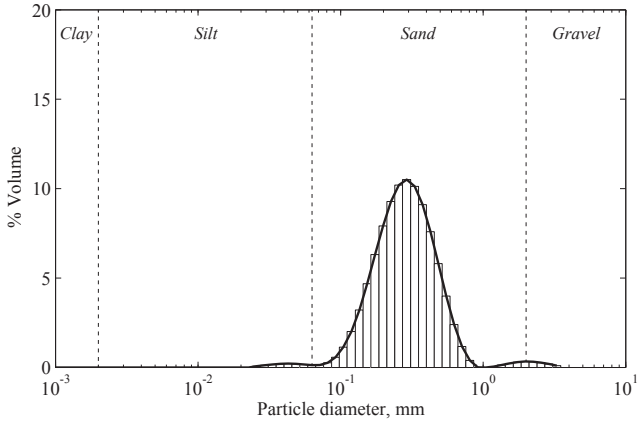


**(b)** Medium sand

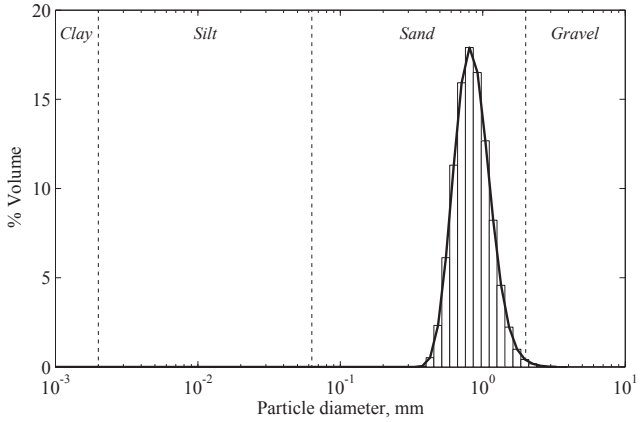


**(c)** Coarse sand

**Figure 3.2:** Particle size distribution histograms of a) sandy loam, b) medium sand and c) coarse sand.

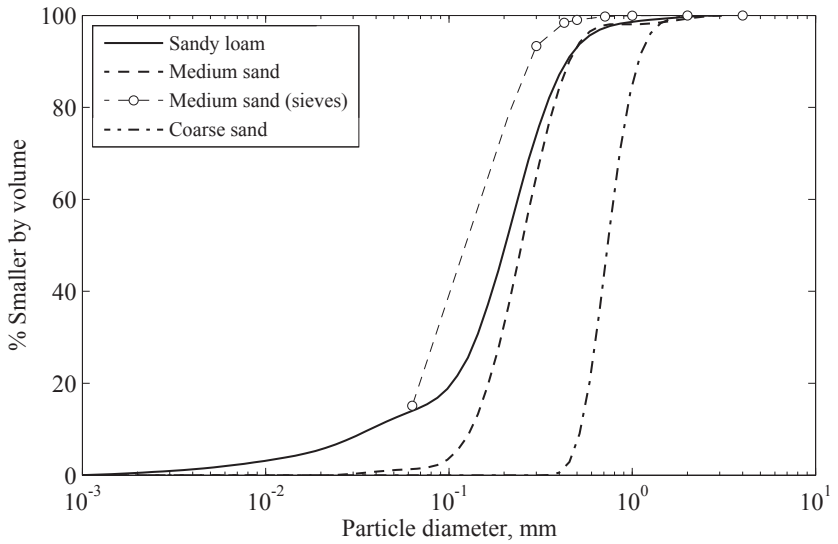


**Figure 3.3:** Cumulative particle size distributions of sandy loam, medium sand and coarse sand using laser diffraction, and a comparison with sieve analysis of the medium sand.

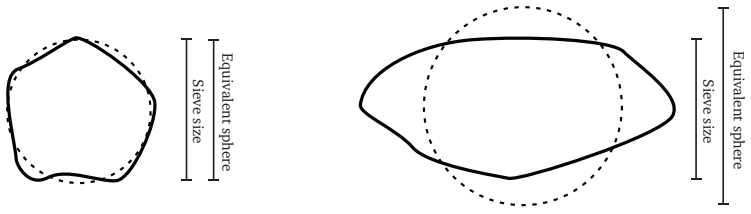


**(a)** High-sphericity particle **(b)** Low-sphericity particle

**Figure 3.4:** Equivalent-volume spheres for particles of varying sphericity, but with the same sieve size.

shapes, can not be directly applied to specimens where particle breakage has occurred. To ensure that all results can be compared reliably, only the laser light diffraction method will be used in this work, as the high resolution and low particle size limit will be valuable in analysing the level of particle breakage in soil specimens loaded to high pressures.

The histograms in Figure 3.2 show the distribution of particle sizes in the three soils by percentage volume, and include the boundaries of the particle size fractions. All three soils are defined as sands, with only the sandy loam containing a significant silt fraction. The sand fraction of the sandy loam and medium sand have similar distributions of fine- and medium-sand-sized particles, while the coarse sand contains a narrower distribution of mostly coarse-sand-sized particles.

The 'narrowness' of the PSDs can be described using the coefficient of uniformity, $C_u$, which is defined as

$$C_u = \frac{D_{60}}{D_{10}} \tag{3.2}$$

where $D_{10}$ and $D_{60}$ are the $10^{\text{th}}$ and $60^{\text{th}}$ percentile particle sizes, respectively. The values of $D_{10}$, $D_{50}$, $D_{60}$ and $C_u$ for each soil are presented in Table 3.1. A soil with a $C_u \geq 4$ has a wide distribution of particle sizes and is classified as well-graded, while a soil with a $C_u < 4$ has a narrow distribution of particle sizes and is classified as poorly-graded. Of the three soils considered, the medium sand and coarse sand are poorly-graded with coefficients of uniformity of 2.2 and 1.5 respectively, while the sandy loam is well-graded with a coefficient of uniformity of 6.0, due to its silt content.

### 3.2.4 Particle mineralogy

X-ray diffraction (XRD) was carried out on all three soils to establish their constituent minerals. In XRD an incident x-ray beam is diffracted by the regular atomic structure of a crystalline specimen: measurement of the intensity of the diffraction at various angles of incidence, $\theta$, leads to a unique diffraction pattern, which can be compared to a database of known patterns to identify the phases present in the specimen. Phase analysis was carried out using a Siemens D5000 diffractometer with a $\text{Cu}_{\alpha 1}$ radiation source, and the ICDD's Powder Diffraction File (PDF-4+).

Figure 3.5 shows the diffraction pattern obtained for each soil, where the peaks have been labelled with the associated mineral. As expected, quartz is abundant in all three sands, as shown by the intensity of the associated peaks. Sandy

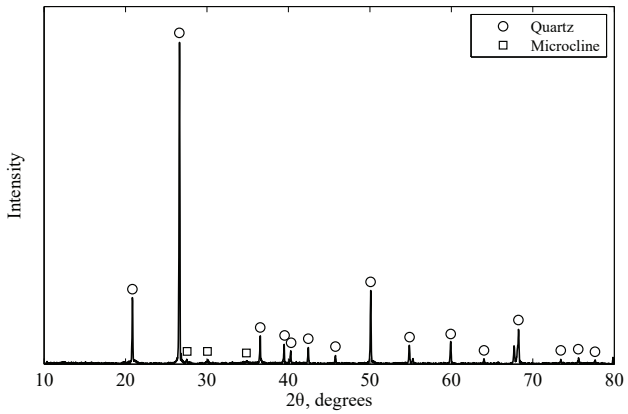


**(a)** Sandy loam

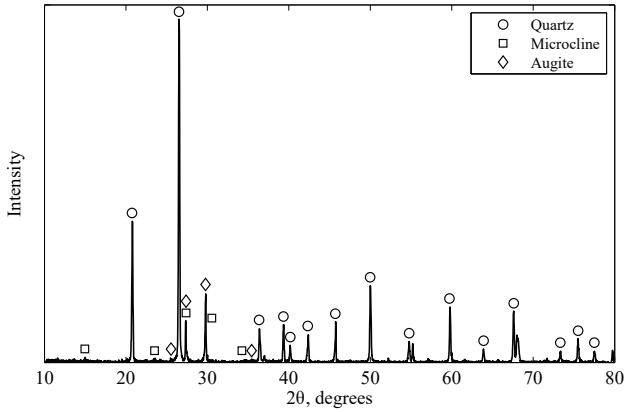


**(b)** Medium sand

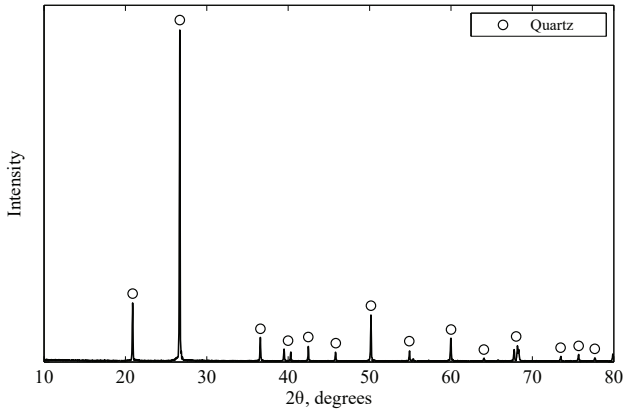


**(c)** Coarse sand

**Figure 3.5:** X-ray diffraction data for a) sandy loam, b) medium sand and c) coarse sand.

loam and medium sand also contain minor quantities of microcline, a potassium feldspar ($K\,Al\,Si_3O_8$), and medium sand contains minor quantities of augite, a pyroxene group mineral ($Ca\,Mg\,Si_2O_6$). Both microcline and augite are common igneous-rock-forming minerals, and rock fragments are indeed visible in the microscope images of the soils in Figures 3.1a and 3.1b.

The relatively large size of the sand particles and the abundance of quartz means that trace minerals cannot be identified from an unsorted specimen, as the associated peaks are lost in the signal noise. For example, only peaks associated with quartz were identified in the coarse sand, while the microscope images also show a number of dark blue-grey particles. As these trace minerals are only present in small quantities they are not expected to have much influence over the mechanical properties of the sands.

### 3.2.5 Moisture content

Soil specimens were tested at moisture contents of 0%, 2.5% and 5.0%, where the moisture content, $w$, is the ratio of the mass of water to the mass of dry sand. All of the soils were oven dried at 110 °C for at least four hours, then sieved to break up any agglomerations and mixed to ensure a homogeneous particle size distribution. Partially-saturated specimens were prepared by blending the soil and water between palette knives in a small metal tray.

The quasi-static specimens each contained 200.00 g of dry sand, to which 5.00 g or 10.00 g of water was added for a moisture content of 2.5% or 5.0% respectively, equivalent to 8.6% and 17.3% saturation at a dry density of $1.5\,Mg\,m^{-3}$. These specimens were used immediately after preparation to avoid loss of moisture. The water lost in transferring the wet sand from the mixing tray to the test box was found to be 0.04 g to 0.08 g, which was deemed acceptable.

The high-strain-rate specimens each contained only 3.50 g of dry sand, and so to ensure accuracy and avoid significant moisture loss 50 g samples were produced to the required moisture content, from which the smaller mass was then extracted. These specimens were prepared and tested in different laboratories, and so were stored in sealed plastic bags until required.

| | Strain rate, $s^{-1}$ | Peak axial stress, MPa | Moisture content, % | Number of tests |
|---|---|---|---|---|
| Medium sand | $10^{-3}$ | 800 | 0.0 | 3 |
| Medium sand | $10^{-3}$ | 800 | 2.5 | 3 |
| Medium sand | $10^{-3}$ | 800 | 5.0 | 3 |
| Medium sand | $10^{3}$ | 400 | 0.0 | 6 |
| Medium sand | $10^{3}$ | 400 | 2.5 | 5 |
| Medium sand | $10^{3}$ | 400 | 5.0 | 5 |
| Coarse sand* | $10^{-3}$ | 800 | 0.0 | 4 |
| Coarse sand | $10^{3}$ | 350 | 0.0 | 2 |
| Sandy loam* | $10^{-3}$ | 800 | 0.0 | 3 |
| Sandy loam | $10^{3}$ | 350 | 0.0 | 3 |

**Table 3.2:** Initial test programme, varying soil, strain rate and moisture content. Tests marked with an asterisk use data recorded by Tyas and Rigby (2012).

## 3.3 Test programme

The goal of this initial study was to assess the sensitivity of the three sandy soils to a large change in strain rate, and to observe how any variation in response is affected by changes in moisture content. All three soils were tested dry under one-dimensional compression at both quasi-static ($10^{-3}\,s^{-1}$) and high strain rates ($10^{3}\,s^{-1}$), at an initial dry density of $1.5\,Mg\,m^{-3}$. The medium sand was also tested at 2.5% and 5.0% moisture content. A summary of the test variables is shown in Table 3.2.

The quasi-static tests on sandy loam and coarse sand were carried out previously by Tyas and Rigby (2012): these experiments used approximately the same method as that described below.

## 3.4 Quasi-static methodology

Quasi-static one-dimensional compression tests were carried out to axial stresses of 800 MPa using mac$^{2T}$ (pronunciation: *MASS-et*), a test apparatus for Multi-Axial Compression of Concrete at Elevated Temperatures (Petkovski et al. 2006). As mac$^{2T}$ was originally designed for testing concrete, a soil testing box was developed to enable experiments on cohesionless materials. The stresses achieved

with mac$^{2T}$ are orders of magnitude larger than in conventional oedometer tests, which ensured that the quasi-static response of the soils was well defined over the range experienced in the SHPB experiments. As well as one-dimensional compression tests, mac$^{2T}$ allows soils to be tested multi-axially to high pressures, enabling characterisation of yield surfaces and tests involving more complex stress paths (as demonstrated in Chapter 6).

### 3.4.1 mac$^{2T}$

The mac$^{2T}$ test apparatus, shown in Figure 3.6, allows specimens to be tested in true multi-axial compression ($\sigma_x \neq \sigma_y \neq \sigma_z$), with independent control of loads or displacements in the x, y and z directions. In each axis the load is applied by a 4 MN hydraulic actuator installed in an independent loading frame. The centroid of the specimen is fixed to avoid eccentric loading by mounting the x- and y-axis frames on roller bearings, and by adjusting the vertical position of the z-axis frame with a fourth actuator. A reinforced concrete frame supports and guides the movement of the three steel loading frames, and is itself supported by three foundation columns which continue to basement level. This arrangement isolates the rig from the rest of the laboratory floor, reducing the effects of vibrations from other equipment.

In each loading frame two 200 mm diameter steel tension bars connect two 550 mm thick steel crossheads, as shown in Figure 3.7. One crosshead contains the fluid chamber for the actuator, while the other acts as a reaction block and supports the load cell, which is rated at 4 MN and operates to an accuracy of ±4 kN. Loads are transmitted from the actuator to the specimen, and from the specimen to the load cell, by 200 mm diameter steel rams, which each terminate in a 95 × 95 mm steel loading platen. The y- and z-axis actuators have a stroke of 60 mm, while the x-axis actuator has a larger stroke of 180 mm to allow specimens to be loaded into the rig.

While not considered in this work, the temperature of the specimen can be adjusted during testing in the mac$^{2T}$ rig. Temperatures of 300 °C can be achieved using the ceramic band heaters which are wrapped around the heating platens, while water-cooled cooling platens prevent transmission of the heat to the actuators and load cells.

The displacement of each specimen face is measured to an accuracy of ±1 μm by a laser interferometer unit, which operates along an evacuated stainless steel tube inside the loading ram. Light from a laser head outside the loading frame is directed into the tube by a linear interferometer, and travels along the vacuum

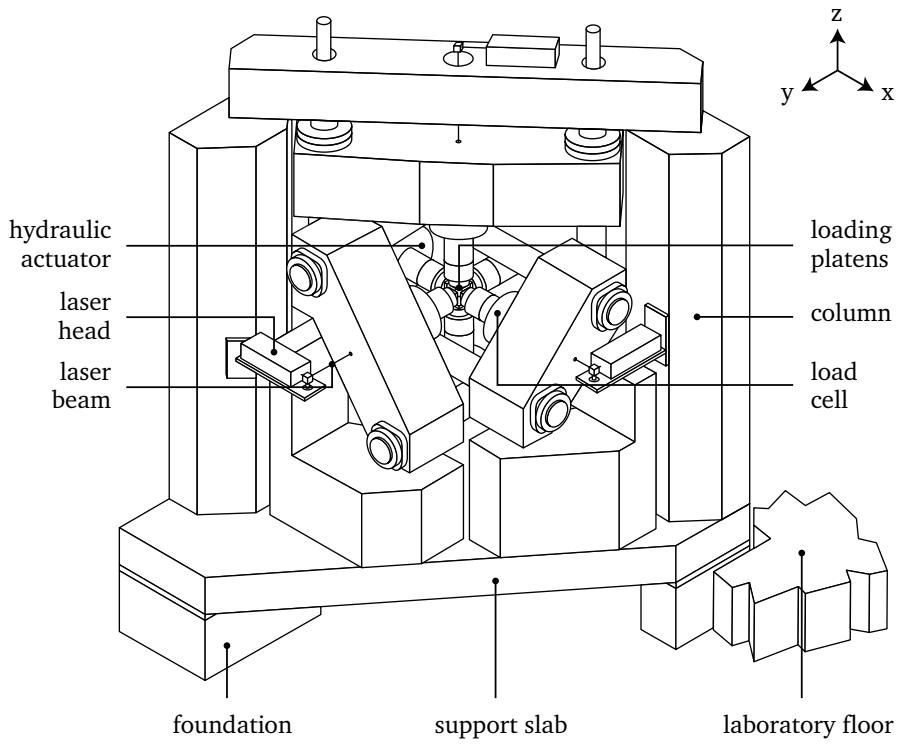


**Figure 3.6:** The mac$^{2T}$ test apparatus, after Petkovski et al. (2006).

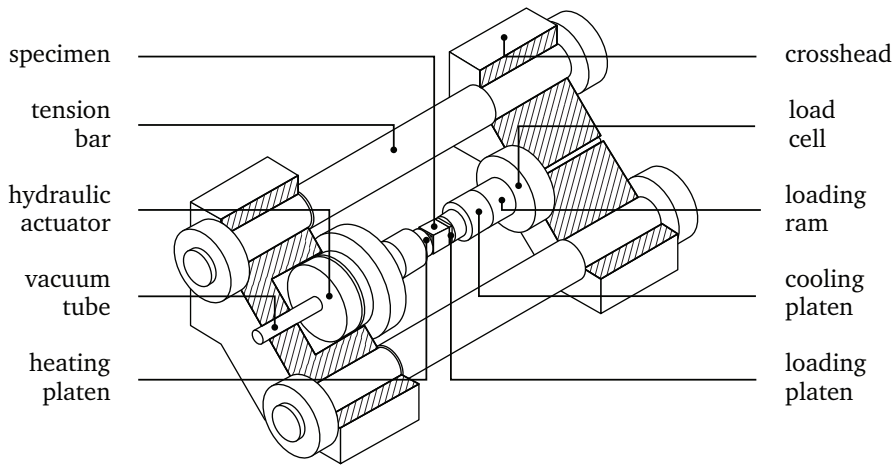


**Figure 3.7:** mac$^{2T}$ x-axis loading frame, after Petkovski et al. (2006). Hatching indicates a section cut.

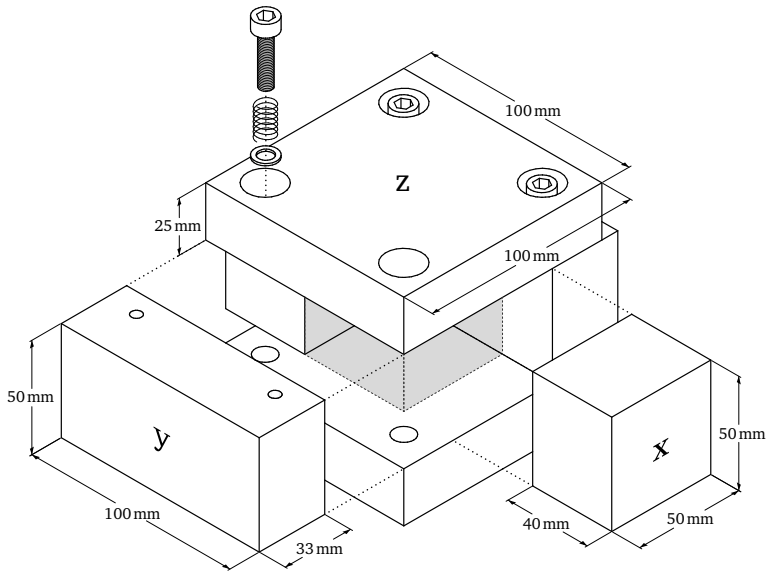


**Figure 3.8:** Sand loading box dimensions, assembly and axes convention. Specimen location is shaded.

tube to a retro-reflector attached to a 5 mm diameter steel pin. In tests on concrete this pin is in contact with the specimen surface, but in the current configuration is in contact with the sand test box.

Data acquisition and control of the loads, displacements and temperatures in the rig are managed by a purpose-built LabVIEW program, which is described in more detail by Petkovski et al. (2006).

### 3.4.2 Sand test box

In its original application, mac$^{2T}$ is used to test cubes of concrete under multi-axial loading conditions, where the strains involved are very small due to the high stiffness of concrete. In these tests a concrete cube is simply placed into the test apparatus and, as long as the loading platens are slightly smaller than the faces of the concrete cube, the test can be carried out without the platens ever touching. In testing sands, however, leaving such gaps between the platens would allow material to escape, and so a special loading box was fabricated to contain the sand during testing.

The test box is made up of six case-hardened steel blocks which can be arranged to form an interior cube, where the sand sample is placed. The dimensions and assembly of the box are depicted in Figure 3.8, which also shows the axis

convention used throughout this work. To assemble the box, four of the blocks are loosely secured together using bolts, springs and washers to form a void of $50 \times 50$ mm cross-section, into which the remaining blocks then slide. The bolts are countersunk in oversized holes which, along with the springs, hold the box together while allowing the blocks to move slightly relative to each other.

In the one-dimensional tests, only the x-axis blocks are actively stressed by the loading frame while the others are held at zero displacement, so that any stresses in the y- and z-axis blocks are generated passively by the x-axis loading. Because of this, the x-axis blocks are called the "active" blocks, while the y- and z-axis blocks are collectively called the "passive" blocks. As the applied stresses are very high, strains in the test box blocks are accounted for in calculations of specimen behaviour.

### 3.4.3 Specimen preparation

To provide an initial dry density of $1.5\,\mathrm{Mg\,m^{-3}}$, the specimens were prepared in the following manner.

a) Each of the six loading platens was fitted with a 1 mm thick steel plate coated in a 0.25 mm sheet of PTFE, in order to reduce friction-induced restraint at the interface with the test box.

b) The four passive blocks of the testing box were loosely secured together using bolts, springs and washers to allow approximately 1 mm of movement in each direction.

c) Propping the test box on shims, one of the active blocks was inserted so that only the top face of the box was open, and the blocks were squared up to create a void of $50 \times 50$ mm cross section.

d) To fix this cross-section, G-glamps were secured on the centre of the z-axis blocks and the bottom of the y-axis blocks so that the remaining active block would just slide in freely.

e) At this point the sand specimen was prepared to the required moisture content. The preceding assembly of the test box ensured that the wet specimens could be loaded immediately after mixing to prevent drying.

f) The specimen was added to the test box, the sand surface was levelled and the remaining active block carefully lowered in.

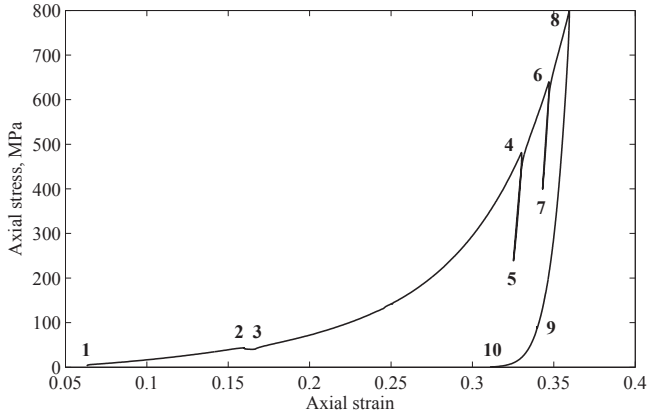


**Figure 3.9:** Example of quasi-static one dimensional compression test on dry medium sand: axial stress – axial strain relationship.

g) The specimen was compacted using hammer drops to reach a dry density of 1.5 Mg m$^{-3}$, which was found by measuring the protrusion of the top block from the test box.

h) The box was carefully rotated into the correct orientation for the test, the G-clamps released, and the test box loaded into mac$^{2T}$ .

### 3.4.4 Test sequence

In a one-dimensional compression test the specimen is deformed along one axis, while deformations in the other two directions are kept at zero. To achieve this in mac$^{2T}$, the load was applied in the x-axis under load control, while the other two axes were kept under displacement control, maintaining zero deformation. All tests were performed by following the same sequence:

a) As a small contact load is required to initialise the displacements measured by the interferometers, the y- and z-axis platens were loaded to 7 kN. This load was supported by the x-axis platens (see Figure 3.8). The specimen was then loaded to 7 kN (2.8 MPa) along the x-axis.

b) The y- and z-axes were switched to displacement control with a displacement rate of zero.

c) The specimen was loaded at a low rate of 20 MPa min$^{-1}$ to $\sigma_x = 40$ MPa. During this stage the strain rates reached maximum values of approximately $10^{-3}$ s$^{-1}$ (points 1–2 in Figures 3.9 and 3.10).

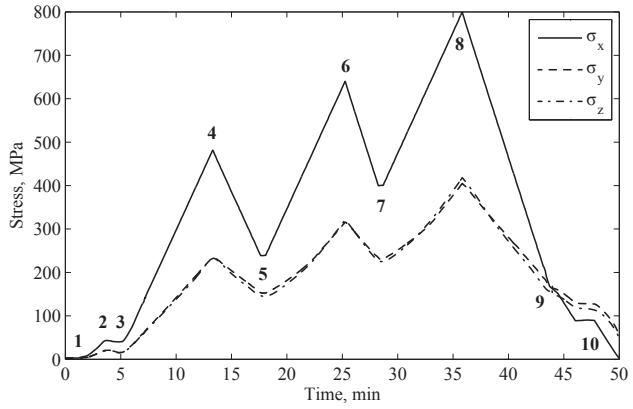


**(a)**

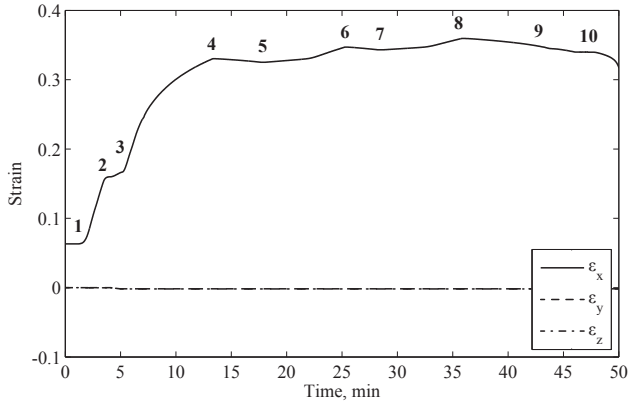


**(b)**

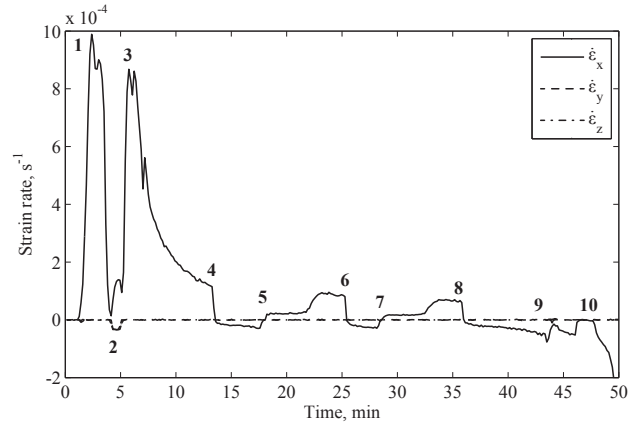


**(c)**

**Figure 3.10:** Example of quasi-static one dimensional compression test on dry medium sand: (a) stress history, (b) strain history and (c) strain rate history $\Delta\varepsilon/\Delta t$, calculated for $\Delta t = 10s$.

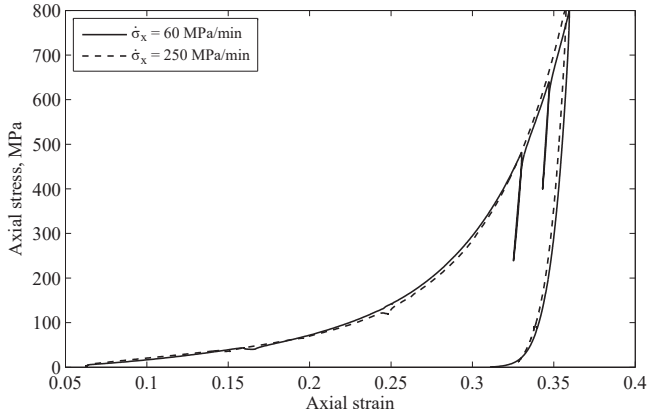


**Figure 3.11:** Stress–strain behaviour of medium sand at quasi-static loading rates of 60 MPa/ min and 250 MPa/ min.

d) The passive platens were backed off by 0.1 mm to ensure that friction between the active and passive blocks did not contribute to the stiffness of the soil specimen (points 2–3).

e) Loading to the peak axial stress of 800 MPa was carried out in three cycles (points 3–4, 5–6 and 7–8), at a constant loading rate of 60 MPa $\text{min}^{-1}$. The load cycles were carried out in order to determine the hysteretic behaviour of the soils, and to provide data for calculating the unloading stiffness at different stress levels.

   The strain rate in this part of the test varied between $10^{-3}$ $\text{s}^{-1}$ and $10^{-4}$ $\text{s}^{-1}$ as the soil stiffened during compaction. The sensitivity of the stress-strain behaviour to variations in quasi-static loading rates was investigated in a test where the axial stress was applied at 250 MPa $\text{min}^{-1}$. In this test the axial stress was increased monotonically following the adjustment in step (d), without unload-reload cycles. The stress-strain curve was identical to those in the tests where the specimen was loaded at 60 MPa $\text{min}^{-1}$, as shown in Figure 3.11.

f) To unload the specimen the axial stress was reduced until it was equal to the two minor stresses (points 8–9), and then all stresses were reduced to zero, so that the sample remained intact for further study (points 9–10).

## 3.5 High-strain-rate methodology

High-strain-rate one-dimensional compression tests were carried out to axial stresses of approximately 400 MPa using a split Hopkinson pressure bar. Soil specimens of nominal length 5 mm were laterally confined by a steel ring, which permitted the lateral stresses in the soil to be recorded; the maximum radial strain in the sand specimen was 0.05%, compared to axial strains of over 30%.

### 3.5.1 Split Hopkinson pressure bar

As discussed in §2.3, the SHPB consists of two long, cylindrical EN24T steel bars with the sand specimen placed between them. The SHPB is struck from one end by a steel striker bar fired from a gas gun, so that a compressive stress pulse propagates through the system. Strain gauges on the bars and the steel confining ring record this pulse and its reflections, enabling information on the response of the test specimen to be obtained. A schematic of the rig used in the current work is shown in Figure 3.12, noting the positions of the strain gauges and the naming convention for the bars. The incident and transmitter bars are each 25 mm in diameter and 1500 mm in length, while the striker bar is 25 mm in diameter and 400 mm in length. The three bars are held in alignment by a series of linear bearings, which are mounted on a length of aluminium channel section. Acceleration of the striker bar is achieved using a gas gun fitted with a brass diaphragm and nylon piston, and the movement of the transmitter bar is restricted by a back stop containing blocks of expanded polystyrene.

To calibrate the individual pressure bars, the incident signal from the impact of a striker of known velocity (calculated using high-speed photography) was compared with the theoretical strain in the bar given by the relationship

$$\varepsilon_b = \frac{v_s}{2c_0} \tag{3.3}$$

where $\varepsilon_b$ is the longitudinal strain in the bar, $v_s$ is the velocity of the striker bar on impact and $c_0$ is the longitudinal wave speed in the bar. The wave speed can be found by using the expression

$$c_0 = \frac{2l}{t} \tag{3.4}$$

where $l$ is the distance between the strain gauge and the specimen end of the bar and $t$ is the time between the incident and reflected pulses. A gauge factor, $F$, is calculated to define the ratio between the voltage across the gauge's Wheatstone

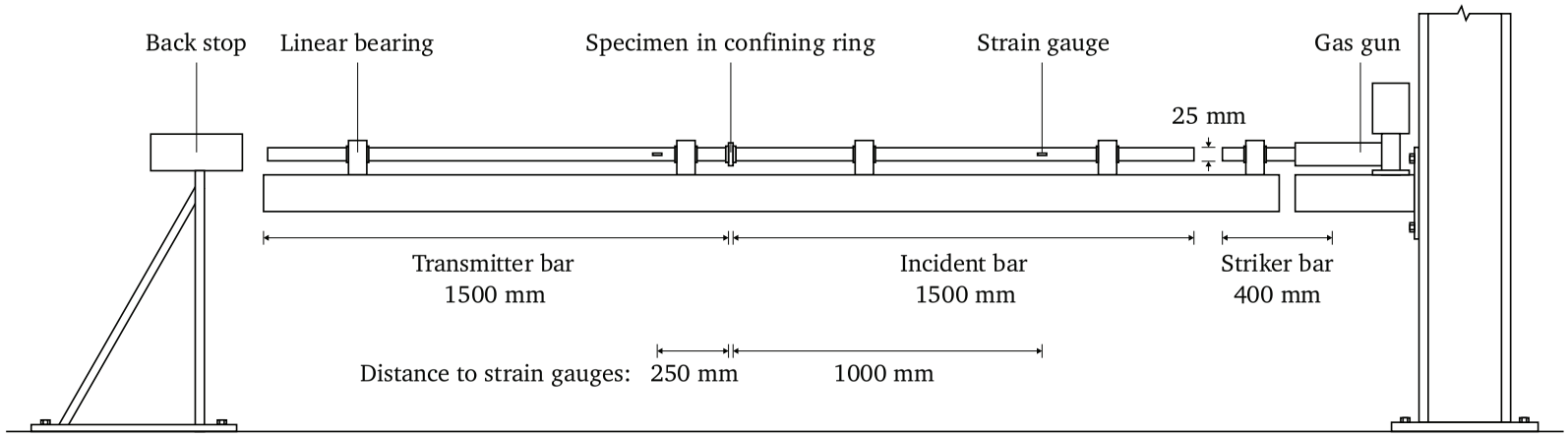


**Figure 3.12:** Schematic of SHPB test rig prepared for a test.

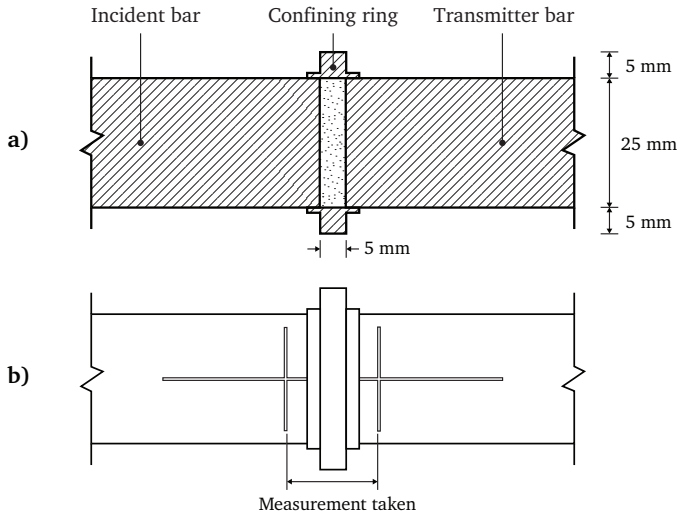


**Figure 3.13:** Steel confining ring a) axial section, and b) axial elevation showing markings used for specimen measurement.

bridge and the strain in the bar calculated from Equation 3.3:

$$F = \frac{2V_o}{\varepsilon V_i} \tag{3.5}$$

where $V_i$ and $V_o$ are the input and output voltages across the Wheatstone bridge, respectively (see §3.5.3).

### 3.5.2 Confining ring

The soil specimens were held in a steel confining ring with a 25 mm internal diameter and 35 mm external diameter over a length of 5 mm, as depicted in Figure 3.13. On each side of the ring 1 mm thick locating flanges aided positioning on the pressure bars and prevented soil loss. A strain gauge located on the outside surface of the ring enabled the circumferential strain of the ring to be measured and, using thick walled pipe theory, the average internal pressure in the sample could be related to the circumferential strain using the expression

$$P_i = \frac{r_o^2 - r_i^2}{2r_i^2} E\varepsilon_\theta \tag{3.6}$$

where $P_i$ is the internal radial pressure exerted on the specimen by the confining ring, $E$ is the Young's modulus of the ring, $\varepsilon_\theta$ is the circumferential strain measured on the outside of the ring and $r_o$ and $r_i$ are the outer and inner radii of the

ring respectively (Stephens 1970). For the current arrangement, $P_i = 0.48E\varepsilon_\theta$. It is important to note that the length of the sand specimen changes significantly during the test, typically by up to 30%. To take this into account, the average internal pressure deduced from the circumferential strain was factored by the length of the confining ring (5 mm) divided by the varying sample length to obtain the radial pressure acting on the shortened length of sample. This test setup allowed both axial and radial stresses and strains within the sample to be recorded, and the one-dimensional nature of the test conditions to be verified.

The position of the strain gauge changes relative to the mid-point of the specimen during the test, as the incident bar end of the specimen begins to move while the transmitted bar end is still stationary. Assuming that the confining ring is stationary throughout the specimen loading, in a representative test the centre of the specimen moves approximately 1.0 mm relative to the strain gauge. The wall thickness (5 mm) of the confining ring also has the effect of spreading a load applied to one surface over a larger area on the other, so that the measurement of radial stress at the strain gauge may be an average over a length of several millimetres inside the ring. As a result, the movement of the specimen relative to the strain gauge will have a reduced effect, and the stress measured by the gauge should be representative of the stress experienced on the radial surface of the sand specimen.

### 3.5.3 Instrumentation and signal processing

The instrumentation of the SHPB tests is represented diagrammatically in Figure 3.14. Strains in the pressure bars and the confining ring were measured using Kyowa KSP-2-120-E4 semiconductor strain gauges, the properties of which are listed in Table 3.3. One gauge was fixed to the surface of the confining ring (Figure 3.15a), and four gauges were placed on each bar (Figure 3.16a), arranged so that strains due to bending would be eliminated and only longitudinal strains would be measured.

An analogue voltage signal was produced by incorporating each set of strain gauges into a Wheatstone bridge, shown for the ring and bars in Figures 3.15b and 3.16b respectively. In each Wheatstone bridge the dummy gauges were adjustable to allow small temperature-induced strains to be balanced out before initiating the experiment.

The output signal was amplified and then recorded using a TiePie Handyscope four-channel digital oscilloscope, where the associated Multi Channel PC software was used to take samples at 14-bit A-D resolution and at a sample rate of

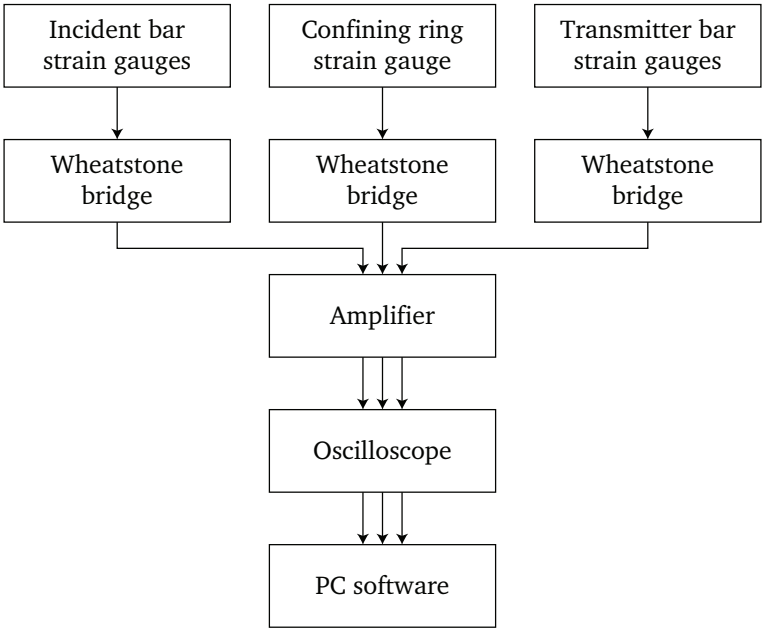


**Figure 3.14:** SHPB signal processing.

| Property | Value |
|---|---|
| Gauge pattern | Uniaxial |
| Resistive material | P-type silicon |
| Gauge length | 2 mm |
| Gauge factor | Approx 120 |
| Gauge resistance | 120 Ω |
| Base size | 7.7 × 4 mm |
| Base material | Paper, phenol-epoxy |

**Table 3.3:** Properties of Kyowa KSP-2-120-E4 semiconductor strain gauge.

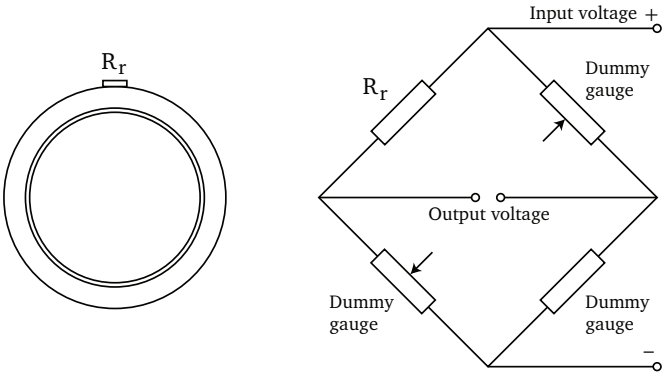


**Figure 3.15:** Confining ring a) strain gauge arrangement, b) Wheatstone bridge.

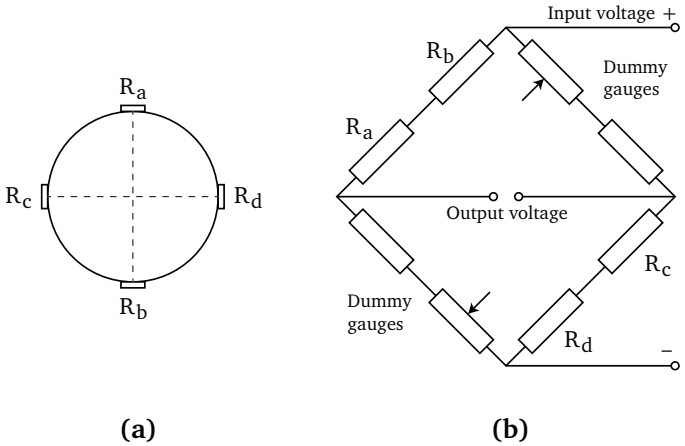


**Figure 3.16:** Split Hopkinson pressure bar a) strain gauge arrangement (bar cross-section), b) Wheatstone bridge.

781.25 kHz. The recorded output voltages were used to calculate the strain in the bars and ring using the equations

$$\varepsilon_{\text{bar}} = 2\frac{V_o}{FV_i} \tag{3.7}$$

$$\varepsilon_{\text{ring}} = 4\frac{V_o}{FV_i} \tag{3.8}$$

where $V_i$ is the input voltage, $V_o$ is the output voltage and $F$ is the gauge factor.

These strains were processed to find the response of the soil specimen by a implementing a dispersion-correction method, which is described in detail in Chapter 4. This method was implemented to improve the measurement of the axial stress in the specimen, as data processing using one-dimensional wave theory introduced large spurious oscillations in the stress at the front face of the specimen, preventing calculation of a representative mean axial stress. The medium sand data in this chapter was published before the implementation of this dispersion-correction method (Barr et al. 2016). In the published work the stress at the back face of the specimen was used to represent specimen behaviour due to the large oscillations in front stress.

### 3.5.4 Specimen preparation

To load a sand specimen into the gauged ring:

a) The transmitter bar was placed vertically into a purpose-made jig which ensured that the end of the transmitter bar was flush with the inside edge of the non-flanged part of the ring.

b) A thin (10 µm thick, 0.01 g) aluminium foil disk was placed on the face of the pressure bar inside the gauged ring, and the 3.5 g sand sample carefully poured into the ring and tamped down using a short length of 25 mm diameter bar.

c) A second foil disk was placed on top of the soil sample and also tamped down, then secured to the confining ring using a very small amount of cyanoacrylate adhesive, confining the specimen. The strength and mass of the foil disks was taken to be negligible, though the thickness of the disks (20 µm in total) was considered when measuring the length of the specimen.

d) The transmitter bar was carefully removed from the jig and placed into the linear bearings, and the specimen in the confining ring brought into contact with the incident bar ready for testing.

In previous tests using a confining ring, the length of the sample was found by measuring the distance between a pair of dots marked onto the bars using an awl (Rigby and Tyas 2012). Using digital callipers, the distance could at best only be considered as measured to the nearest 50 μm, as the dots themselves had a non-trivial diameter, and the method relied on consistently lining the callipers up to the exact same point. It was noted that the processed data was particularly sensitive to the recorded pre-test length of the specimen: a ±50 μm tolerance in the measured length results in a $\pm 0.04\,\mathrm{Mg\,m^{-3}}$ error in density measurements.

In the current tests, the incident and transmitter bars were each marked with a pair of perpendicular lines by using a sharp blade, as shown in Figure 3.13b. The distance between the inside edges of these lines was then measured using a travelling microscope fitted with a digital dial gauge. While the lines themselves had a width of about 500 μm, the microscope enabled measurements to be taken between the same points consistently which, along with ±1 μm accuracy offered by the digital dial gauge, allowed measurements to be taken within ±10 μm.

### 3.5.5 Test sequence

Stress pulses were applied using a striker bar accelerated by a gas gun, which was set up in a consistent manner to ensure a similar peak axial stress and strain rate in each test:

a) A nylon piston was inserted 100 mm into the barrel of the gas gun.

b) The barrel was screwed onto the gas gun, and a 0.2 mm thick brass diaphragm was fitted between the reservoir and the barrel.

c) The striker bar was inserted into the barrel until it was in contact with the piston.

d) The Wheatstone bridges were balanced to correct for any temperature-induced strain in the bars, and the oscilloscope was primed.

e) The reservoir was filled until the diaphragm ruptured, initiating the test.

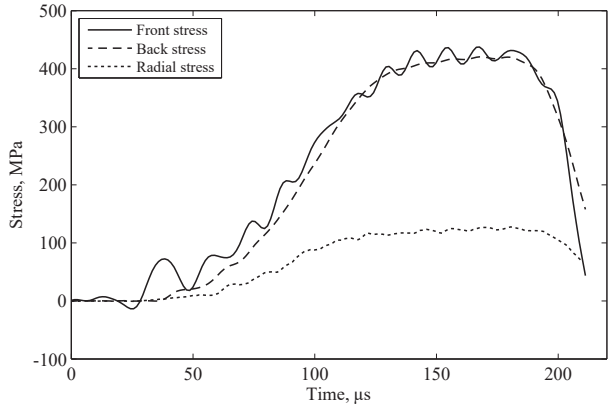


**(a)**

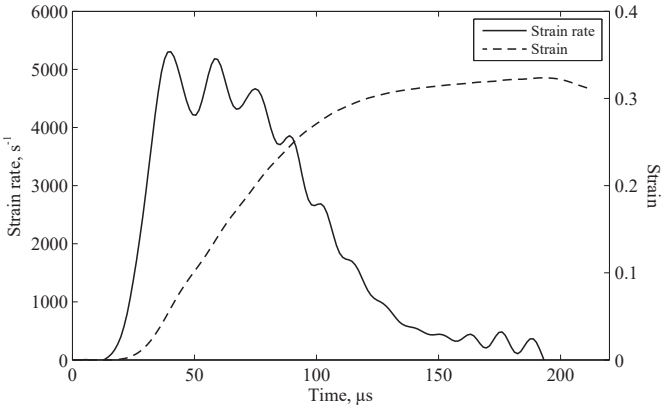


**(b)**

**Figure 3.17:** Typical histories from a dry SHPB test on medium sand a) axial and radial stress, b) strain and strain rate.

This setup typically provided impact velocities of $22\,\mathrm{m\,s^{-1}}$, and incident pulses of 350 MPa to 400 MPa over 200 µs. Typical histories of stress and strain in the dry SHPB tests are shown in Figure 3.17, where the axial strain rate typically fell from $5200\,\mathrm{s^{-1}}$ at the start of loading to $1000\,\mathrm{s^{-1}}$ at the maximum stress, resulting in a mean strain rate of $2900\,\mathrm{s^{-1}}$.

The strain rate imposed on the specimen is a function of both the magnitude of the loading pulse and the stiffness of the specimen. For materials whose stiffness varies by relatively small amounts during a SHPB experiment, it is possible to alter the shape of the incident wave to approximate a constant strain rate during the loading (Nemat-Nasser et al. 1991, Frew et al. 2005). However, for the highly compressible sands under investigation in this study, the stiffness varies by around an order of magnitude over the duration of the SHPB test, and while pulse shaping techniques for materials as compliant as this may be possible in theory, they have not been reported in practice. The variation in strain rate over the course of the SHPB experiment is deemed acceptable as the intention of this work is to identify first-order differences between quasi-static and high strain rate regimes, noting that it is six orders of magnitude higher than that applied in the quasi-static experiments.

## 3.6 Results and discussion

As this test programme contains three independent variables, the results will be analysed by considering each in turn. First, the response of the three soils in quasi-static one-dimensional compression will be analysed in terms of their compressibility and response to loading cycles. The effect of strain rate on dry specimens of each soil will then be considered, followed by the effect of moisture content on the strain-rate sensitivity of the medium sand.

### 3.6.1 Quasi-static compressibility

Following quasi-static one-dimensional compression to 800 MPa, all three soils could be removed from the test box as a block of solid material, as shown in Figure 3.18. These blocks remained intact under significant unconfined loading, even though the sand used in the tests was dry and cohesionless. For example, a block of medium sand tested in a state of uniaxial stress along the original loading axis failed at a stress of 3.2 MPa. It is possible that interlocking of the sand particles and electrostatic effects may both contribute to the new cohesive strength, but this has not been investigated as part of this work.

**Figure 3.18:** Dry medium sand after one-dimensional compression to 800 MPa.

The results of the quasi-static tests are shown in $e$–$\log \sigma_x$ space in Figure 3.19. The initial loading of the specimens is incomplete due to the 3 MPa load applied to locate the interferometers, but the results agree well from test to test, with a few exceptions. The tests on coarse sand (Tyas and Rigby 2012) were the first to be carried out using mac$^{2T}$ as a soil testing rig, and several preliminary tests had issues with friction between the test cube blocks at higher stresses: these are shown as dashed lines in Figure 3.19c. The friction effects do not seem significant in $e$–$\log \sigma_x$ space, but significantly stiffen the apparent material behaviour when mean stresses are considered in later sections, and so these tests will be excluded from those analyses. In one test on sandy loam (Figure 3.19a) a measurement error appears to have shifted the compressibility curve along the void ratio axis, and so this will also be excluded.

The grey markings on the surface of the sand block in Figure 3.18 are evidence of friction with the interior of the steel test box. These markings are particularly noticeable on the edges of the y- and z-axis faces, which moved approximately 8 mm from their original position during the test. To assess whether this friction significantly affected the test results, a test on medium sand was repeated with a shorter 30 mm specimen, the shortest length possible using the current test box. This test is shown in Figure 3.19b as a dotted line. The 30 mm specimen is slightly stiffer than the 50 mm specimens at lower stresses, but this may be due to the additional 20 mm of steel-on-steel contact inside the test box before the passive blocks are backed off (§3.4.4). The behaviour of the 30 mm and 50 mm specimens is very similar at higher stresses, and so friction does not appear to have significantly affected the test results in the 50 mm specimens.

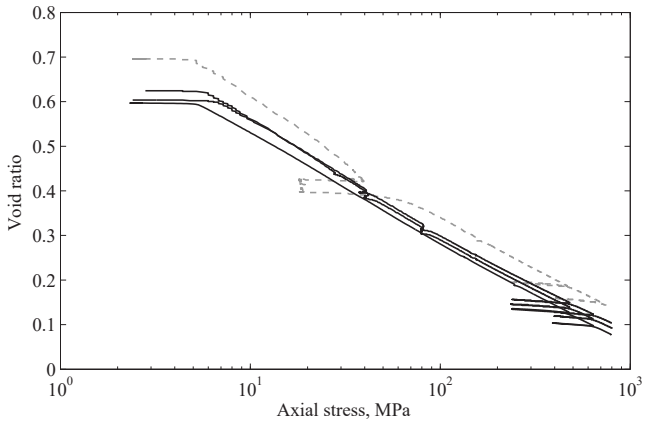


**(a)** Sandy loam

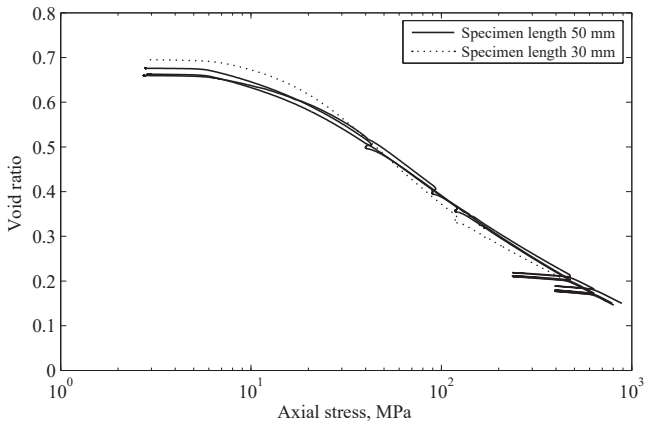


**(b)** Medium sand

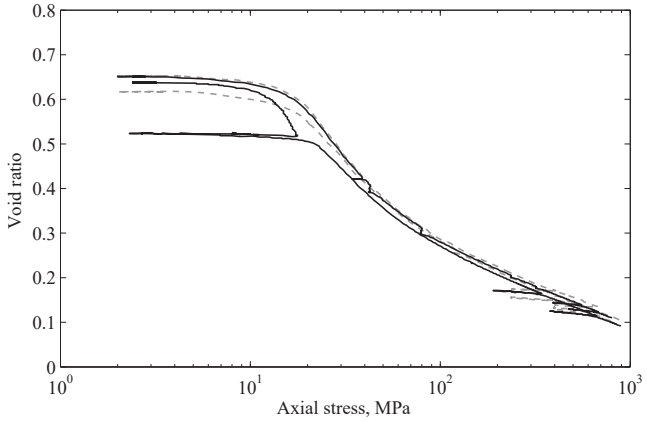


**(c)** Coarse sand

**Figure 3.19:** Quasi-static one-dimensional compression tests on a) sandy loam, b) medium sand and c) coarse sand. Dashed lines represent rejected tests.

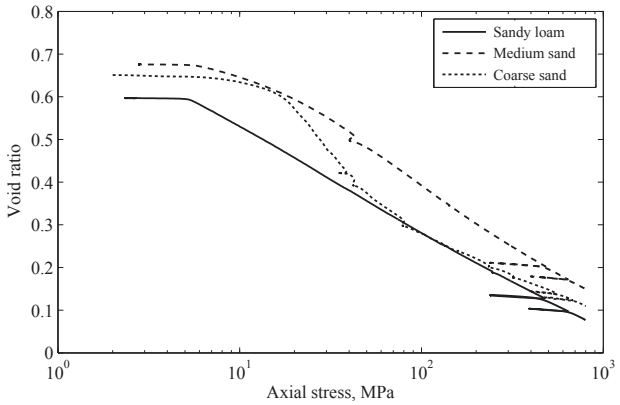


**(a)**

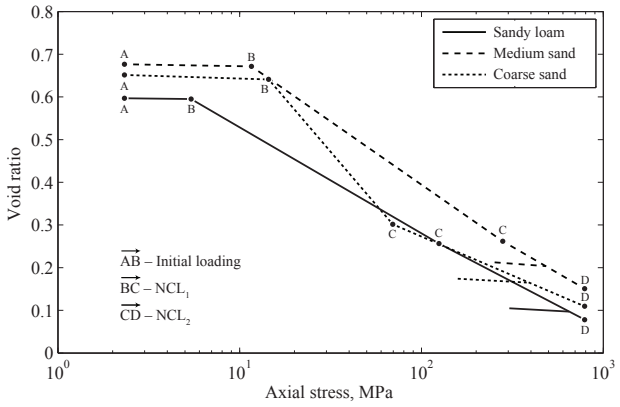


**(b)**

**Figure 3.20:** Comparison of quasi-static one-dimensional compression tests on sandy loam, medium sand and coarse sand: a) representative data, b) idealised NCLs.

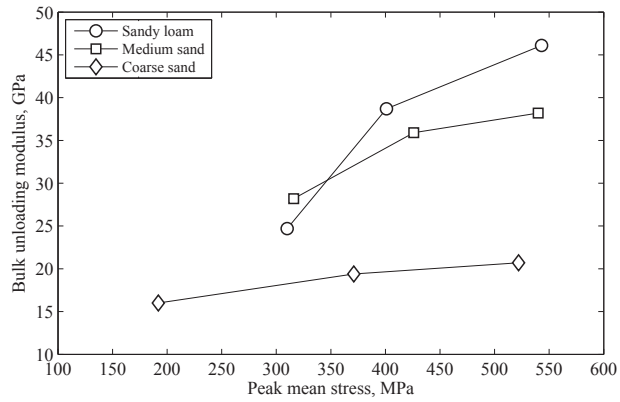


**Figure 3.21:** Variation of the bulk unloading moduli with peak mean stress.

A comparison of representative tests on each soil is shown in Figure 3.20a. At axial stresses of 800 MPa the soils achieved void ratios between 0.08 and 0.15, equating to dry densities between 2.31 $\mathrm{Mg\,m^{-3}}$ and 2.43 $\mathrm{Mg\,m^{-3}}$. Figure 3.20b shows the idealised response of the three soils, which are observed to follow the one-dimensional compression response discussed in §2.4.1. In each case initial loading, *AB*, is followed by convergence on a unique NCL, *BCD*, which is approximately bi-linear. The soil response in *CD* is stiffer than in *BC*, and appears to replicate the behaviour observed by Hagerty et al. (1993), which was related to decreasing particle breakage due to an increasing coordination number.

In terms of secant stiffness (calculated using only the current stress state and the origin), the uniform medium sand behaved most stiffly throughout the tests, followed by the uniform coarse sand, and then the well-graded sandy loam; however, the tangent stiffness of the coarse sand was much lower than in the other soils during the first section of the NCL. If the majority of particle breakage takes place over *BC* this reduced stiffness could be due to the increased probability of breakage in the coarse sand, which contains relatively large, uniformly-sized particles (McDowell et al. 1996).

The tangent stiffness (calculated over the last small stress increment) of the three soils is very similar over *CD*, and the void ratio at *C* is similar in each soil, at approximately 0.3. This may indicate that the soils have developed a similar PSD through particle breakage but this cannot be confirmed, as post-test particle size analyses were not carried out on the coarse sand or silty loam.

The stiffness along the elastic unload–reload lines (URLs) increases as the peak stress experienced by the soils increases, as shown by the increasing bulk unloading moduli in Figure 3.21. This increased stiffness is associated with the reducing void ratio with increasing stress, which increases the area of stress-bearing material in a given cross-section. The sandy loam and medium sand have similar bulk moduli and exhibit similar increases with stress, while the coarse sand is less stiff and exhibits a smaller increase with stress. This could be due to the similar PSDs of the sandy loam and medium soil, and the presence of stiffer rock fragments which are absent in the coarse sand.

The slope of the NCLs and URLs can be defined using the compression and swelling indices, which have units of $\mathrm{MPa^{-1}}$. Mean values of $C_c$ and $C_s$ are provided for the three soils in Table 3.4. The equations of the NCLs are then given by the following, where $e_0$ is the void ratio at $\sigma_x = 1\,\mathrm{MPa}$:

$$e = \begin{cases} e_{0,1} - C_{c,1} \log_{10} \sigma_x & e \geq 0.3 \\ e_{0,2} - C_{c,2} \log_{10} \sigma_x & e < 0.3 \end{cases} \tag{3.9}$$

### 3.6.2 Effect of strain rate in dry soil

While it is common geotechnical practice to plot one-dimensional compression tests as semi-logarithmic graphs of void ratio against axial stress, the majority of the existing literature on strain-rate effects presents results as graphs of axial stress against axial strain. To facilitate comparison with the high-strain-rate literature the results in this section are expressed in terms of both void ratio and dry density, which has the same form as strain but allows a comparison between the current density and the maximum density achievable.

Where density is considered, dry density ($\rho_d = M_s/V$) is used to compare test series rather than bulk density ($\rho = M/V$), as partially-saturated specimens would otherwise automatically appear to be less stiff due to the additional mass. As there is no record of the changing mass of the specimen, use of bulk density would also be inaccurate if any pore water is lost. This is shown schematically in Figure 3.22, where the dry density increases with stress until all pores are removed ($e = 0$) and the density is that of the quartz mineral. Over the same stress range the bulk density is proportionally larger than dry density until the sand reaches full saturation and pore water begins to be drained, reducing both the moisture content and mass of the specimen and causing the bulk density to approach the dry density at $e = 0$. An assumption of constant mass while using bulk density leads to erroneously large values at full saturation.

#### Axial stress measurements

Axial stress–dry density data is presented in Figure 3.23 for the quasi-static mac$^{2T}$ tests and dynamic SHPB tests, where in all three soils the dynamically-tested specimens appear to respond more stiffly. This stiffening is particularly pronounced in the coarse sand. The same data is presented in $e - \log \sigma_a$ space in Figure 3.24, where in each soil the dynamic series forms an NCL which is largely parallel to the quasi-static response, similar to the strain-rate behaviour observed in clays (Bjerrum 1967).

The SHPB results show more variation than the quasi-static tests, perhaps due to the smaller specimen size, but the two strain rates form distinct series, and do not overlap except near the peak stress in the tests on medium sand. This convergence is associated with the part of the test where the peak stress is maintained for 80 µs to 100 µs, and the strain rate reduced to approximately 500 s$^{-1}$, as seen in Figure 3.17.

It is noted that while the mac$^{2T}$ tests were fully drained, the loading of the SHPB specimens more closely resembled undrained conditions, with little opportunity

| | Sandy loam | Medium sand | Coarse sand |
|---|---|---|---|
| $e_{0,1}$ | 0.82 | 0.99 | 1.22 |
| $C_{c,1}$ | 0.26 | 0.30 | 0.50 |
| $e_{0,2}$ | 0.74 | 0.85 | 0.66 |
| $C_{c,2}$ | 0.22 | 0.24 | 0.19 |
| $C_s$ | 0.033 | 0.031 | 0.041 |

**Table 3.4:** Coefficients of compressibility for the three soils. Values of $e_0$ are taken at 1 MPa, and the subscripts 1 and 2 relate to $NCL_1$ and $NCL_2$.

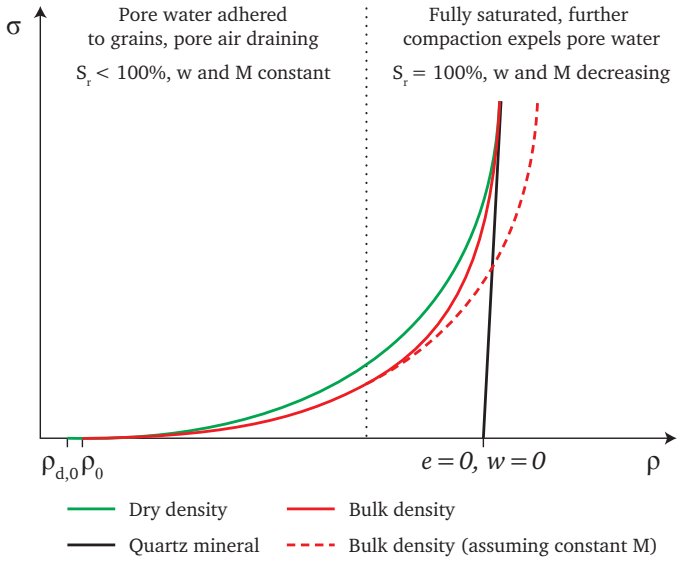


**Figure 3.22:** Schematic comparison of dry density and bulk density responses in a partially-saturated sand.

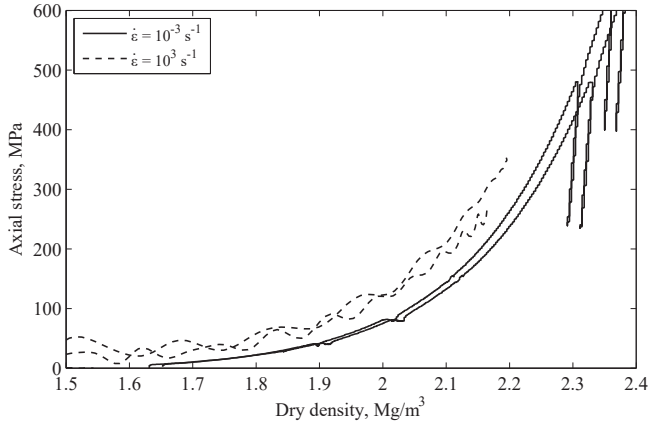


**(a)** Sandy loam

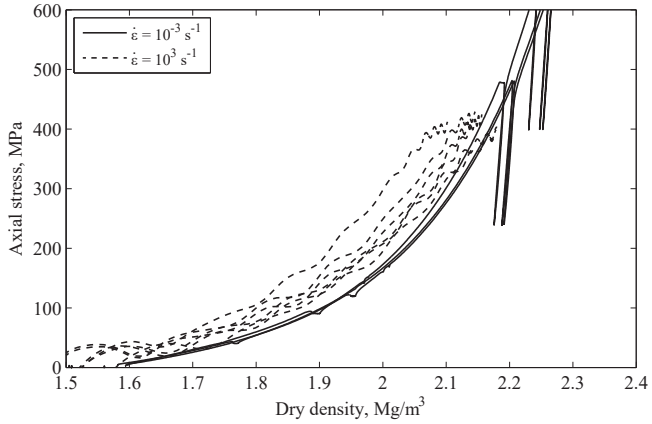


**(b)** Medium sand

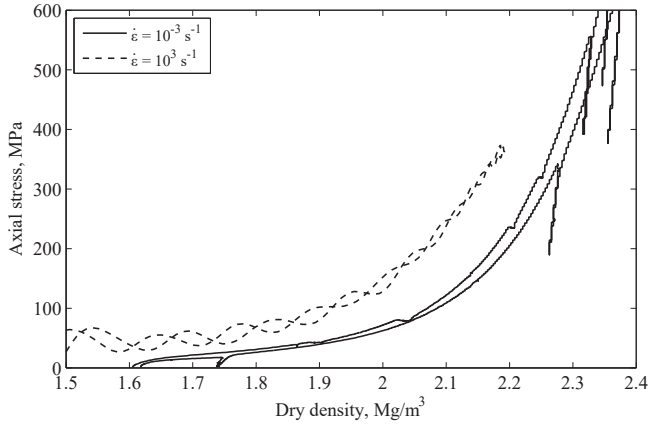


**(c)** Coarse sand

**Figure 3.23:** Quasi-static and high-strain-rate one-dimensional compression tests on dry a) sandy loam, b) medium sand and c) coarse sand, presented as axial stress against dry density.

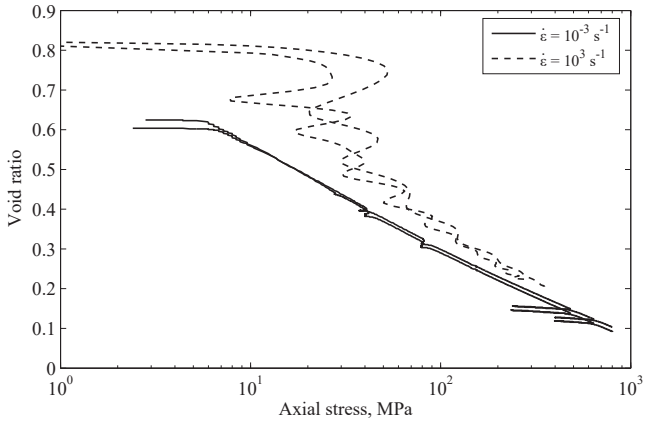


**(a)** Sandy loam

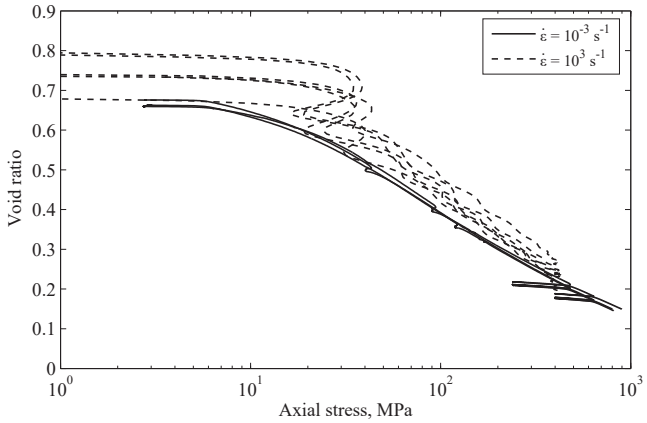


**(b)** Medium sand

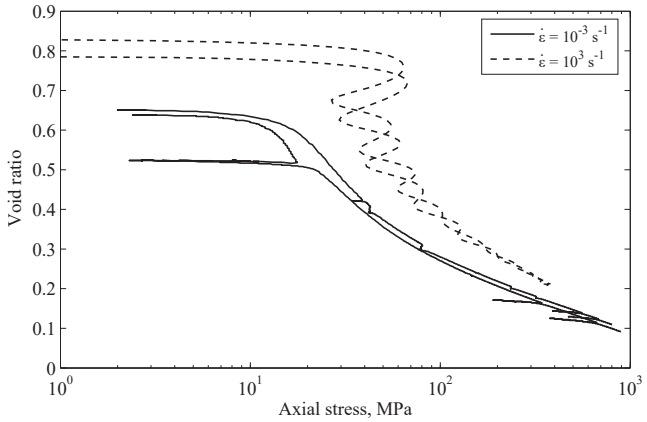


**(c)** Coarse sand

**Figure 3.24:** Quasi-static and high-strain-rate one-dimensional compression tests on dry a) sandy loam, b) medium sand and c) coarse sand, presented as void ratio against axial stress.

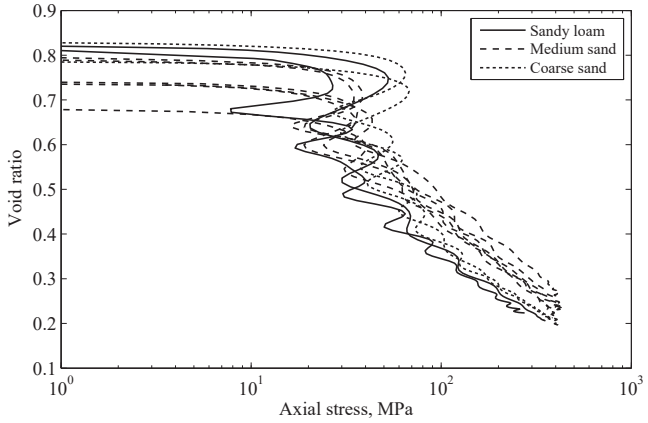


**Figure 3.25:** High-strain-rate one-dimensional compression tests on dry sandy loam, medium sand and coarse sand, presented as void ratio against axial stress.

for the escape of pore air. The resulting compression of pore air contributes to the stiffness of the specimen at higher strains, but a calculation based on ideal gas behaviour in undrained conditions shows this contribution to be negligible. The compression of air observed at 2.1 $\mathrm{Mg\,m^{-3}}$ in the medium sand would require an additional pressure of 190 kPa, a small fraction of the 80 MPa mean increase in axial stress.

A comparison of the high-strain-rate response of the three soils is shown in Figure 3.25. The behaviour at low stresses is dominated by inertia (see below, and §4.3.5), and so the effect of particle size distribution does not appear to be significant. At higher stresses a similar trend to the quasi-static experiments emerges, with the uniform medium sand behaving more stiffly than the coarse sand and the well-graded sandy loam.

### Radial stress measurements

Examples of the radial stresses recorded in the SHPB tests are shown in Figure 3.26. Six of the ten dry SHPB tests contain an additional negative pulse at the beginning of the radial stress recording (*e.g.* Figure 3.26a), which obscures the actual signal at that point, and appears to attenuate the remainder of the signal compared to unaffected signals (*e.g.* Figure 3.26b). These troughs denote a circumferential compression in the ring of 5 MPa to 25 MPa, which is impossible under the current loading conditions, suggesting that their source is electrical in nature.

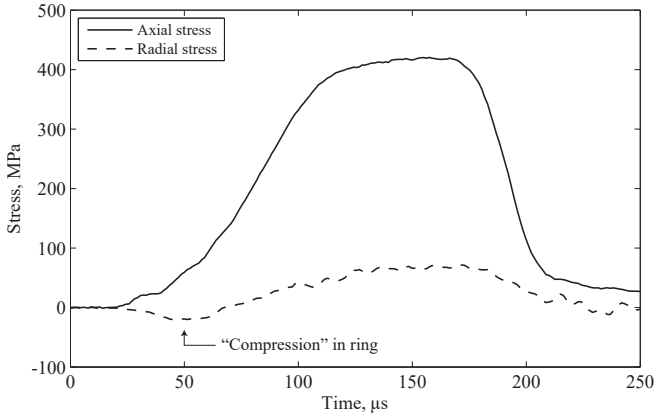


**(a)**

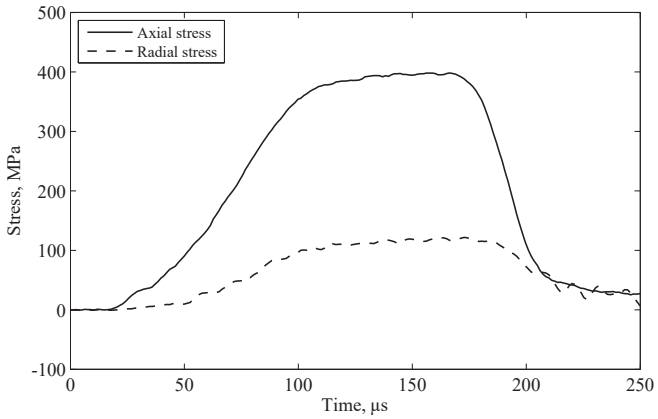


**(b)**

**Figure 3.26:** Examples of axial and radial stresses in SHPB experiments on medium sand a) where EMF interference has introduced additional features in the radial stress signal, b) without EMF interference.

Similar troughs were observed in transient Hopkinson bar signals by Meitzler (1956) and Vigness (1956), and were identified as being due to magnetostrictive effects in the wire strain gauges. Magnetostriction is an effect observed in magnetic materials where a change in the magnetic state of the material results in a change in its length, due to the realignment of magnetic domains. The strain due to magnetostriction increases with the strength of the magnetic field up to a saturation strain, where all domains have been aligned with the field. The reciprocal Villari effect occurs when a change in the length of a magnetic material results in a change in its magnetic state, which can in turn induce a current in the material.

While magnetostrictive effects can account for fluctuations in the signal from ferromagnetic wire gauges, the semiconductor strain gauges used in the current experiments use P-type silicon as the resistive element. Here the change in resistance with strain is almost entirely due to the effect of piezoresistance rather than the change of geometry: straining the gauge affects the interatomic spacing in the resistive element, making it easier or harder for electrons to be raised into the conduction band (Fraser 1986). The gauge, leadwires and other cables forming the strain gauge circuit, however, remain susceptible to induced currents from simple electromagnetic induction. The source of a fluctuating magnetic field in this case could be the steel bars, confining ring or a nearby electrical source. Cress et al. (1987) demonstrated that the fracture of many types of rock are accompanied by electrical activity due to the relative movement of charged surfaces, and so the fracture and movement of sand particles may itself be a magnetic source. Chapter 4 will introduce experiments which identify the pressure bars as the main source of the additional signals, and concludes that it is not possible to reliably correct for the additional features in the current experiments.

The apparent Poisson's ratio of each soil specimen is shown in Figure 3.27, calculated by solving Hooke's Law in its three-dimensional form

$$\begin{aligned}
\varepsilon_1 &= \frac{1}{E}(\sigma_1 - \nu(\sigma_2 + \sigma_3)) \\
\varepsilon_2 &= \frac{1}{E}(\sigma_2 - \nu(\sigma_1 + \sigma_3)) \\
\varepsilon_3 &= \frac{1}{E}(\sigma_3 - \nu(\sigma_1 + \sigma_2))
\end{aligned} \tag{3.10}$$

where $E$ is Young's modulus and $\nu$ is Poisson's ratio. It is clear that repeatable radial measurements were not achieved in the case of sandy loam and coarse sand, and so the following comments apply only to the medium sand.

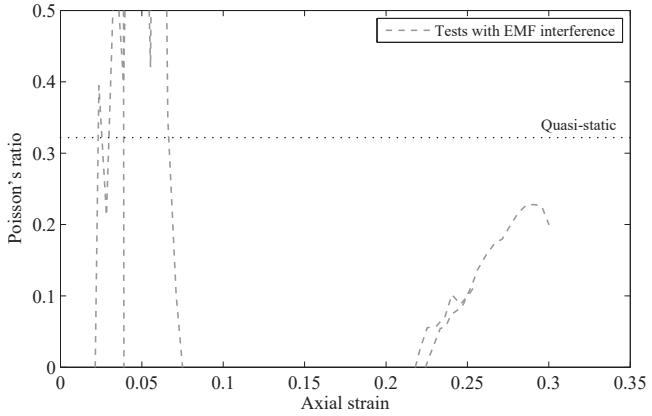


**(a)** Sandy loam

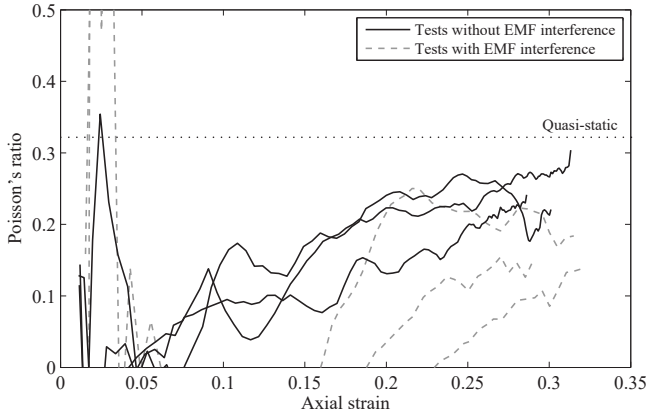


**(b)** Medium sand

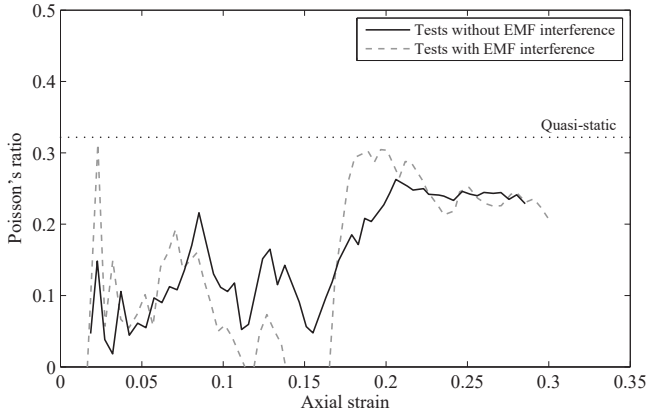


**(c)** Coarse sand

**Figure 3.27:** Apparent Poisson's ratio of a) sandy loam, b) medium sand and c) coarse sand in SHPB tests. Dashed lines indicate tests where EMF interference has introduced additional peaks or troughs in the radial stress signal.

While the quasi-static specimens exhibited a stable Poisson's ratio of between 0.30 and 0.33, the Poisson's ratio of the SHPB specimens varied throughout the test, typically rising from approximately zero to a value between 0.25 and 0.30. Large fluctuations are present in the calculated Poisson's ratio at low strains, due to the stresses at that point being similar in magnitude to the signal noise, but these are also centred around a Poisson's ratio of zero, indicating that the specimen is compressing axially without an accompanying lateral expansion. This deviation from the quasi-static behaviour suggests that an inertial effect is restricting radial displacement within the specimen.

When a specimen is loaded in uniaxial strain, information about the boundary conditions takes a small but finite time to reach the interior from the surface. In quasi-static experiments this occurs far faster than the rate at which loading is applied; however, in the SHPB experiments this period is comparable to the loading duration, and so inertial forces can be expected to influence the behaviour of the specimen. In the early stages of loading the steel ring only acts to confine a small annulus of material on the surface of the specimen, while the interior is confined inertially. A relief wave propagates inwards from the surface, permitting the interior of the specimen to accelerate radially and contribute to the loading in the ring, and causing the radial stress measured on the surface of the ring to develop over time.

Inertial confinement in the specimen increases the axial stress required to achieve a given axial strain, in the same way that a higher cell pressure in a triaxial test on soil increases the axial stiffness of the specimen. This mechanism could account for the increase in axial stiffness observed between the quasi-static and dynamic specimens: similar effects have previously been documented in materials such as rock (Young and Powell 1979) and plain concrete (Bischoff and Perry 1991), where apparent increases in material strength at high strain rates were attributed to the transition from uniaxial stress to uniaxial strain. This mechanism also appears to be supported by Figure 3.28, which shows the volumetric response of the medium sand using a mean stress, $\bar{\sigma}$, calculated using both axial and radial stresses:

$$\bar{\sigma} = \frac{\sigma_a + 2\sigma_r}{3}. \tag{3.11}$$

Here the dynamically-tested specimens show very little increase in stiffness over the quasi-static tests, and with considerable overlap between the two series, suggesting that while the distribution of stresses within the specimen has varied with strain rate, the volumetric response remains the same.

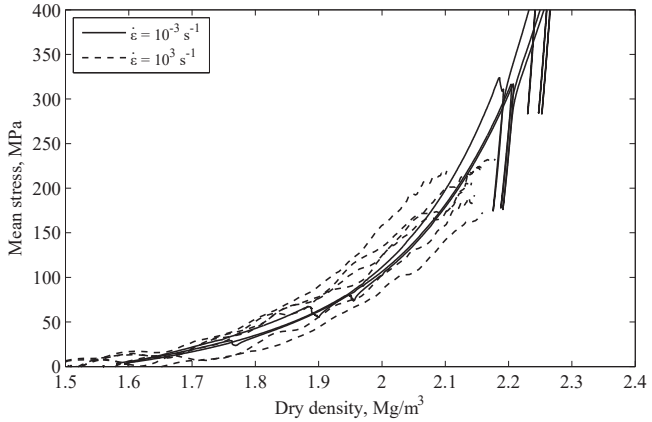


**(a)**

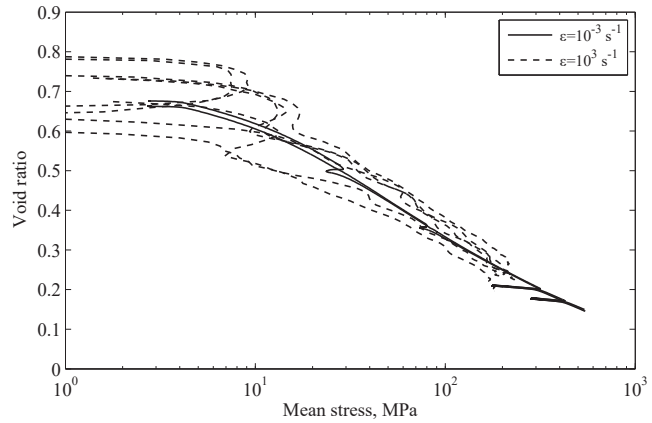


**(b)**

**Figure 3.28:** Quasi-static and high-strain-rate one-dimensional compression tests on dry medium sand in a) mean stress – dry density, b) void ratio – mean stress.

The presence of a distribution of radial stress over the specimen cross-section introduces two important considerations to the interpretation of the results:

- The radial stress measured on the surface of the confining ring will only provide the stress on the surface of the specimen, and will not be representative of the stress state inside.
- The axial stress over the specimen cross-section will vary with the level of radial confinement, but only one measurement is taken on the surface of each pressure bar. This cross-sectional variation in stress decreases as the stress pulse propagates in the bar, disappearing after a length of approximately 10 bar diameters (Follansbee and Frantz 1983). The measurement on the surface of the bar then represents the mean stress across the cross-section.

The result of these issues is that the data provided by the SHPB experiment cannot provide direct information on the material behaviour, but rather the behaviour of a sand specimen of a particular geometry.

More detailed analyses would require stress–strain data to be recorded from inside the sand specimen, which would be difficult to achieve with pressure gauges and similar techniques, as these would interact with the sand matrix and affect the results. Alternatives to physical gauges include the use of x-ray methods, which can assess the density field inside the specimen over a certain exposure time, and numerical modelling, which can be validated against physical experiments and then used for further analysis. The latter of these methods will be the focus of Chapter 6 in this thesis.

### 3.6.3 Effect of moisture content in medium sand

The response of medium sand to changes in moisture content is shown in Figures 3.29 and 3.30 for both quasi-static and high-strain-rate loading regimes. The relatively low moisture contents used in the sand specimens meant that the initial saturations were also low (see Table 3.5), so none of the specimens tested in the SHPB became fully saturated during testing and the rapid stiffening response associated with loading of the pore water (eg. Felice et al. 1987, Luo et al. 2014) was not observed.

At a moisture content of 5.0% the sand specimens are expected to become fully saturated at a dry density of $2.35\,\mathrm{Mg\,m^{-3}}$: as the mac$^{2\mathrm{T}}$ tests achieved dry densities of approximately $2.40\,\mathrm{Mg\,m^{-3}}$, these specimens will have reached full saturation towards the end of the test. The mac$^{2\mathrm{T}}$ tests were carried out in drained

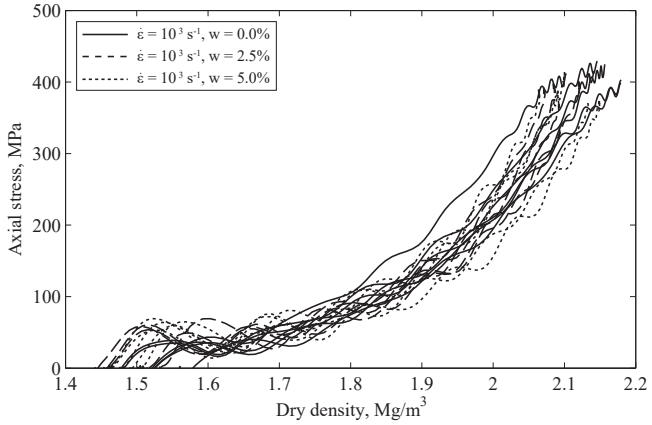


**(a)**

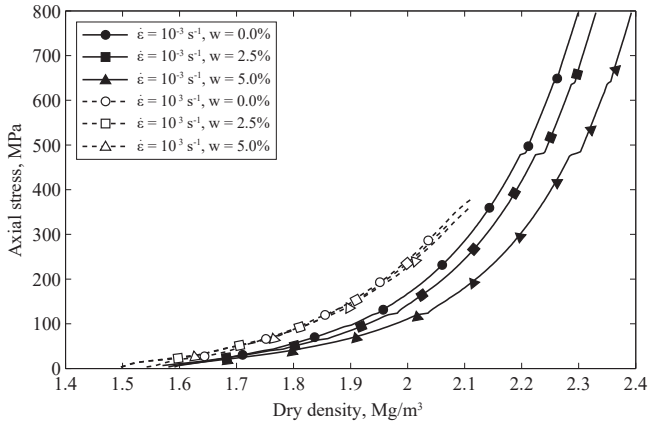


**(b)**

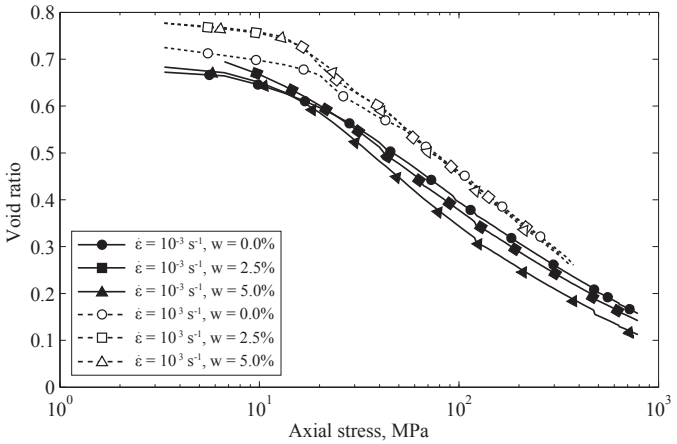


**(c)**

**Figure 3.29:** Effect of moisture content and strain rate on medium sand considering axial stresses only: a) individual SHPB tests, b) mean response in terms of dry density, c) mean response in terms of void ratio.

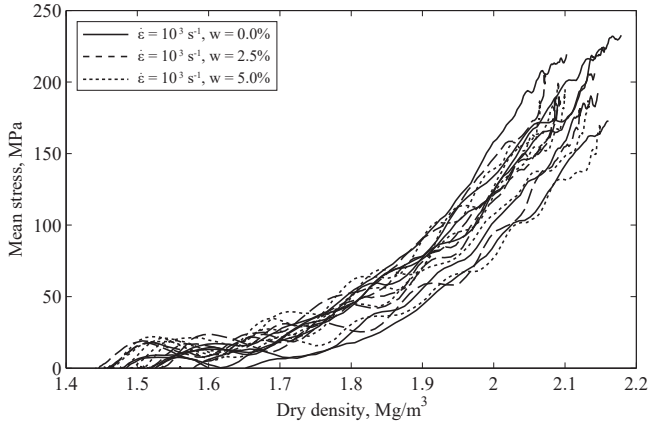


**(a)**

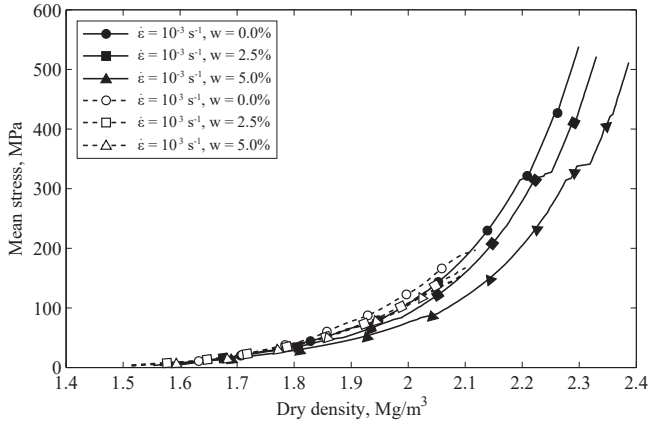


**(b)**

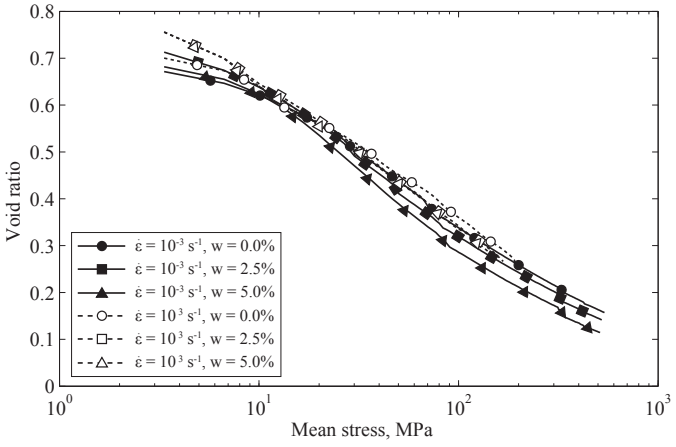


**(c)**

**Figure 3.30:** Effect of moisture content and strain rate on medium sand considering mean stresses: a) individual SHPB tests, b) mean response in terms of dry density, c) mean response in terms of void ratio.

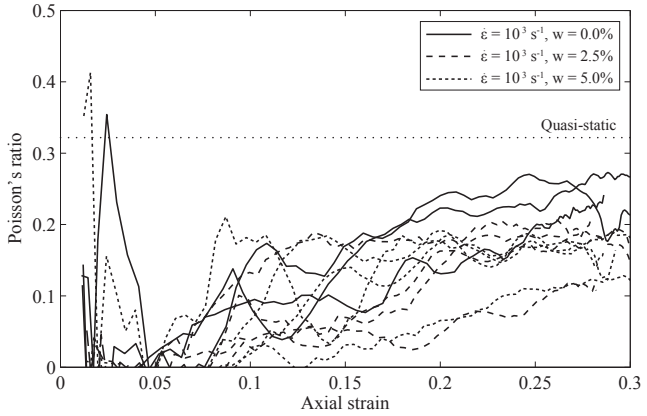


**Figure 3.31:** Apparent Poisson's ratio of medium sand specimens with varying moisture content. Only tests with reliable radial stress measurements are shown (4 out of 5 tests at both 2.5% and 5.0% moisture content).

| $w$(%) | Saturation ratio, $S_r$ (%) | | |
|---|---|---|---|
| | At initial dry density | At peak SHPB dry density | At peak mac$^{2T}$ dry density |
| 2.5 | 8.6 | 28.0 | 61.4 |
| 5.0 | 17.1 | 56.1 | 122.8 |

**Table 3.5:** Theoretical saturation ratios at the initial dry density and the peak dry densities achieved in the SHPB and mac$^{2T}$ tests, varying with moisture content.

conditions, and so the excess water was simply expelled from the sample rather than sustaining additional load. Droplets of water observed on the test box platens after the test confirm this.

In the quasi-static tests the addition of water leads to a reduction in the stiffness of the sand specimen, with the 2.5% moisture content specimens behaving less stiffly than the dry specimens, and the 5.0% moisture content specimens less stiff than the 2.5% moisture content specimens (Figures 3.29b,c and 3.30b,c). As reported by Martin et al. (2009), this reduction in stiffness is likely due to the lubricating effect of the water between the sand particles, which reduces inter-particle friction and facilitates compaction.

In contrast, the dynamic SHPB tests show no significant change in stiffness with changing moisture content: while the mean results in Figures 3.29b,c and 3.30b,c appear to show a small decrease in stiffness with increasing moisture content, the individual tests overlap each other significantly, as shown in Fig-

ures 3.29a and 3.30a. This is similar to the pre-saturation behaviour observed in high-strain-rate testing by Veyera (1994) and Luo et al. (2014). The radial response of the wet specimens is also similar to the dry tests (Figure 3.31), indicating that inertial effects continue to influence the material response. Combined with the quasi-static response, the insensitivity to moisture content at high strain rates means that a strain rate effect on stiffness appears to increase as the moisture content increases, even when mean stresses are considered.

If it is assumed that the main effect of moisture in the quasi-static tests is in aiding particle rearrangement by rolling and sliding, the moisture-insensitive behaviour observed in the dynamic tests could indicate that the compression of the sand at higher strain rates is dominated more by particle crushing than by particle rearrangement. This would contradict previous work, however, as Farr (1986) observed that sandy materials exhibited less particle breakage at higher strain rates. An alternative explanation could be that at the higher strain rate the moisture does assist in the rearrangement of particles as in the quasi-static tests, but that another mechanism, such as localised loading of pore water, increases the stiffness of the specimen, resulting in little net change in stiffness. The associated increase in pore water pressure would also decrease the effective stress on the particles, which would decrease the probability of particle fracture in line with Farr's observations.

Further tests are required to indicate whether the observed trend continues as the moisture content is increased beyond 5%. Recovery of the specimens would also allow the level of particle breakage in medium sand to be assessed with changing moisture content, which would aid the understanding of the underlying mechanism. This is the focus of Chapter 5 of this thesis.

## 3.7 Summary

This chapter introduced quasi-static and high-strain-rate one-dimensional compression tests on three sandy soils. Quasi-static tests were performed to 800 MPa using the mac$^{2T}$ rig with a soil testing box, while high-strain-rate tests were carried out to 400 MPa using a split-Hopkinson pressure bar with a steel confining ring. In both test series lateral stresses and strains were recorded.

When tested quasi-statically, the well-graded sandy loam behaved less stiffly than the more uniform medium and coarse sands, although the coarse sand had a higher initial compression index. The compression behaviour of each soil was described by a bi-linear NCL, with an intersection at a void ratio of approx-

imately 0.3 in each case. The lower compression indices at high stresses appear to be related to the increasing coordination number of the soils as observed by Hagerty et al. (1993), though this has not been investigated in detail. The unloading bulk modulus of the soils also increased as the peak stress increased.

The relative stiffness of the soils followed a similar trend in the high-strain-rate tests, except for the dominance of inertial effects at low stresses. In each soil the specimens behaved more stiffly at $10^3\,s^{-1}$ than at $10^{-3}\,s^{-1}$ when axial stresses were considered, but this apparent strain rate effect disappeared in the medium sand when mean stresses were considered: while axial stresses had increased, radial stresses had decreased. This change in stress distribution was attributed to radial inertial confinement in the specimen at high strain rates. Reliable radial stress measurements were not achieved for the sandy loam and coarse sand, due to electromagnetic interference.

The medium sand was also tested at moisture contents of 2.5% and 5.0%. Under quasi-static loading, the stiffness of the sand reduced as the moisture content increased, which was attributed to the lubricating effect of the water during particle rearrangement. Under high-strain-rate loading there was no significant change in the behaviour of the sand with changing moisture content, and it was suggested that localised loading of pore water may have offset the lubricating effects. The difference in quasi-static and high-strain-rate behaviour resulted in an increasing strain rate effect on stiffness with increasing moisture content, even when considering mean stresses.

Several experimental modifications were identified which would improve the understanding of the preceding results, namely measurement of magnetic activity in the SHPB tests, recovery of the specimens for particle size analysis and extension of the test series to higher moisture contents. Numerical modelling was also highlighted as a potential tool for understanding the stress distribution inside the SHPB specimens.

Chapter 4

# Dispersion and electromagnetic effects on SHPB measurements

## 4.1 Introduction

This chapter discusses sources of error in the analysis of SHPB experiments which were highlighted in Chapter 3. The effects of dispersion on measurements of axial stress and strain are analysed, and a first-mode correction is implemented in MATLAB, which is shown to improve the interpretation of specimen stresses. The variation in radial stress measurements is also investigated by recording the electromagnetic activity around the confining ring during experiments with air, rubber and sand specimens.

## 4.2 Dispersion correction in SHPB experiments

The results of the SHPB experiments in Chapter 3 highlighted the need for correction of the dispersive effects observed in the axial strain gauge signals. As introduced in §2.3.3, strain readings from the surface of a pressure bar are affected by three errors:

- dispersion of the signal due to variation of phase velocity with frequency, which affects the phase angle of frequency components;
- variation in the response across the bar cross-section due to radial inertia effects, which affects the amplitude of frequency components; and
- variation in the ratio of axial stress to axial strain both across the bar cross-section and with frequency, which also affects the amplitude of frequency components.

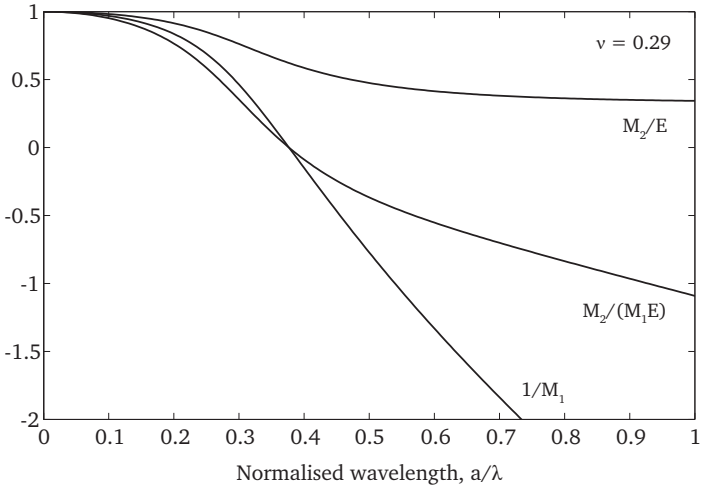


**Figure 4.1:** Variation of factors $M_1$ and $M_2$ in a cylindical bar for $\nu = 0.29$.

These errors become significant at higher frequencies ($a/\lambda > 0.05$), but can be corrected using the method described by Tyas and Pope (2005), where corrections are applied to the amplitudes and phase angles of each frequency component in the signal.

### 4.2.1 Phase angle correction

The first correction to be made to the SHPB signals is adjustment of the phase angle to account for the dispersion of each frequency component over the distance between the strain gauge and the bar end. As described by Gorham (1983) and Follansbee and Frantz (1983), this is achieved by calculating the phase velocity, $c_\omega$, of each component using Bancroft's equation (Equation 2.17), and then applying a phase shift, $\theta'_\omega$:

$$\theta'_\omega = \left(\frac{c_0}{c_\omega} - 1\right)\frac{\omega z}{c_0} \tag{4.1}$$

where $\omega$ is the angular frequency of the component, and $z$ is the distance the correction is applied over, positive in the direction of wave propagation. In this work it will be assumed that waves propagate in the first mode only: while Bancroft's equation shows that higher modes will propagate at normalised frequencies above $fa/c_0 \approx 0.23$ (92 kHz in the current setup), it is not currently known how energy is distributed when several modes are propagating concurrently.

### 4.2.2 Amplitude correction

The second correction to the SHPB signals applies factors to the amplitude of the frequency components. Tyas and Watson (2001) introduced the factors $M_1$ and $M_2$ to account for the radial variation of strain and Young's modulus, respectively, deriving these from Davies' (1948) analysis of these radial effects. Using these factors, the strain measurement recorded on the surface of the bar can be used to infer the mean axial stress and strain acting over the whole cross-section. The factors are defined as

$$M_1 = \frac{2\left(1+\frac{1-\beta x}{x-1}\right)}{\varphi(ha)+\frac{1-\beta x}{x-1}\,\varphi(\kappa a)} \tag{4.2}$$

$$M_2 = E\left(\frac{c_\omega}{c_0}\right)^2 \tag{4.3}$$

where

$$\begin{aligned} \beta &= (1-2\nu)/(1-\nu) \\ x &= (c_\omega/c_0)^2(1+\nu) \\ h &= \gamma(\beta x-1)^{\frac{1}{2}} \\ \kappa &= \gamma(2x-1)^{\frac{1}{2}} \\ \varphi(y) &= yJ_0(y)/J_1(y) \end{aligned}$$

| | | |
|---|---|---|
| $c_\omega$ | — | Phase velocity |
| $c_0$ | — | One-dimensional elastic wave velocity |
| $a$ | — | Bar radius |
| $\nu$ | — | Poisson's ratio |
| $E$ | — | Young's modulus |
| $\gamma$ | — | Wave number, $2\pi/\lambda$ |
| $\lambda$ | — | Wavelength |
| $J_n(y)$ | — | Bessel function of the first kind, of order $n$ |

The variation of $M_1$ and $M_2$ with normalised wavelength is shown in Figure 4.1. The reciprocal of $M_1$ is plotted due to the discontinuity in $M_1$ at $a/\lambda = 0.375$, which corresponds to the point where the strain recorded on the surface of the bar falls to zero; at even higher frequencies the recorded strain has the opposite sign to the mean cross-sectional response. As the corrections applied around $a/\lambda = 0.375$ involve multiplying a low-magnitude signal by a very large correction factor, the noise in the signal is likely to significantly reduce the accuracy of

the result. This forms an effective upper limit on the frequency range which can be corrected: Tyas and Watson (2001) suggest that the method can be reliably used to $a/\lambda \approx 0.3$, which is equivalent to 94 kHz in the current tests.

## 4.3 A MATLAB function for dispersion correction

A MATLAB function (`dispersion.m`) has been developed to automate the application of phase angle and amplitude corrections to SHPB signals as part of the processing described in §2.3.1. This replaces the simple timeshifting of signals with manipulation of individual frequency components, the functionality and limitations of which are described below. The full source for `dispersion.m` has been reproduced in Appendix A.

### 4.3.1 The frequency domain in MATLAB

Conversion of a signal into the frequency domain is achieved using the fast Fourier transform (FFT), an algorithm which represents a signal as the sum of a series of sinusoidal waves of different frequencies and amplitudes. Implementation of the FFT in MATLAB is achieved using the `fft` function, which takes any regularly-sampled signal and provides amplitude and phase information with frequency as a matrix of complex vectors of the form $z = z_r + iz_i$. The amplitude, $A$, and phase angle, $\theta$, of the Fourier component at a particular frequency can be calculated as

$$A = \sqrt{z_r^2 + z_i^2} \tag{4.4}$$

$$\theta = \tan^{-1}\left(\frac{z_i}{z_r}\right) \tag{4.5}$$

These relationships are shown in Figure 4.2a, where $z$ and its complex conjugate $\bar{z}$ are represented in the complex plane, while Figure 4.2b shows how these values are used to represent the amplitude and phase angle of a particular sinusoid. After suitable corrections have been applied to the amplitude and phase angle, the Fourier component can be reconstructed using the relationship

$$z = A\cos(\theta) + iA\sin(\theta) = Ae^{i\theta} \tag{4.6}$$

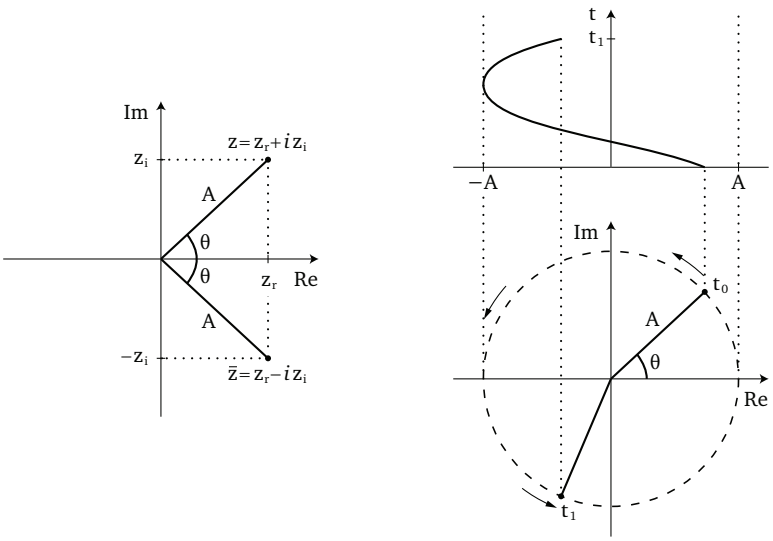


**(a)** **(b)**

**Figure 4.2:** A Fourier component $z$ in the complex plane: a) relationship to amplitude and phase angle, b) description of a sinusoid.

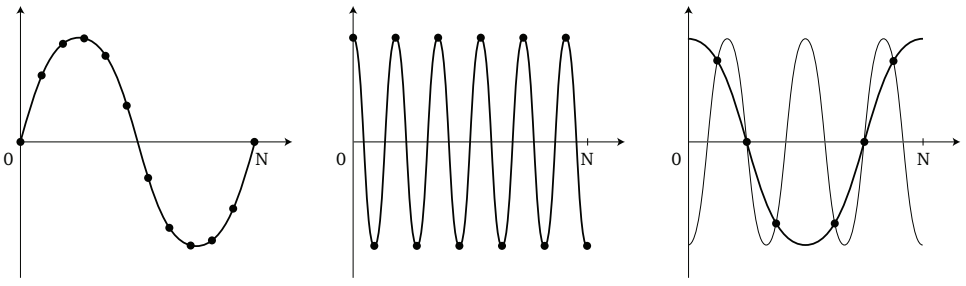


**(a)** **(b)** **(c)**

**Figure 4.3:** Frequency limitations in the FFT: a) minimum frequency and b) maximum frequency for a signal where $N = 12$; c) aliasing at higher frequencies.

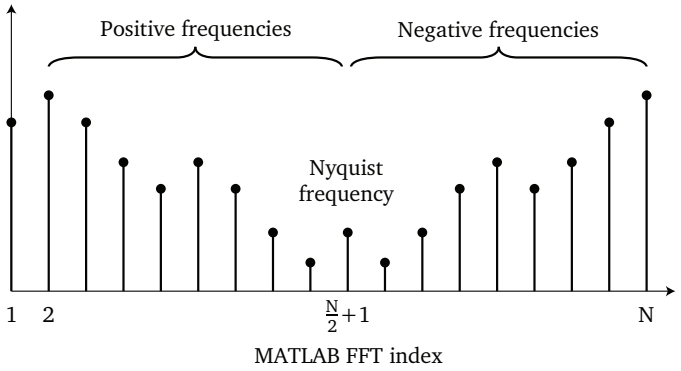


**Figure 4.4:** Composition of the frequency-domain vector produced by `fft`.

### 4.3.2 Correction bandwidth

The FFT is a discrete form of the Fourier transform, and so components are only calculated at discrete frequency values, which depend on the sampling rate and length of the original signal. If a signal is sampled $N$ times at a frequency $f$ the lowest readable frequency is equal to $f/N$, which describes a single wave filling the sampling window (Figure 4.3a). Higher frequencies are multiples of this fundamental frequency, up to the highest readable frequency, or Nyquist frequency, which is equal to $f/2$ (Figure 4.3b). This limit is imposed because at least two samples are required for each period to prevent aliasing, an example of which is shown in Figure 4.3c. Here two different sinusoids can be fitted to the sample data due to undersampling. The maximum readable frequency is restricted by the sampling rate of the oscilloscope ($f/2 = 390\,\text{kHz}$ in the current tests), although the frequency resolution can be improved by increasing $N$, either by increasing the recording time, or by zero-padding the input signal.

Given an $N$-length time-domain vector $x(t)$, the `fft` function will produce an $N$-length frequency domain vector $X(\omega)$. As a result of the aliasing described above, the second half of $X(\omega)$ is the complex conjugate of the first half, reflected about the Nyquist frequency, as shown in Figure 4.4. Practically, this means that corrections only need to be individually applied to the first $N/2+1$ bins in $X(\omega)$, which can then be reflected to complete the vector.

As discussed in §4.2.2, an additional frequency limit is imposed by the very low strain signals measured on the surface of the bar at frequencies above 94 kHz, so that in the current SHPB setup corrections can only be reliably applied between 39 µHz and 94 kHz. This is shown in Figure 4.5, which is a frequency-domain representation of a typical experimental incident pulse in the form of a modified periodogram. Power is expressed in logarithmic units, where a change of 10 dB

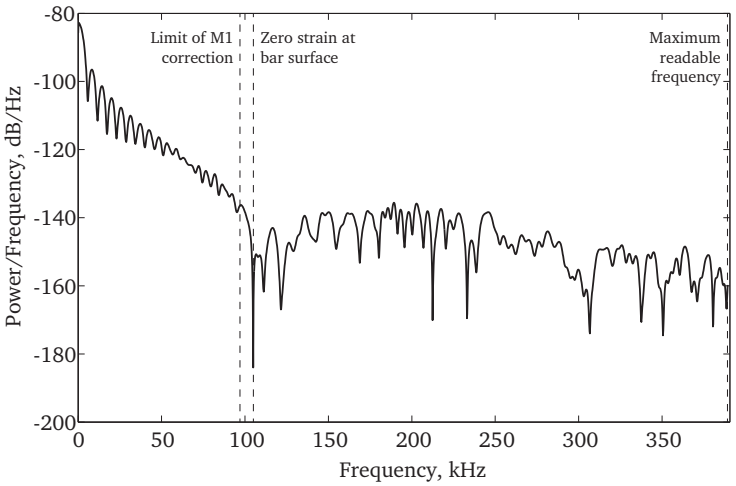


**Figure 4.5:** Power spectral density for experimental incident wave, and maximum frequency limits imposed by the strain gauge data and FFT.

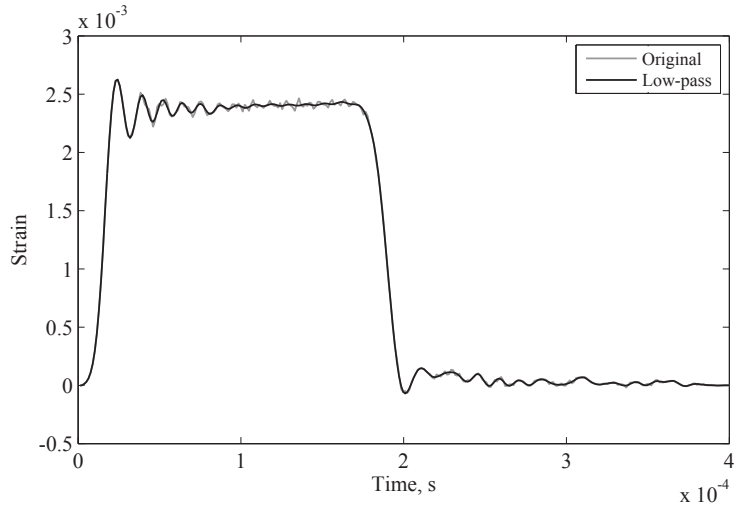


**Figure 4.6:** Experimental incident wave and result of ideal low-pass filtering of frequencies above 94 kHz.

| *Inputs* | |
|---|---|
| `x` | zero-padded strain signal in time domain |
| `fs` | sampling frequency [Hz] |
| `a` | bar radius [m] |
| `c0` | one-dimensional wave velocity of the bar [$\mathrm{m\,s^{-1}}$] |
| `E` | Young's modulus of the bar [GPa] |
| `z` | distance to correct over, +ve in direction of propagation [m] |

| *Outputs* | |
|---|---|
| `xStrain` | dispersion-corrected strain signal |
| `xStress` | dispersion-corrected stress signal [MPa] |

**Table 4.1:** Input and output variables used in `dispersion.m`.

denotes an order of magnitude change in the power of the signal. As described above, the periodogram shows that the power of the signal recorded on the surface of the bar rapidly reduces to zero between 94 kHz and 110 kHz. As dispersion correction can only be applied at frequencies below 94 kHz, a low-pass filter is applied to the signal to remove the higher frequencies. The power at these higher frequencies is orders of magnitude lower, and so little information is lost in filtering, as shown in Figure 4.6.

### 4.3.3 Operation of `dispersion.m`

The `dispersion()` function is called as a subroutine during processing of the SHPB signals using `shpb()`, both of which are provided in Appendix A. Once the incident, reflected and transmitted waves have been isolated, `dispersion()` is used to infer the stress and strain at the bar–specimen interface for each wave using a form of the following command, which contains input and output variables as defined in Table 4.1.

```
[xStrain xStress] = dispersion(x,fs,a,c0,E,z);
```

The operation of the function can be summarised as follows:

a) The strain signal is converted to a frequency-domain signal using the FFT.

b) An ideal low-pass filter is used to remove frequency components above the $M_1$ correction cut-off.

c) For each of the remaining components below the Nyquist frequency:

(i) The required phase shift and the factors $M_1$ and $M_2$ are found using the `dispersionFactors.m` subroutine. This function uses a pre-calculated, normalised look-up table to improve calculation time.

(ii) A dispersion-corrected strain component is reconstructed using Equation 4.6, factor $M_1$ and the phase angle correction, $\theta'_\omega$:

$$z_\varepsilon = M_1 A e^{i(\theta - \theta'_\omega)} \tag{4.7}$$

where $A$ is the original amplitude of the component and $\theta$ is the original phase angle.

(iii) Similarly, a dispersion-corrected stress component is reconstructed using factors $M_1$ and $M_2$ and the phase angle correction, $\theta'_\omega$:

$$z_\sigma = M_1 M_2 A e^{i(\theta - \theta'_\omega)} \tag{4.8}$$

d) The frequency components above the Nyquist frequency are created by taking the complex conjugate of these corrected stress and strain components.

e) The frequency-domain stress and strain signals are converted back to the time domain using the inverse FFT, `ifft()`, and returned as output variables `xStrain` and `xStress`.

These corrected pressure bar stresses and strains are then used to infer the behaviour of the SHPB specimen as described in §2.3.1.

### 4.3.4 Comparison with one-dimensional wave theory

To illustrate the benefit of dispersion correction using `dispersion()`, Figures 4.7 and 4.8 show the front and back specimen stresses in a SHPB test on dry sand, calculated using one-dimensional wave theory and the frequency-domain method described above. In Figure 4.7a the incident and reflected stress waves measured at the incident bar strain gauge are assumed to maintain their shape as they are translated along the time axis, while in Figure 4.7b the dispersion associated with 1000 mm of travel in the bar is added to the incident wave and removed from the reflected wave.

The dispersion correction causes a significant reduction in the large fluctuations of front stress calculated using one-dimensional wave theory, as shown in Figure 4.7c. This is due to alterations to the initial gradient of the stress waves, and the position and magnitude of the Pochhammer–Chree oscillations, which

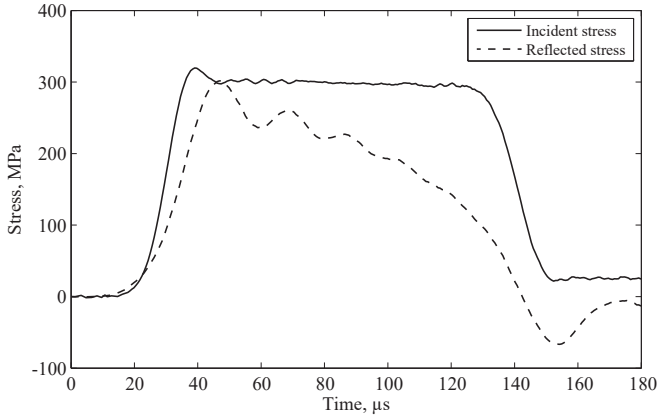


**(a)**

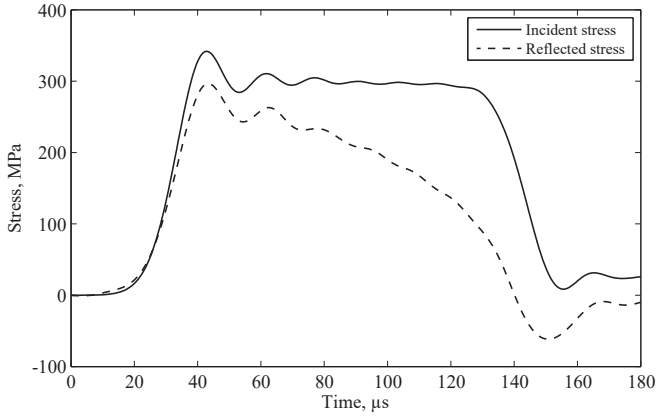


**(b)**

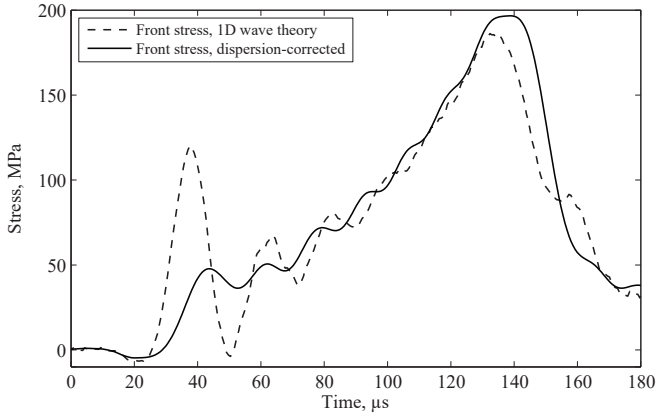


**(c)**

**Figure 4.7:** Comparison of incident and reflected waves using a) one-dimensional wave theory and b) dispersion-corrected analysis, and c) the specimen front stress calculated using each method. Reflected waves have been inverted to aid comparison.

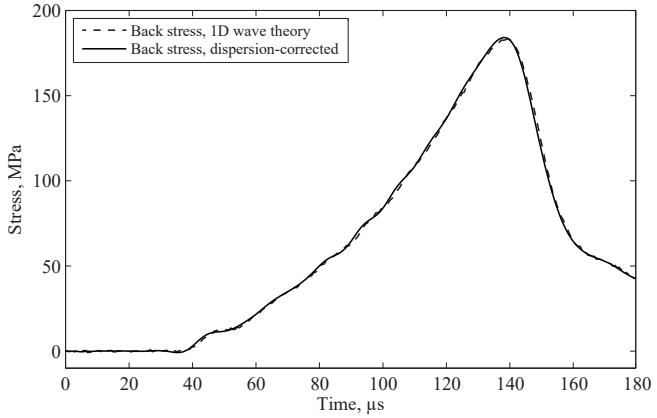


**Figure 4.8:** Comparison of specimen back stress calculated using one-dimensional wave theory and dispersion-corrected analysis.

improves the alignment of these features in the incident and reflected waves. In contrast, the dispersion correction has little effect on the calculated back stress in Figure 4.8, as the transmitted wave contains few high-frequency features and is measured only 250 mm from the specimen interface. This improved processing technique has been applied to all SHPB experiments in this thesis, enabling a representative axial stress to be calculated from the mean of the front and back specimen stresses.

### 4.3.5 Stress equilibrium

The ability to calculate representative front stresses also enables a meaningful assessment of the variation of axial stress in the SHPB specimens, which can provide information about inertial effects. Figures 4.9 and 4.10 show the front and back specimen stresses for typical experiments on dry medium sand in Chapters 3 and 5: in both cases, the front stress is considerably higher than the back stress for the first 80 µs. This initial lack of stress equilibrium indicates the level of axial inertia acting in the specimen as it begins to compact, and explains the increased stiffness observed at low stresses in the results in Chapters 3 and 5. The difference in front and back stress is similar for both experimental setups, with an initial peak of around 100 MPa. The strain rate at this point is approximately 5200 $s^{-1}$ in the Chapter 3 experiments and 3000 $s^{-1}$ in the Chapter 5 experiments, and so the axial inertia does not seem to be strongly affected by the change in strain rate during this part of the loading.

After 80 μs the front and back stress equalise, and the normalised stress differences in Figures 4.9 and 4.10 tend towards zero, corresponding well with the release of the inertial effects as discussed in Chapter 3. The experiment in Figure 4.9 does not fully achieve stress equilibrium until near the peak stress, where the loading is maintained and accelerations in the specimen are relatively low (*c.f.* Figure 3.17). The experiment in Figure 4.10 achieves stress equilibrium while the axial stress is still rising, and so this part of the loading appears to be more sensitive to variations in strain rate history.

The stress equilibrium in these experiments highlights the difficulty in designing valid SHPB experiments for soils. At the strain rates and stresses of interest large inertial contributions are present for at least part of the experiment, but these cannot be simply eliminated by further reducing the specimen length as in other materials, as the specimen would no longer be representative of the soil.

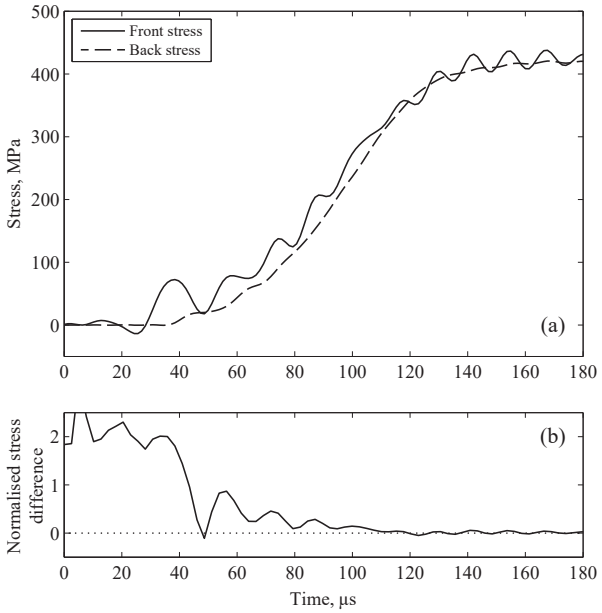


**Figure 4.9:** a) Front and back specimen stresses, and b) the difference between them normalised by their mean, for a typical experiment using the SHPB in Chapter 3.

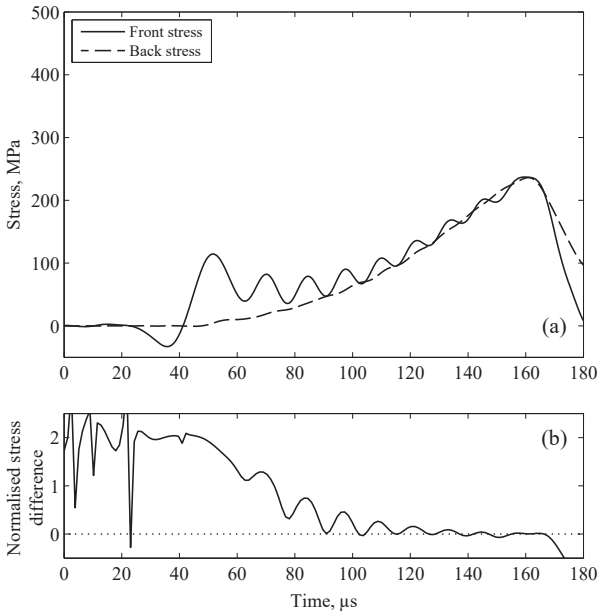


**Figure 4.10:** a) Front and back specimen stresses, and b) the difference between them normalised by their mean, for a typical experiment using the SHPB in Chapter 5.

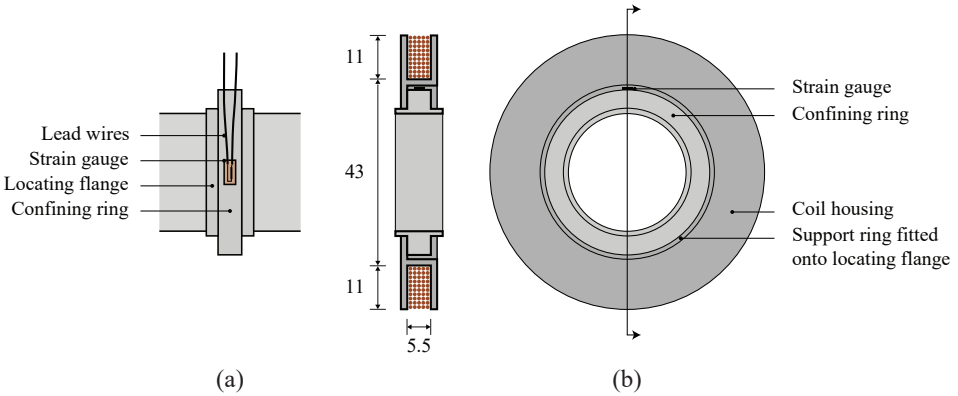


**Figure 4.11:** Arrangement of a) gauged confining ring during a SHPB experiment (plan), b) a 200-turn induction coil fitted to a confining ring (section and side view).

## 4.4 Measurement of electromagnetic activity

It was noted in Chapter 3 that measurements of radial stress in the SHPB tests appeared to be affected by electromagnetic activity, leading to spurious peaks and troughs, and potentially affecting the magnitude of the signal over the whole loading duration. In order to identify any sources of electromagnetic activity, and to understand how this may affect the radial stress measurements, an induction coil was designed to fit around the confining ring of the SHPB apparatus used in Chapter 3, as shown in Figure 4.11.

The coil consists of 200 turns of 0.5 mm diameter single-core copper magnet wire arranged in ten-turn rows. This is secured using a polystyrene housing which is attached by interference fit to one of the confining ring flanges. A 2 mm clearance between the coil housing and the main body of the confining ring ensures that the coil is not strained during testing, so that any measurements can be confidently attributed to an electromagnetic source.

Any electromagnetic activity will generate an electromotive force (EMF) in the coil according to Faraday's law of induction

$$\mathscr{E} = -N\frac{\mathrm{d}\Phi_B}{\mathrm{d}t} \tag{4.9}$$

where $\mathscr{E}$ is the EMF, $N$ is the number of turns in the coil and $\Phi_B$ is the magnetic flux (Feynman et al. 1964). The magnetic flux in the coil is the product of the external magnetic field, $B$, and the area of the coil perpendicular to the field, $A$, so that this can be rewritten as

$$\mathscr{E} = -N\frac{\mathrm{d}(BA)}{\mathrm{d}t} \tag{4.10}$$

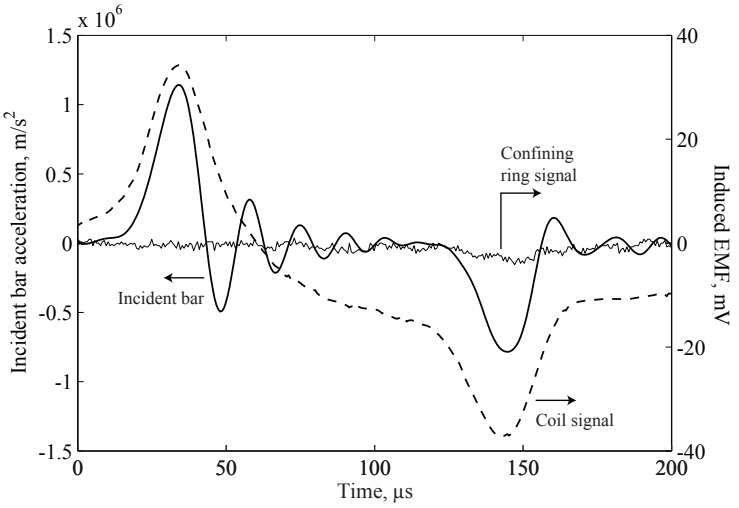


**Figure 4.12:** Relationship between incident bar acceleration and induction coil signal in a SHPB test with a 5 mm air specimen. Acceleration positive when towards the coil.

### 4.4.1 EMF contribution from pressure bars

To isolate the potential contributions of the specimen and pressure bars, experiments using the confining ring and induction coil were carried out with only a 5 mm air gap between the pressure bars. An EMF was induced in the coil as shown in Figure 4.12, and appears to be associated with the acceleration of the incident bar: the transmitter bar remains stationary over the period of interest due to the air gap. If a constant magnetic field existed around the incident bar the EMF in the coil would be expected to be proportional to the bar velocity: the correlation with acceleration implies that the strength of the magnetic field is also changing. Such a variation of the magnetic field with velocity (which is proportional to the stress in the bar) resembles the Villari effect discussed in §3.6.2, suggesting that the transient stresses in the bar lead to its magnetisation.

While an EMF was repeatedly produced in the induction coil, only one of the three experiments exhibited an EMF in the confining ring signal, and even in this case the EMF only significantly exceeded the signal noise during the deceleration at the end of the incident wave (Figure 4.12).

As described by Equation 4.10, EMFs are generated by changes in the magnetic field which passes through the area enclosed by the coil or wire loop, which in the case of the coil is in a well-defined plane parallel to the bar cross-section, as shown in Figure 4.13a. The loop formed by the gauge leadwires, however, is nominally parallel to the bar surface, and varies in position from test to test due

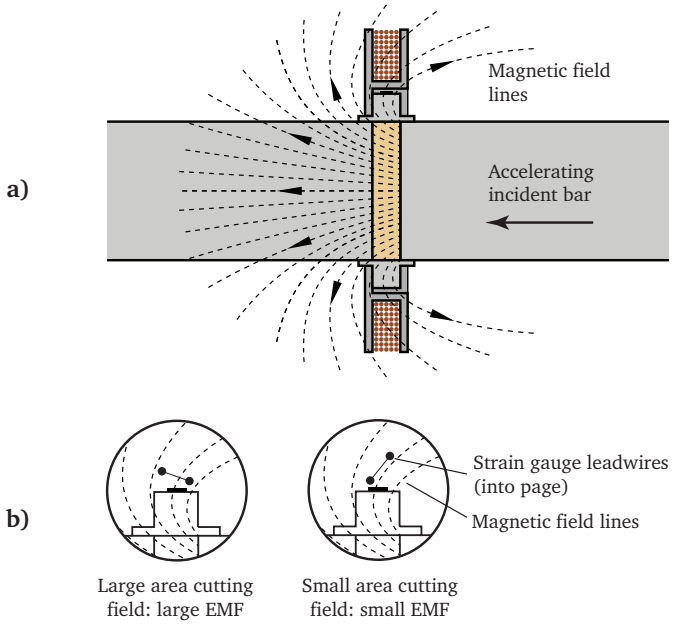


**Figure 4.13:** An example of the field around a magnetised incident bar in relation to a) the induction coil, and b) the leadwires on the confining ring strain gauge.

to the thin, flexible wire. The area of the loop perpendicular to the magnetic field therefore varies considerably depending on the relative position of the two leadwires in any particular experiment, as demonstrated in Figure 4.13b. Where a large area cuts the field a larger EMF will be generated, and where a small area cuts the field a smaller EMF will be generated. This is likely to be the cause of the large variation in the EMFs observed in these experiments, as well as those reported in Chapter 3.

### 4.4.2 EMF contribution from particle breakage

Section 3.6.2 discussed the possibility that fracture of the sand particles may be another source of electromagnetic activity, and so experiments on dry medium sand and natural rubber were also carried out using the induction coil. In both cases the induction coil signals were similar to those in Figure 4.12, and a number of experiments showed EMF interference in the radial strain measurements. This is shown in Figures 4.14 and 4.15 for sand and rubber, respectively, where the the more obvious additional peaks (▲) and troughs (▼) are highlighted. The peaks at the beginning of the pulses coincide with the peak velocity in the incident bar and so appear to be another artefact of the pressure bar magnetism. The trough at higher radial stress in Figure 4.14 for sand also occurs at in Fig-

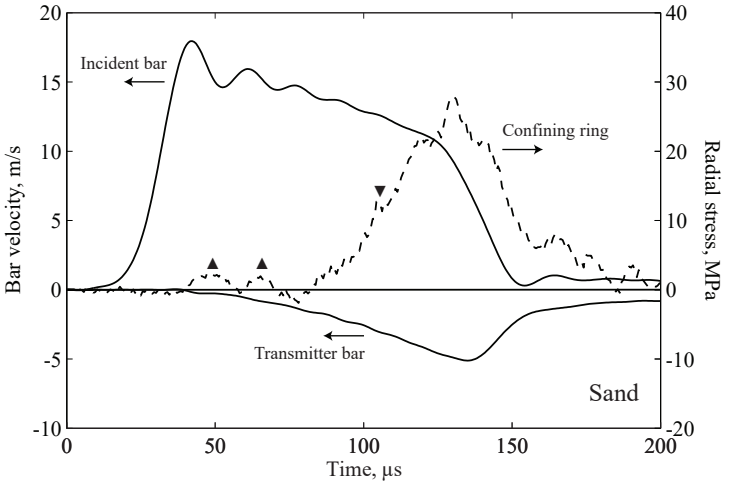


**Figure 4.14:** Relationship between incident and transmitter bar velocity and radial stress measurement in a SHPB test on a 5 mm sand specimen. Velocity positive when towards the coil. Peaks and troughs due to induced voltages are marked with ▲ and ▼.

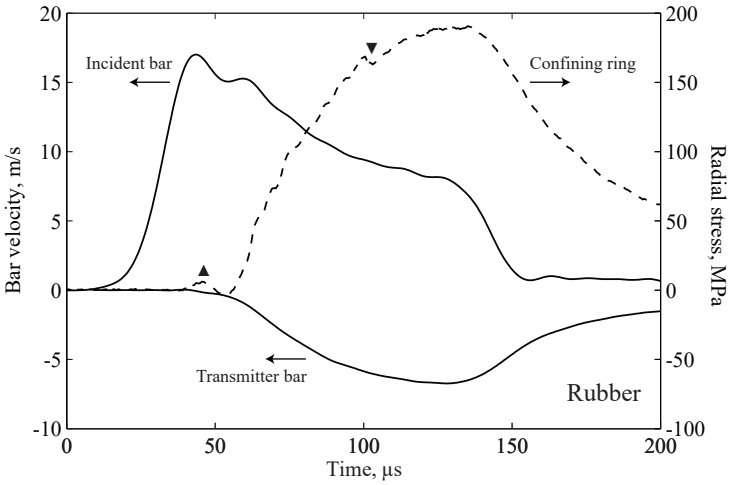


**Figure 4.15:** Relationship between incident and transmitter bar velocity and radial stress measurement in a SHPB test on a 5 mm rubber specimen. Velocity positive when towards the coil. Peaks and troughs due to induced voltages are marked with ▲ and ▼.

ure 4.15 for rubber, and so while it has no obvious relation to the movement of the pressure bars, it cannot be due to particle breakage.

It should be noted that the expected contribution in this case was from an electrical, rather than magnetic, source. It is quite possible that the phenomenon occurs, but that the arrangement of the steel pressure bars and confining ring form a Faraday cage around the specimen, shielding the strain gauge circuit from the noise which is produced. The conclusion is therefore only that particle breakage does not significantly contribute to the noise in the radial stress measurements: further experiments without a confining ring would be required to identify whether significant electrical activity is generated by particle breakage.

## 4.5 Summary

This chapter discussed sources of error in the processing of axial and radial stress and strain measurements in SHPB experiments. The frequency-domain dispersion correction method described by Tyas and Pope (2005) was used to develop a MATLAB function to improve the accuracy of axial stresses inferred at the bar ends. This was particularly shown to improve the stress calculated at the front face of the specimen, which is calculated by the superposition of the incident and reflected stress waves, enabling a representative mean axial stress to be used to describe the specimen behaviour.

Experiments with an induction coil confirmed that the pressure bars are the major source of electromagnetic noise in measurements of radial stress in SHPB experiments. The EMF generated in the strain gauge circuit is sensitive to the position of the leadwires, and so an automated correction of these EMFs would be difficult to apply in the current experimental configuration. The best approach in future experiments with radial strain measurements would be to use non-ferrous pressure bars to remove the Villari effect; however, if this is impractical it may be possible to consistently position a twisted pair of gauge leadwires to minimise the effect.

Chapter 5

# Recovery tests on medium sand

## 5.1 Introduction

Building on the methods and results of Chapters 3 and 4, this chapter presents a refined methodology for high-strain-rate experiments on medium sand which allows post-test particle size distributions to be recovered reliably. These experiments are carried out at moisture contents between 0% and 15%, enabling the effect of moisture content on stiffness and particle breakage to be analysed from dry specimens up to specimens which reach full saturation during loading.

## 5.2 SHPB recovery experiments

Post-test particle size analyses were identified in Chapter 3 as a potential tool for understanding the variation in soil response with strain rate and moisture content, but were not implemented as meaningful analysis of the SHPB specimens was hindered by two issues. Firstly, the peak stress was maintained for a period of between 80 μs and 100 μs before unloading, allowing time for further particle breakage to take place. Secondly, the stress waves continued to reflect up and down the SHPB after the initial loading, repeatedly loading and unloading the sand specimen. While these additional loadings should be of a lower magnitude than the first, the additional time in a loaded state could introduce similar errors to the maintained peak stress above, and any rearrangement of the sand particles between loadings could make them more susceptible to breakage. Accurate measurement of the post-test particle size distributions therefore requires modifications to the SHPB experiment to ensure that the sand specimens experience a single loading pulse with immediate unloading on reaching a peak stress.

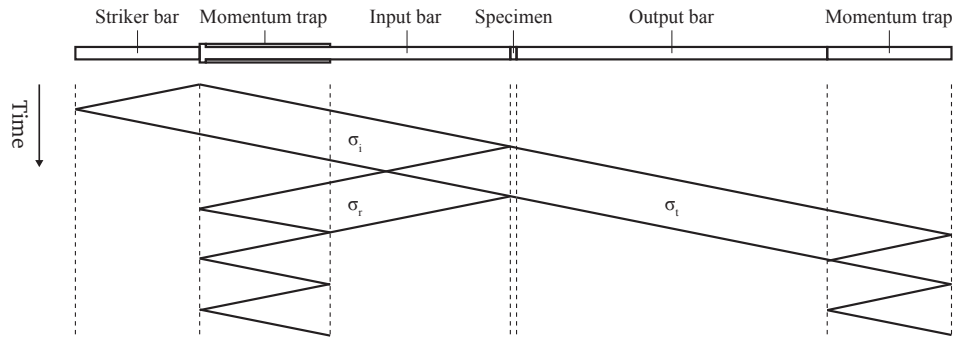


**Figure 5.1:** Lagrange diagram of a single-pulse compression SHPB test using momentum traps on the incident and transmitter bars, as developed by Nemat-Nasser et al. (1991).

### 5.2.1 Momentum-trapping techniques

Nemat-Nasser et al. (1991) developed techniques for single-pulse and stress-reversal SHPB tests which used reaction masses and momentum traps to alter the stress waves experienced by the specimen. In the example shown in Figure 5.1 the incident and transmitter bars are fitted with momentum traps of the same cross-sectional area – a tube and a bar, respectively. The tube and bar each have a length at least that of the incident wave, and prevent the reflected and transmitted waves from returning to the specimen, so that the specimen experiences a single stress pulse during the experiment.

The tensile reflected wave in the incident bar is converted into a compressive wave in the tube by an additional flange at the striker end of the incident bar. With a perfect contact and impedance match between the bar and tube, no further stress waves travel down the incident bar to the specimen: instead the entire wave is 'trapped' in the tube, where it reciprocates until it dissipates fully. Similarly, in the transmitter bar the compressive transmitted wave continues into the momentum trap and reflects as a tensile wave at its end. On returning to the interface with the transmitter bar, the tensile wave reflects again, and the two bars separate with the entire wave 'trapped' in the additional bar.

While this method ensures a single loading pulse in theory, it has several issues in practice, particularly with trapping the reflected wave. Firstly, a precision gap must be left between the incident bar flange and the momentum trapping tube, to account for the initial displacement of the bar due to the incident wave. If this gap is too large or too small, part of the reflected wave will fail to be trapped, and the specimen will experience additional loading. Secondly, the method

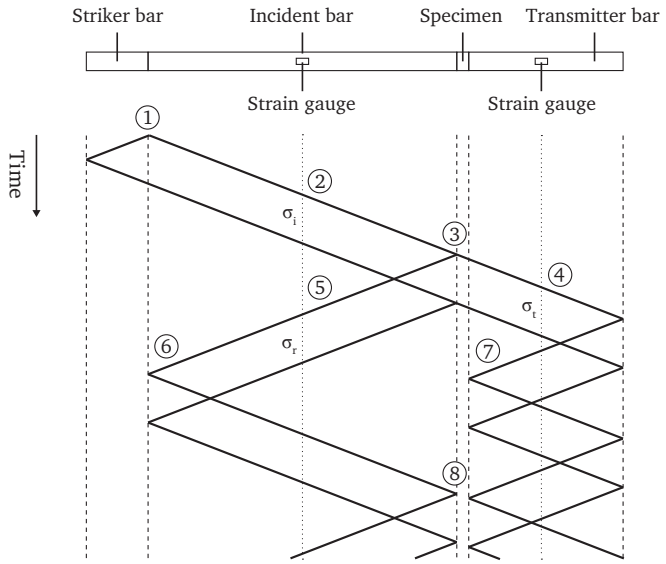


**Figure 5.2:** Lagrange diagram of a single-pulse compression SHPB test using a short transmitter bar as a momentum trap.

relies on an exact impedance match between the bar and tube to ensure the entire pulse is transferred: any damage to the flange or tube end will result in an imperfect contact which will again cause the specimen to experience a second loading.

Due to these limitations, the current work will instead adopt the approach developed by Chen and Ravichandran (1997), which is shown in Figure 5.2. In this case the transmitter bar itself is used as a momentum trap by reducing its length to half that of the incident bar. The initiation and recording of the incident, reflected and transmitted waves (Points 1–5) occur as in the previous experiments (§2.3.1). As the wave in the short transmitter bar will be reflected back towards the strain gauge, it is ensured that the distance between the strain gauge and the distal end of the bar is at least half the length of the transmitted pulse to avoid signal overlap. At around the same time that the reflected wave reaches the end of the incident bar (Point 6), the reflected transmitted wave has already returned to the specimen interface (Point 7). The specimen end of the transmitter bar begins to move, opening a space between the specimen and the transmitter bar before the arrival of the second compressive wave (Point 8), and preventing further specimen loading.

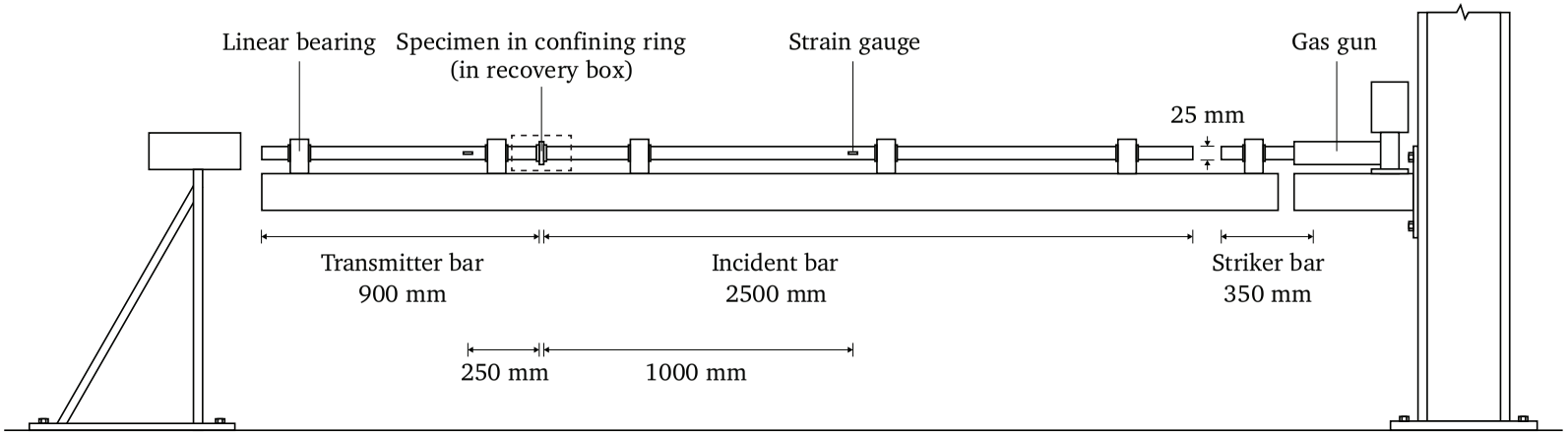


**Figure 5.3:** Schematic of recovery SHPB.

### 5.2.2 Modifications to SHPB methodology

To incorporate this recovery approach, the SHPB used in Chapter 3 was modified by altering the length of the bars, as shown in Figure 5.3. The length of the striker bar was reduced from 400 mm to 350 mm to ensure that the specimen was unloaded immediately after reaching a peak stress. This also had the effect of reducing the peak stress from 400 MPa to approximately 200 MPa, and slightly reduced the peak strain rate to 3500 $s^{-1}$ (Figure 5.4). This lower strain rate was also more stable than in the previous experiments (*cf.* Figure 3.17).

The transmitter bar was shortened from 1500 mm to 900 mm, the shortest length which prevents the transmitted wave being overwritten by the reflection from the bar end. The incident bar length was increased to 2500 mm: when using the unmodified 1500 mm incident bar, the reflected wave returns to the specimen interface before the transmitter bar begins to move, resulting in additional specimen loading. This is indicated in Figure 5.5 by the change in the shape of the transmitted wave after several reflections, where it contains an additional 50 MPa component. By increasing the length of the incident bar to 2500 mm, the transmitter bar begins to move before the reflected wave returns to the specimen, and the specimen does not experience any further loading. This is shown in Figure 5.6 by the decay of the wave reciprocating in the transmitter bar.

To ensure that the sand specimens were retained for further study, a lidded polypropylene box was fitted around the confining ring assembly (Figure 5.3). As holes were required to permit the pressure bars to enter the box, close-fitting PTFE bushings were used to prevent sand loss. This method typically retained more than 99% of the dry mass of the specimen, with only small losses from particles embedded in the aluminium foil disks. Use of the box also allowed the radial strain gauge leadwires to be held perpendicular to the confining ring, reducing the electromagnetic effects discussed in Chapter 4. The sample preparation, steel confining ring, and strain gauge instrumentation continued to be used as described in §3.5.1.

## 5.3 Test series

Specimens were prepared with moisture contents of 0.0%, 2.5%, 5.0%, 7.5%, 10.0%, 12.5% and 15.0%. Three specimens were tested at each moisture content, using a constant dry mass of 3.50 g, and with water added using the method described in §3.2.5. The initial saturations of the specimens and the dry densities required to reach full saturation are shown in Table 5.1.

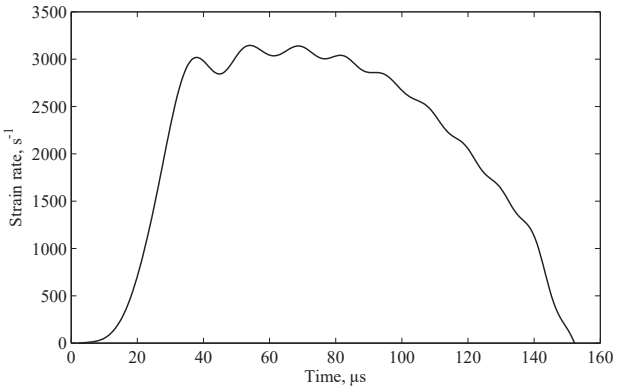


**Figure 5.4:** Typical strain rate history achieved using recovery SHPB.

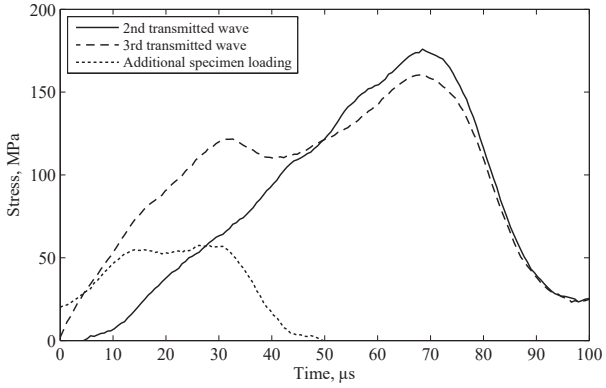


**Figure 5.5:** With a short incident bar, the specimen experiences additional loadings, indicated by the difference in subsequent transmitted waves.

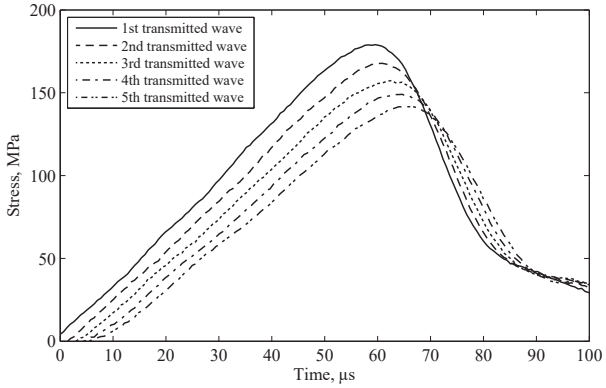


**Figure 5.6:** With a long incident bar, the specimen experiences only one loading, indicated by the steady decay of the wave reciprocating in the transmitter bar.

| Moisture content (%) | 0.0 | 2.5 | 5.0 | 7.5 | 10.0 | 12.5 | 15.0 |
|---|---|---|---|---|---|---|---|
| Saturation ratio at $\rho_d = 1.5\,\mathrm{Mg\,m^{-3}}$ (%) | 0.0 | 8.6 | 17.3 | 25.9 | 34.6 | 43.2 | 51.8 |
| Dry density at full saturation ($\mathrm{Mg\,m^{-3}}$) | — | 2.49 | 2.34 | 2.21 | 2.09 | 1.99 | 1.90 |

**Table 5.1:** Initial saturation ratios and dry density required to reach full saturation for medium sand at moisture contents between 0% and 15%.

## 5.4 Results and discussion

The axial stress – dry density behaviour of each sand specimen is shown in Figure 5.7 alongside the pre- and post-test particle size distributions (PSDs). Axial stresses were calculated using the dispersion-corrected stresses from both pressure bars, and so represent the mean axial stress in the specimen. This greatly improved the representation of axial stress in the early stages of the experiment, where inertial stresses dominate, and resulted in the highly repeatable measurements in Figure 5.7.

PSDs were analysed using a Mastersizer 3000 (§3.2.3) fitted with a wet dispersion unit, where particles are suspended in a liquid dispersant (distilled water). The wet dispersion unit was used as it enables reliable testing of small specimens, and incorporates stirring and ultrasound features which were used to separate any agglomerations which may have formed during the SHPB test.

### 5.4.1 Partially-saturated specimens

The mean axial stress – dry density behaviour in Figure 5.8a shows that for moisture contents between 0.0% and 7.5%, the stiffness of the soil specimen reduces as the moisture content increases. In contrast, the specimens in Chapter 3 showed little variation in stiffness as the moisture content increased from 0.0% and 5.0%. This difference may be partly due to the improvements to the repeatability of the results, as the current experiments show very little overlap between series, but may also indicate a change in behaviour related to the reduced strain rate. These specimens remained partially-saturated throughout the experiment (Table 5.1), and so the reduction in stiffness with increased moisture content appears to indicate a reduction in inter-particle friction, as also observed in the quasi-static experiments in Chapter 3. This behaviour is similar to that observed in SHPB experiments by Martin et al. (2009), but to axial stresses of 200 MPa rather than 10 MPa, and with higher repeatability.

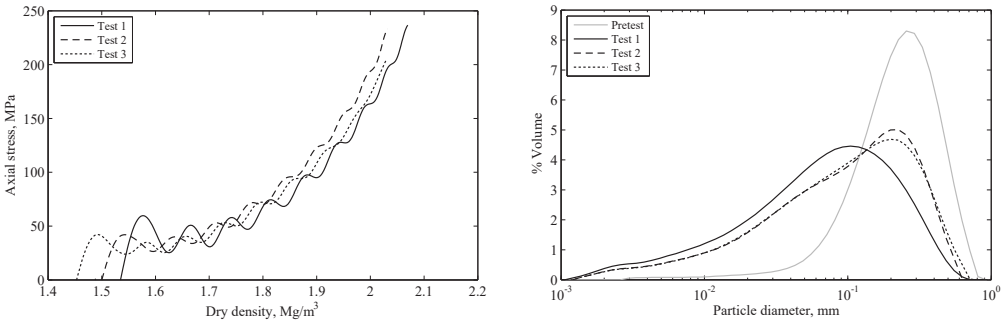


**(a)** $w = 0.0\%$

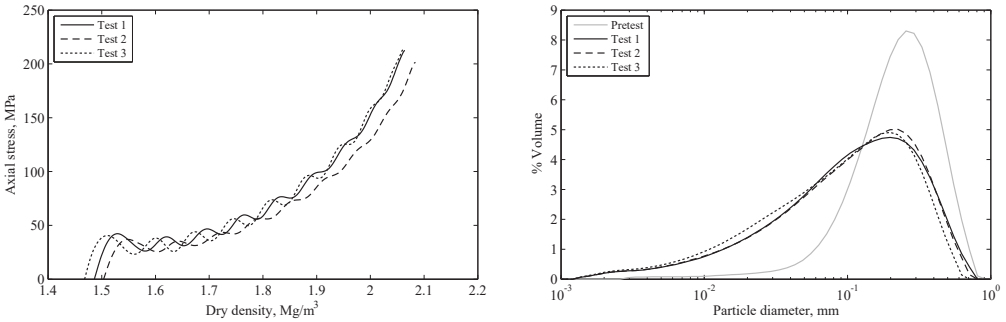


**(b)** $w = 2.5\%$

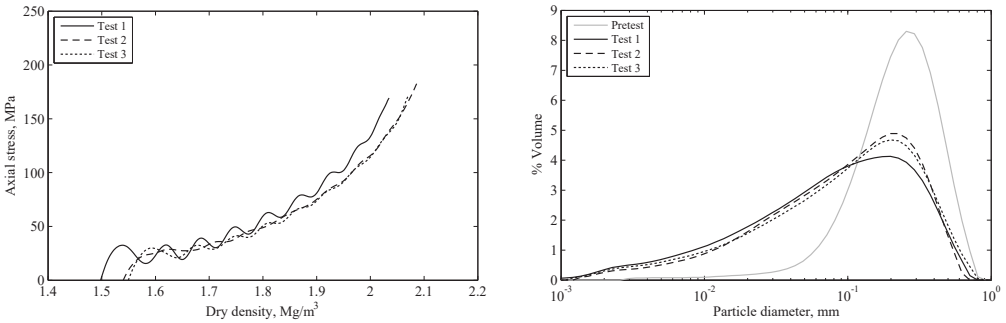


**(c)** $w = 5.0\%$

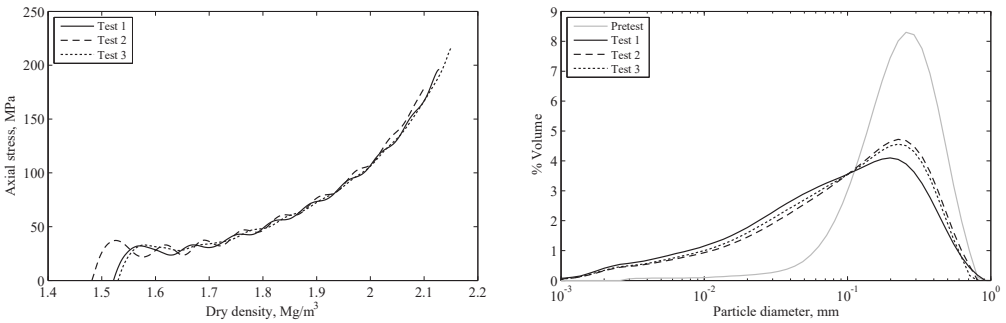


**(d)** $w = 7.5\%$

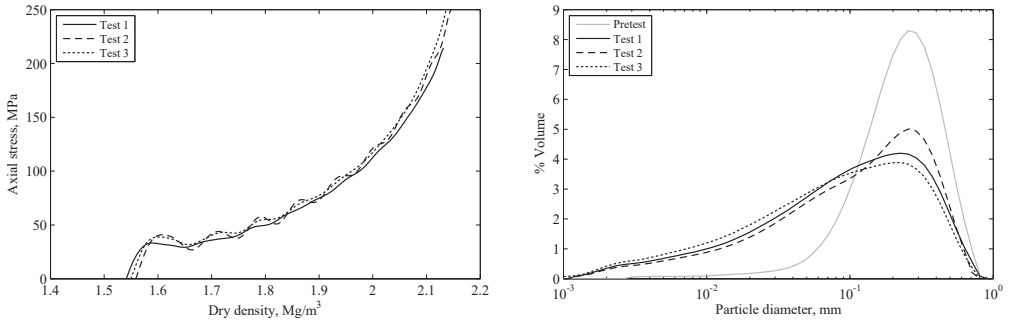


**(e)** $w = 10.0\%$

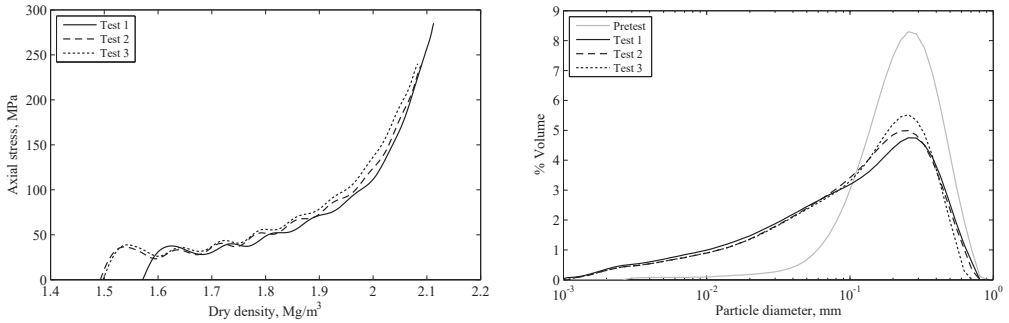


**(f)** $w = 12.5\%$

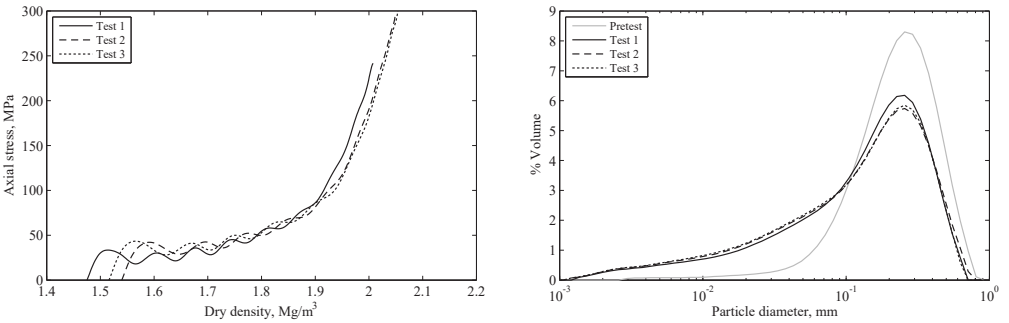


**(g)** $w = 15.0\%$

**Figure 5.7:** Axial stress – density results, and pre- and post-test particle size distributions, from recovery SHPB experiments on medium sand with moisture contents of a) 0.0%, b) 2.5%, c) 5.0%, d) 7.5%, e) 10.0%, f) 12.5%, and g) 15.0%.

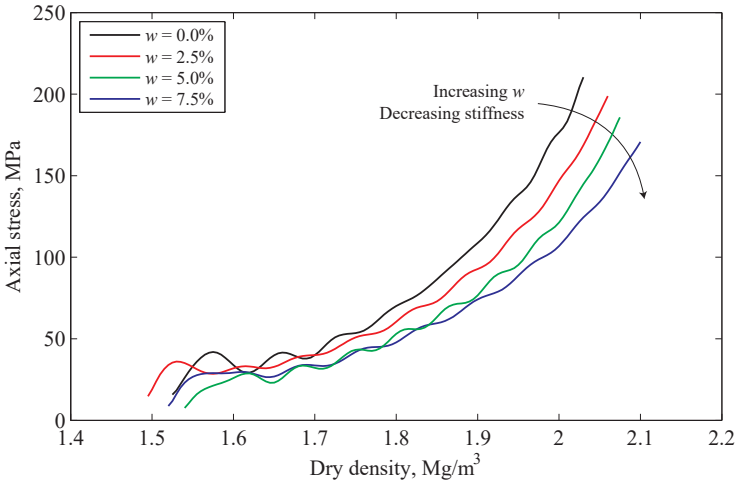


**(a)**

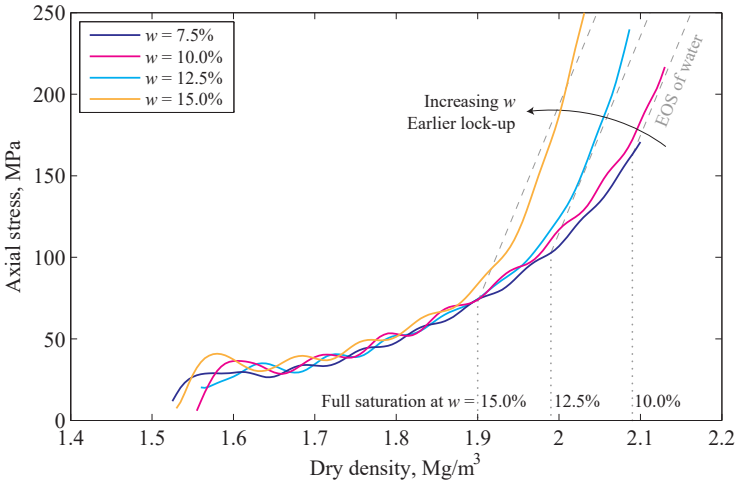


**(b)**

**Figure 5.8:** Axial stress – dry density results from SHPB experiments on medium sand with moisture contents of a) 0.0–7.5%, remaining partially saturated throughout, and b) 10.0–15.0%, reaching full saturation. (Mean results)

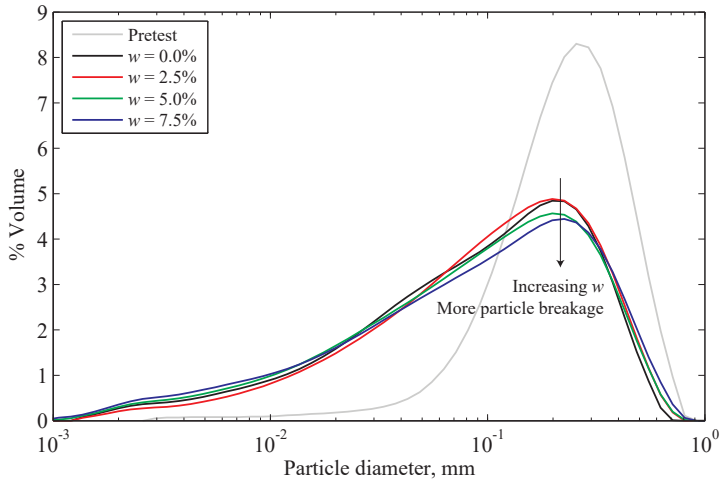


**(a)**

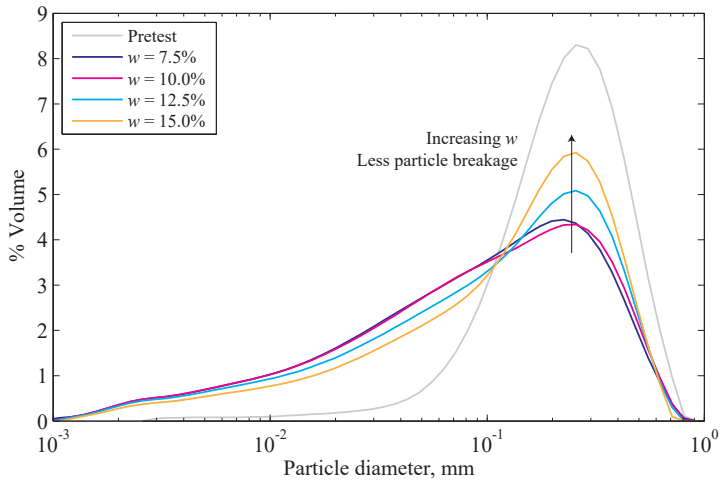


**(b)**

**Figure 5.9:** Post-test particle size distributions from SHPB experiments on medium sand with moisture contents of a) 0.0–7.5%, remaining partially saturated throughout, and b) 10.0–15.0%, reaching full saturation. (Mean results)

Figure 5.9a shows the mean pre- and post-test PSDs of the 0.0% to 7.5% moisture content specimens, where the particle breakage increases slightly with moisture content. This appears to be related to the larger strains obtained at higher moisture contents, where the reduction in inter-particle friction would increase the energy available for further breakage and compaction. In Chapter 3 it was speculated that localised loading of pore water may have caused the insensitivity to moisture content observed in the SHPB tests: as this should lead to a *reduction* in particle breakage with increased moisture content, no such effect appears to occur under the experimental conditions considered in this chapter.

### 5.4.2 Specimens reaching full saturation

For moisture contents of 10.0% to 15.0% the specimen reaches full saturation during loading, leading to a rapid increase in stiffness. This is shown in Figure 5.8b, where the theoretical density at full saturation is indicated for each moisture content. Prior to full saturation, the behaviour from 10.0% to 15.0% moisture content is very similar to the 7.5% specimens, showing no additional reduction in stiffness with increased moisture content. On reaching saturation the increased stiffness corresponds closely to the EOS of water, where $K_{\text{water}}$ =2.3 GPa (Veyera 1994), indicating that subsequent volume changes are dominated by the compression of the pore water.

The transition from partially-saturated to saturated behaviour occurs smoothly in each case, suggesting that parts of the specimen reach full saturation at slightly different densities. At low saturation ratios pore water exists as discrete drops adhering to the surface of particles and at the contact points between particles. At saturation ratios of around 25% and above, pore water tends to be continuous, and may migrate through the specimen under gravity, leading to a vertical distribution of moisture content (Atkinson and Bransby 1978). Such distributions have been observed by Clarke et al. (2015) in the preparation of large partially-saturated soil specimens, and may lead to a slightly higher moisture content at the bottom of the specimens in the current experiments.

Pore water loading is also shown in the recordings of radial stress (Figure 5.10), which increase rapidly on reaching full saturation, causing the Poisson's ratio of the specimens to increase to over 0.45. There is little significant variation in the radial stresses generated before saturation between moisture contents of 0.0% and 15.0%, and so the trend in mean stress – dry density behaviour in Figure 5.11 is similar to that observed in Figure 5.8.

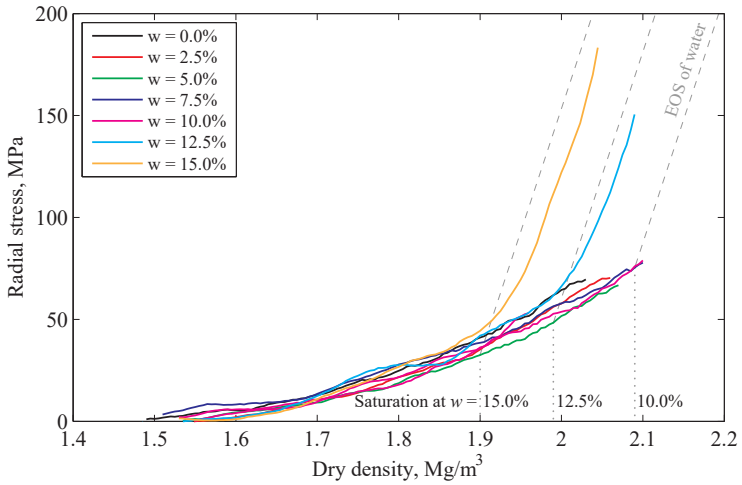


**Figure 5.10:** Radial stress – dry density results from SHPB experiments on medium sand with moisture contents of 0.0–15.0%. (Mean results)

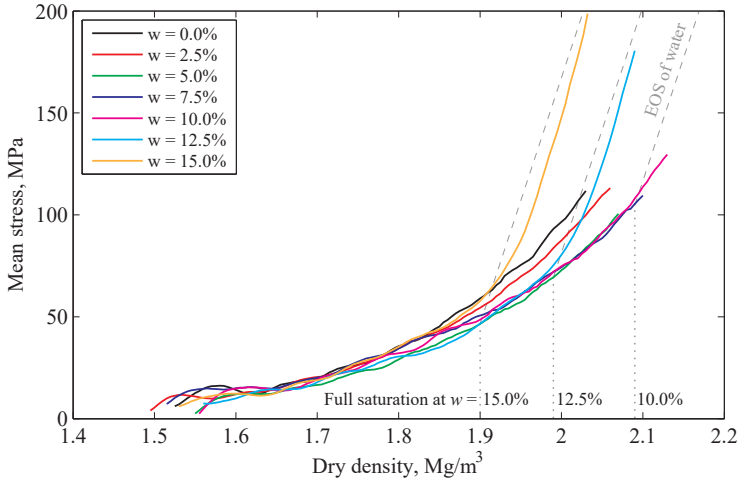


**Figure 5.11:** Mean stress – dry density results from SHPB experiments on medium sand with moisture contents of 0.0–15.0%. (Mean results)

Figure 5.9b shows the mean pre- and post-test PSDs of the 10.0% to 15.0% moisture content specimens, where particle breakage decreases as the moisture content increases. On reaching full saturation the sand particles move from being loaded mainly via particle-to-particle contact to include a significant hydrostatic component from the surrounding pore water. The resulting decrease in deviatoric stress makes particle breakage less likely, and so the majority of breakage will occur before the specimen reaches full saturation. This is confirmed through comparison of the 7.5% and 10.0% specimens. The 7.5% specimens achieve a dry density of approximately $2.10\,\mathrm{Mg\,m^{-3}}$, which is the point at which the 10.0% specimens reach full saturation. Through compression of the pore water the 10.0% specimens continue to a dry density of nearly $2.15\,\mathrm{Mg\,m^{-3}}$, but have a post-test PSD which is very similar to the 7.5% specimens. Full saturation occurs at lower stresses as moisture content increases, resulting in a reduction in particle breakage.

It is interesting to note that on reaching full saturation in the 10.0% tests, the stiffness of the soil is already similar to the stiffness of water, and so no significant increase in stiffness is observed. At lower moisture contents full saturation will occur at higher stresses, where the stiffness of the soil may exceed the stiffness of the pore water. The stiffness of the saturated soil would then be expected to be dominated by the soil skeleton rather than the pore water, and compaction would continue as it did before saturation, as shown in Figure 5.12. The moisture content at which this change in behaviour occurs will depend on the partially-saturated compressibility of the soil.

### 5.4.3 Strain-rate effects

It was noted above that the SHPB experiments in this chapter exhibited a decrease in stiffness with increasing moisture content, contrary to the results in Chapter 3. Figure 5.13 shows that this decrease in stiffness is similar in magnitude to that observed in the quasi-static experiments. Aside from the inertial effects which dominate the SHPB experiments at low strains, all three moisture contents show very similar behaviour at quasi-static and high strain rates, and so any strain rate effect appears to be negligible. This significant deviation from the previous results is unlikely to be entirely due to the improved axial measurements, and so suggests that a change in behaviour has occurred due to the difference in strain rate history between the two SHPB series. Further tests would be required to confirm this: use of the recovery SHPB to perform experiments to the strain rates and stresses in Chapter 3 may be useful to rule out the effects of experimental error.

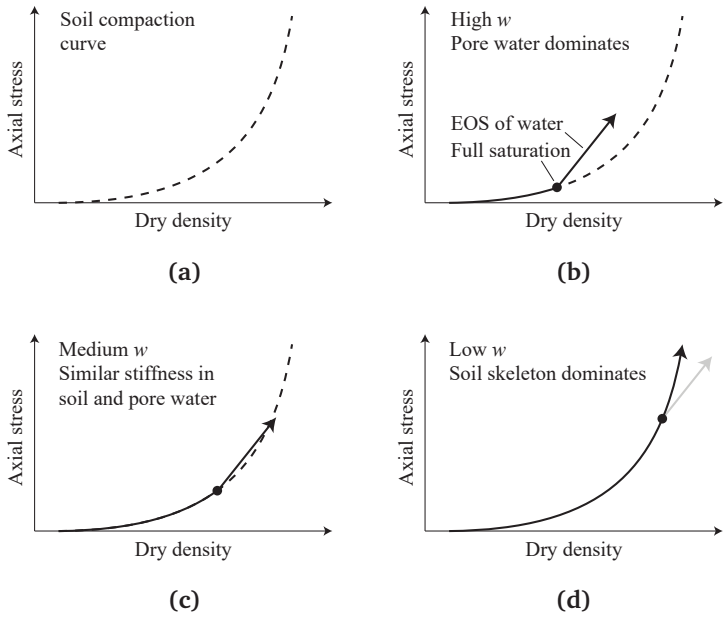


**Figure 5.12:** a) Soil compaction curve, and change in soil stiffness at full saturation in undrained conditions, at b) high, c) medium and d) low moisture contents.

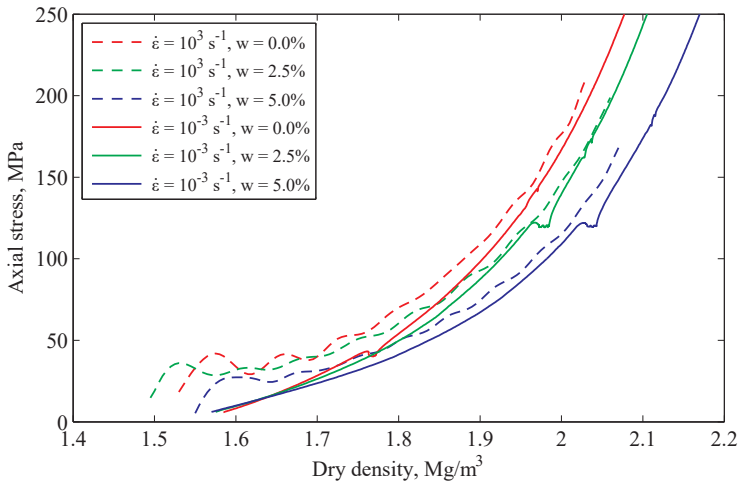


**Figure 5.13:** Mean axial stress – dry density results from SHPB experiments on medium sand with moisture contents of 0.0–5.0%, compared with the quasi-static experiments presented in Chapter 3.

A similar study on particle breakage in flyer plate experiments has also been carried out as part of the Force Protection Engineering research programme, of which this thesis forms a part. Perry et al. (2016) performed experiments on dry, partially-saturated ($w = 10\%$), and saturated medium sand and observed a qualitatively similar reduction in particle breakage as moisture content increased and full saturation occurred at lower stresses. The partially-saturated sand also had a lower stiffness than the dry sand, observed in this case as a lower shock velocity, and so similar compaction processes appear to occur at high and very high strain rates.

## 5.5 Summary

A recovery SHPB was designed to deliver a single compressive loading to the sand specimens, enabling post-test particle size analyses to be performed. Specimens were tested with moisture contents from 0.0% to 15.0%, and results were processed using the dispersion correction technique discussed in Chapter 4.

Between moisture contents of 0.0% and 7.5%, specimens remained partially-saturated throughout the experiment, and increases in moisture content led to a decrease in the stiffness of the sand and a small increase in particle breakage. The decrease in stiffness was similar to that observed in the quasi-static experiments in Chapter 3, and there appeared to be little dependence on strain rate between the SHPB and quasi-static tests. This apparent contradiction of the results obtained in Chapter 3 appears to be due to the variation in strain rate history between the two SHPB test series.

The 10.0%, 12.5% and 15.0% specimens reached full saturation during the experiment. The pre-saturation stiffness was similar to the 7.5% specimens in each case, and increased to the stiffness of water on reaching saturation, indicating that further volume changes were dominated by the compression of pore water. Full saturation occurred at lower dry densities as moisture content was increased, leading to a decrease in particle breakage. It was noted that at low moisture contents full saturation could occur when the stiffness of the soil was greater than that of the pore water, and that in these cases the soil would follow the regular soil compaction curve.

Chapter 6

# High-pressure compression and yield strength data for numerical modelling

## 6.1 Introduction

This chapter demonstrates the use of mac$^{2T}$ to provide high-pressure compaction and yield surface data for the calibration of soil models. Data generated for medium sand is used to assess the ability of LS-DYNA's 'soil' models to accurately represent sand behaviour in split Hopkinson pressure bar experiments, using experimental data to validate model performance. Recommendations are made for the development of a high-pressure soil model.

## 6.2 Quasi-static calibration data at high pressures

The literature review in Chapter 2 indicated that a lack of high-pressure experimental data was the likely cause for deficiencies in the models' ability to predict soil behaviour: for example, the extrapolation of two triaxial tests below 2 MPa to model buried explosive events (Fiserova 2006). The use of high-quality calibration data for the medium sand is therefore essential, and is the subject of this section. The compressibility and shear behaviour of medium sand is characterised to pressures of over 400 MPa, ensuring that no extrapolation is required to model the stresses in the SHPB experiments. The experimental results in previous chapters appear to show that differences in compression behaviour at different strain rates are due to inertial effects rather than true strain-rate dependence, and so quasi-static data is used to calibrate the models. Throughout this chapter, significant disagreement between experimental and numerical results will be taken as a sign that the model does not accurately represent the material behaviour: no attempts will be made to 'adjust' models to fit.

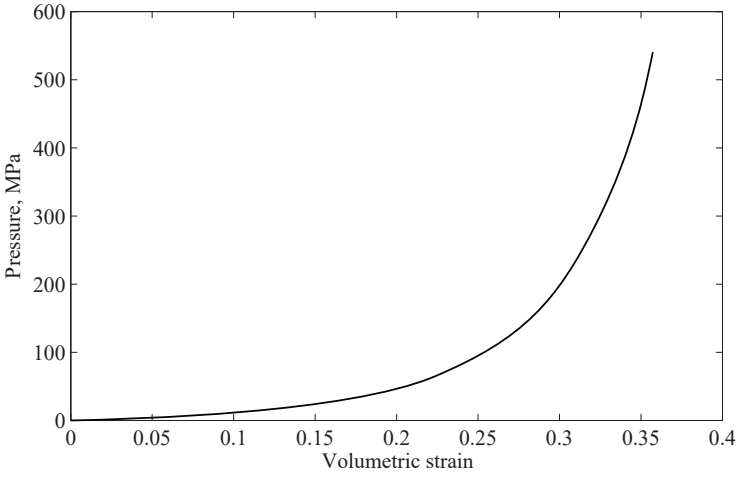


**Figure 6.1:** High-pressure quasi-static compressibility of dry medium sand prepared at $1.5\,\mathrm{Mg\,m^{-3}}$, expressed monotonically.

| Parameter | Value | Test method |
|---|---|---|
| Initial bulk modulus, $K_0$ | 30.5 MPa | Oedometer |
| Initial shear modulus, $G_0$ | 13.5 MPa | Oedometer |
| Poisson's ratio, $\nu$ | 0.32 | mac$^{2T}$ one-dimensional compression |
| Bulk unloading modulus, $K_u$ | 22 GPa | mac$^{2T}$ one-dimensional compression |

**Table 6.1:** Elastic constants derived from one-dimensional compression experiments on medium sand prepared at $1.5\,\mathrm{Mg\,m^{-3}}$.

### 6.2.1 Compressibility

The compressibility of the sand can be directly obtained from the mac$^{2T}$ one-dimensional compression data presented in Chapter 3. Many models require a compressibility curve to be expressed in terms of pressure and volumetric strain: this relationship is shown for dry medium sand in Figure 6.1, where the loading cycles have been removed to form a smooth, monotonic curve.

Various elastic constants are used by models to define soil characteristics such as Poisson's ratio and the unloading stiffness. These can each be derived from one-dimensional compression experiments, and are shown in Table 6.1. The initial shear modulus and initial bulk modulus define behaviour at low stresses, and so were investigated using standard oedometer experiments (BS 1377–5:1990).

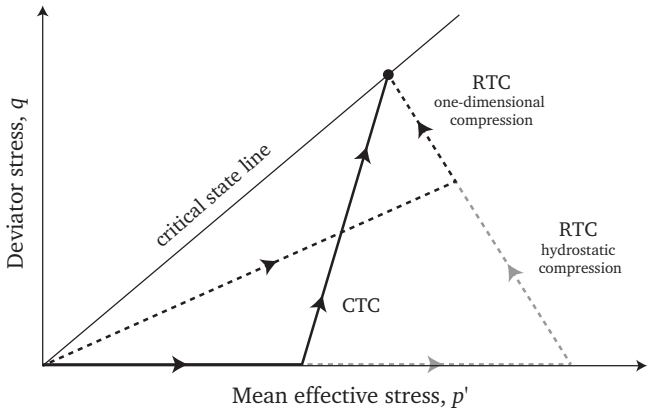


**Figure 6.2:** Stress paths in conventional triaxial compression (CTC) and reduced triaxial compresion (RTC) tests with the same CSL intersect.

### 6.2.2 Yield surface

Most models require information on the yield surface, or failure envelope, of a material, which defines the relationship between shear strength and mean stress. In the case of soils this surface is analogous to the critical state line discussed in §2.5.

The yield surface of dry medium sand was obtained at high pressures by using mac$^{2T}$ to perform reduced triaxial compression (RTC) tests. RTC tests differ from the CTC tests described in §2.5 in that deviatoric stresses are applied by reducing the cell pressure under a constant axial stress, rather than increasing axial stress under a constant cell pressure. Both the CTC and RTC tests typically begin with hydrostatic compression, but true hydrostatic pressure cannot be applied to sand in mac$^{2T}$, as the large displacements would lead to contact between the loading platens. Instead, initial compaction of the sand in these RTC tests was achieved in one-dimensional compression, as shown by the load paths in Figure 6.2. Experiments were performed as follows:

a) Sand specimens were prepared in the steel testing box as described in §3.4.3, and loaded into mac$^{2T}$.

b) The x-, y- and z-axes were each loaded to 7 kN (2.8 MPa).

c) The y- and z-axes were switched to displacement control with a displacement rate of zero.

d) With the x-axis in load control the specimen was loaded in one-dimensional compression to $\sigma_x$ =120 MPa (points 1–2 in Figure 6.3).

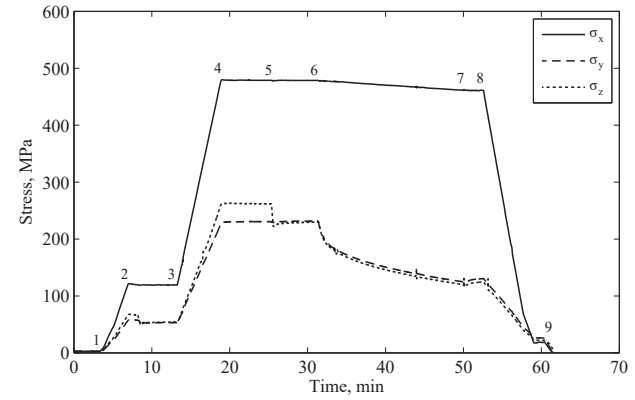


**(a)**

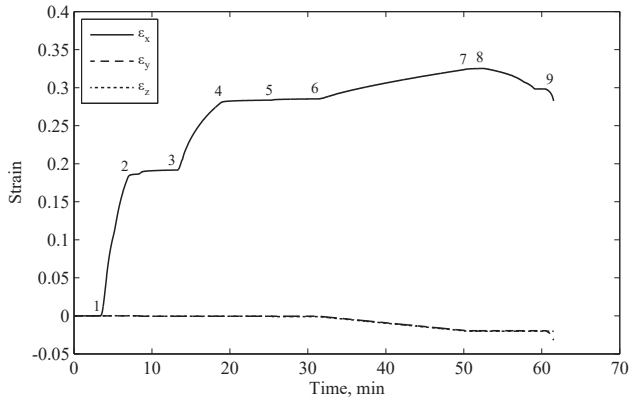


**(b)**

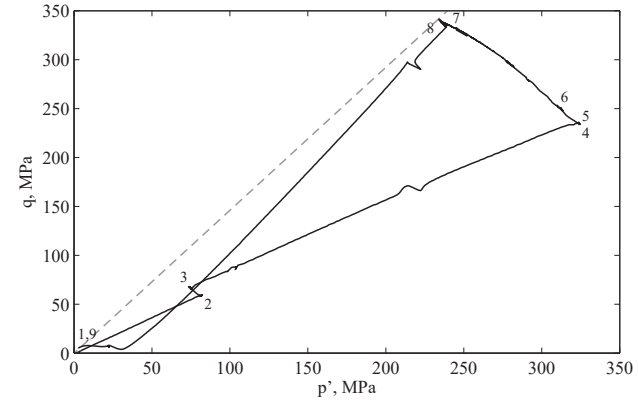


**(c)**

**Figure 6.3:** RTC experiment on medium sand, showing a) specimen stresses, b) specimen strains and c) the stress path in $q$–$p'$ space.

e) The passive platens were backed off by 0.1 mm to ensure that friction between the active and passive blocks did not contribute to the stiffness of the soil specimen (points 2–3).

f) The specimen was loaded in one-dimensional compression to the peak mean stress, $p'_0$ (points 3–4). Peak mean stresses of 325 MPa, 445 MPa and 555 MPa where used in the current test series.

g) Before beginning the main deviatoric portion of the test, the stresses in the y- and z-axes were equalised, in this case by reducing $\sigma_z$ (points 5–6).

h) The load in the x-axis was fixed by setting the loading rate to zero.

i) The y- and z-axes were backed off, decreasing the lateral stresses, and causing the stress path to turn towards the yield surface (points 6–7). A small decrease in axial stress occurred during the shearing due to the increasing cross-sectional area of the x-axis.

j) Displacement of the y- and z-axes was halted (points 7–8), $\sigma_x$ was reduced to around 20 MPa, and then all three axes were unloaded together (points 8–9).

As these are the first experiments of their kind in the literature, the high-pressure shear behaviour of the sand was not known before testing, and there was a risk that a sudden failure of the specimen would lead to a loss of control of the actuators and damage the mac$^{2T}$ apparatus. To reduce this risk, lateral displacements in the current experiments were limited to 1 mm and, as a result, the specimens did not quite reach a critical state (§2.5). However, least-squares fits to the $q$–$\varepsilon_x$ data in Figure 6.4 show that in each case the specimen was within 4 MPa of its utimate strength, and so the small associated error was easily accounted for. These extrapolations also predict that the largest lateral displacement required to reach a critical state would be approximately 1.6 mm (for $p'_0 = 555$ MPa), and so shearing to ultimate strength may be achievable in future experiments.

Figure 6.5 shows the results of the three RTC tests on dry medium sand, which can be used to define a linear yield surface for the sand to pressures of over 400 MPa. As the sand is cohesionless the surface passes through the origin, with a gradient, $M$, of 1.47, equivalent to an angle of shearing resistance $\phi' = 36.6°$. Each of the constitutive models in LS-DYNA define the yield surface of the material using different stress spaces and sets of parameters: these are indicated in the discussion of each model. A summary of the stress spaces is also supplied in Appendix C.

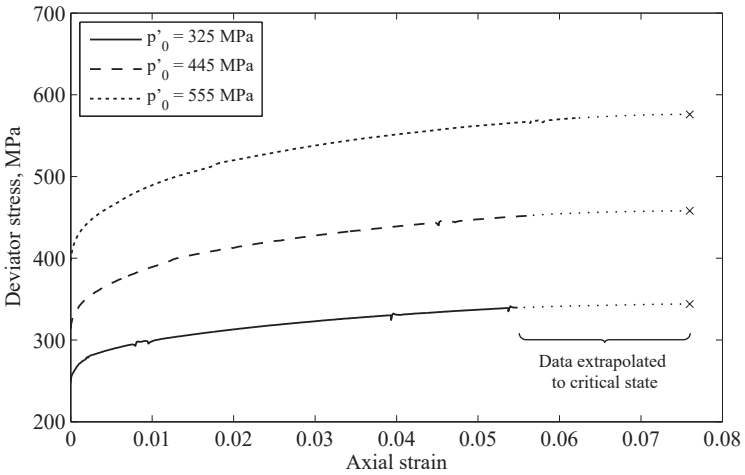


**Figure 6.4:** RTC experiments on medium sand, showing $q$–$\varepsilon_x$ behaviour during deviatoric loading. Extrapolation to the critical state was carried out using a least-squares quadratic fit to the data.

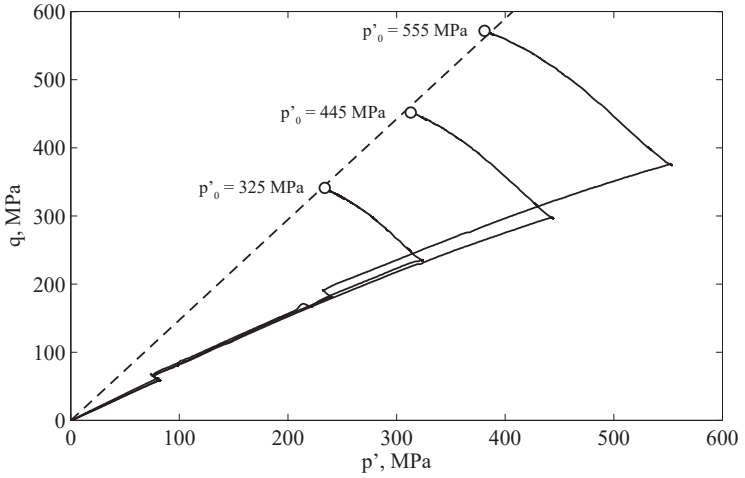


**Figure 6.5:** RTC experiments on medium sand, with unloading omitted for clarity.

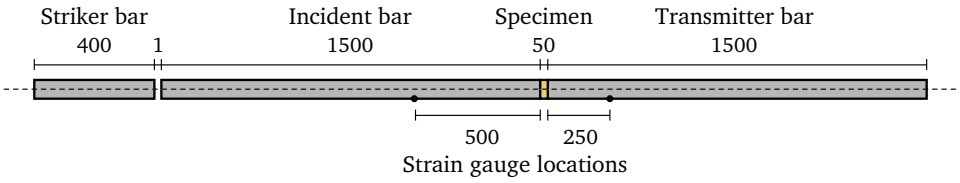


**Figure 6.6:** LS-DYNA model geometry and locations of strain gauge recordings.

## 6.3 Model geometry and setup

Figure 6.6 shows the FE model used to assess the performance of the constitutive models in LS-DYNA, which reproduces the geometry of the SHPB used in tests on dry medium sand in Chapter 3. The stainless steel striker, incident and transmitter bars all have a diameter of 25 mm, a density of 7850 kg m$^{-3}$, a Young's modulus of 168 GPa and Poisson's ratio of 0.29, and are modelled using the *Elastic* material model (`*MAT_001`).

The model parts are represented using a Lagrangian mesh, which is axisymmetric about the bar axis. Mesh files for the SHPB were generated using a MATLAB script developed by Dr Sam Rigby (personal communication, 2014): following previous mesh sensitivity studies by Dr Rigby, 2.5 mm and 0.625 mm meshes were adopted for pressure bar and specimen elements, respectively.

The striker bar was given an initial velocity of 22.4 m s$^{-1}$ to match the experimental incident waves in Chapter 3, and the sand specimen was set up with an initial length of 50 mm. In the physical test the sand specimen is confined laterally by a steel ring, and so this is approximated by applying a boundary condition to restrict lateral displacement of the nodes on the surface of the specimen. Experimental data was collected from the strain gauges on the surface of the pressure bars, and so the constitutive models will be assessed using the strains recorded at the same locations in the model, as noted on Figure 6.6.

## 6.4 LS-DYNA constitutive models for sand

A number of the constitutive models supplied with LS-DYNA are identified in the documentation as being suitable for modelling soils (LSTC 2012). These range from simple compressibility curves and perfectly-plastic yield surfaces to more complex models incorporating pore water effects, dilatency, hardening and strain-rate effects. A brief overview of each model is provided below, and a comparison of the key features of the models are shown in Table 6.2.

| *MAT_ | Model name | Failure surface space | Failure surface definition | Pressure dependent | Strain-rate dependent | Hardening criteria | Dilatency | Compressibility control |
|---|---|---|---|---|---|---|---|---|
| 005 | *Soil and Foam* | $J_2$–$p$ | Quadratic | Yes | No | None | No | $P$–$\varepsilon_v$, tabulated |
| 014 | *Soil and Foam with Failure* | $J_2$–$p$ | Quadratic | Yes | No | None | No | $P$–$\varepsilon_v$, tabulated |
| 016 | *Pseudo Tensor (I)* | $q$–$p$ | Tabulated | Yes | Shear strength scale factor | None | No | Defined EOS |
| 025 | *Geological Cap* | $\sqrt{J_2}$–$I_3$ | Coefficients | Yes | No | Associated, kinematic | Yes | Cap surface |
| 078 | *Soil and Concrete* | $J_2$–$p$ | Tabulated | Yes | No | No | No | $P$–$\varepsilon_v$, tabulated |
| 079 | *Hysteretic Soil* | $\tau$–$\gamma$ | Tabulated, coefficients | Yes | No | (Nested PP surfaces) | Yes | Elastic moduli |
| 145 | *Schwer–Murray Cap* | $\sqrt{J_2}$–$I_3$ | Coefficients | Yes | Viscoplasticity | Nonassociated, kinematic | Yes | Cap surface |
| 147 | *FHWA Soil Model* | $p$, $J_2$, $J_3$ | $\phi$, $c$, coefficients | Yes | Viscoplasticity | Associated | Yes | No |
| 173 | *Mohr–Coulomb* | $\tau$, $\sigma$ | $\phi$, $c$ | Yes | No | Nonassociated | Yes | No |
| 193 | *Drucker–Prager* | $\tau$, $\sigma$ | $\phi$, $c$ | Yes | No | Nonassociated | Yes | No |

**Table 6.2:** Comparison of LS-DYNA soil models.

**Soil and Foam (*MAT_005)** A simple pressure-dependent model which simulates crushing through volumetric deformation, provides a pressure-dependent quadratic yield surface in $J_2 - P$ space, and unloads elastically to a tensile cut-off.

**Soil and Foam with Failure (*MAT_014)** Similar to *Soil and Foam*, with the addition of a failure pressure where an element loses its ability to carry tension.

**Pseudo Tensor (*MAT_016)** Designed for concrete, but by excluding the parameters for the reinforcement material, can be used for soils, and in this configuration is similar to *Soil and Foam*. Compressibility is defined using the equation of state *Tabulated* or *Tabulated Compaction*. Yield surfaces are tabulated in $(\sigma_1 - \sigma_3) - P$ space. Strain-rate dependence can be incorporated by applying a yield stress multiplier.

**Geological Cap (*MAT_025)** A two-invariant cap model with kinematic hardening, where the yield surface is defined in $\sqrt{J_2}$–$J_1$ space with both tension cut-off and cap surfaces. The hardening function can be defined, and an associated flow rule is assumed.

**Soil and Concrete (*MAT_078)** Similar to *Soil and Foam*, with the addition of options for the initiation of cracks and definition of residual strengths.

**Hysteretic Soil (*MAT_079)** A nested-surface model, with the ability to define up to ten elastic–perfectly-plastic surfaces. Elastic moduli are pressure-dependent, and control the compressibility of the soil. Yield stresses are controlled by a shear stress–shear strain relationship which is modified for individual surfaces through a number of additional coefficients. A number of parameters are supplied to control dilatancy in sandy soils.

**Schwer–Murray Cap (*MAT_145)** A cap model based on *Geological Cap*, with strain-rate dependence in the form of viscoplasticity and strain softening.

**FHWA Soil Model (*MAT_147)** A modified Mohr-Coulomb yield surface, includes parameters to model excess pore water pressure, viscoplasticity, strain softening, kinematic hardening and deletion of distorted elements.

**Mohr–Coulomb (*MAT_173)** A Mohr–Coloumb yield surface defined using a value for cohesion and angle of friction. The dilation angle is used to define a nonassociated flow rule, and both $\phi$ and $\psi$ can vary with plastic strain.

| Group | Models |
|---|---|
| Soil and Foam | *Soil and Foam** |
| | *Soil and Foam with Failure* |
| | *Pseudo Tensor** |
| | *Soil and Concrete* |
| Mohr–Coulomb | *Mohr–Coulomb** |
| | *Drucker–Prager* |
| | *FHWA Soil* |
| Cap Models | *Geological Cap** |
| | *Schwer–Murray Cap* |
| Nested Surface | *Hysteretic Soil** |

**Table 6.3:** Grouping of similar LS-DYNA soil models. Models selected to represent the groups are indicated with an asterisk.

**Soil Brick (*`MAT_192`)** A model is designed for modelling overconsolidated clays. The yield surface is initially in the form of a Von Mises surface, which can be altered using a shape factor, and has additional parameters for anisotropy.

**Drucker–Prager (*`MAT_193`)** A modified Drucker–Prager yield surface defined using a value for cohesion and angle of friction. The dilation angle is used to define a nonassociated flow rule, and both $\phi$ and $\psi$ can vary with plastic strain. The yield surface can be modified using a shape factor.

Many of these models have similar approaches to defining the equation of state and failure surface of the material, and so they have been grouped in order to reduce the number of comparisons which have to be made, as shown in Table 6.3. *Soil Brick* has been excluded as it is not suitable for modelling cohesionless soils. The following sections will consider the suitability of a representative model from each group for modelling the behaviour of sand at high pressures and strain rates, in each case assessing:

- the ease with which the model can be calibrated using quasi-static experimental data for medium sand; and
- the performance of the model when validated against the experimental SHPB data.

| Variable | Description |
|---|---|
| `ro` | Initial density. [$\mathrm{kg\,m^{-3}}$] |
| `g` | Elastic shear modulus. [Pa] |
| `bulk` | Bulk modulus, used to define the unloading response. [Pa] |
| `pc` | Tensile pressure cut off. [Pa] |
| `eps1-eps10` | Volumetric strain values corresponding to pressures `p1-p10`. Volumetric strain is given by the natural log of relative volume. Negative in compression. |
| `p1-p10` | Pressure values corresponding to volumetric strains `eps1-eps10`. Positive in compression. [Pa] |
| `a0, a1, a2` | Constants used to create a quadratic fit yield function in $J_2$–$P$ space. |
| `vcr` | Volumetric crushing option (boolean): 0: on, 1: loading and unloading defined by pressure-strain curve. |
| `ref` | Use reference geometry to initialise pressure (boolean): 0: off, 1: on. |

**Table 6.4:** Variables for definition of LS-DYNA *Soil and Foam*.

| P (MPa) | 0 | 6 | 12 | 21 | 36 | 56 | 86 | 132 | 207 | 320 |
|---|---|---|---|---|---|---|---|---|---|---|
| $\epsilon_{eps}$ | 0 | -0.08 | -0.12 | -0.16 | -0.20 | -0.24 | -0.28 | -0.32 | -0.36 | -0.40 |

**Table 6.5:** Pressure–strain relationship used in *Soil and Foam*, derived from experimental quasi-static data on dry sand.

## 6.5 Validation of LS-DYNA sand models

### 6.5.1 Soil and Foam

#### Calibration

*Soil and Foam* (`*MAT_005`) is a simple pressure-dependent model designed for foams and soils which are confined within a structure (LSTC 2012). Definition of the material requires the variables in Table 6.4, comprising of a compressibility curve, a shear strength function, shear and bulk moduli and a tensile cutoff.

The variables `rho`, `p1-p10` and `eps1-eps10` define the compressibility of the soil (`vcr` = 0), and were defined using the pressure–volumetric strain relationship from §6.2.1. Ten pressure and volumetric strain pairs can be provided to the model, and these were chosen to best describe the experimental curve, as shown in Figure 6.7 and Table 6.5. `eps1-eps10` are compression negative, and

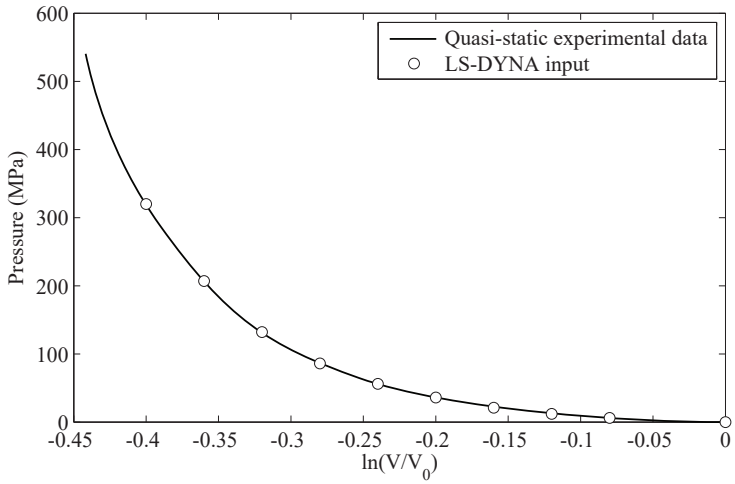


**Figure 6.7:** Medium sand pressure–strain relationship used in LS-DYNA, derived from experimental quasi-static data on dry sand.

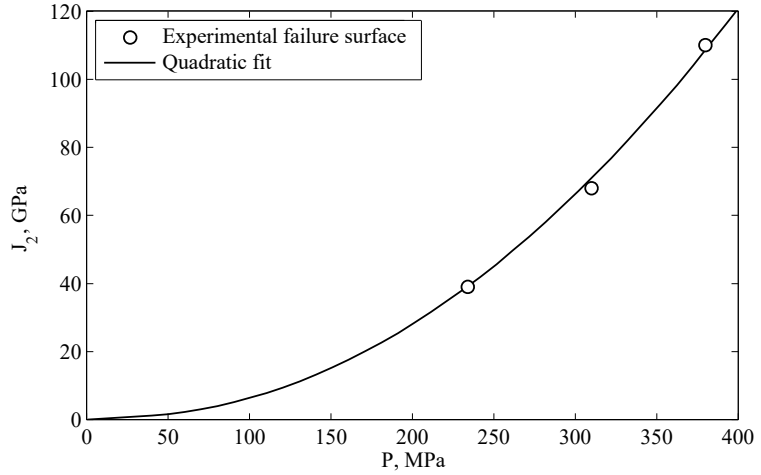


**Figure 6.8:** Shear strength relationship used in LS-DYNA, derived from triaxial tests on dry sand.

are expressed as the natural logarithm of relative volume:

$$\epsilon_{eps} = \ln\left(\frac{V}{V_0}\right) \tag{6.1}$$

The variables `a0`, `a1` and `a2` are coefficients in the deviatoric perfectly-plastic function $\phi$, which is defined as

$$\phi = J_2 - \left(a_0 + a_1 P + a_2 P^2\right) \tag{6.2}$$

where $J_2$ is the second deviatoric invariant and $P$ is pressure. This function can be fitted to the experimental data in §6.2.2 by plotting a strength envelope in $J_2$–$P$ space: the least-squares fit shown in Figure 6.8 provides the coefficients `a0` $= 0$, `a1` $= 4.51$ and `a2` $= 0.693$. The tensile cut-off, `pc`, was set to zero, as the sand is cohesionless. These variables are provided to LS-DYNA in the form shown in Table B.1, where the variable `mid` is the material ID, a unique integer identifier.

### Validation

A comparison of the experimental and modelled sand behaviour is shown in Figure 6.9 in terms of axial stress and dry density. The *Sand and Foam* specimen has a much lower stiffness than both the quasi-static and dynamic experimental specimens, indicating that it does not represent the sand behaviour well.

The volumetric response in Figure 6.10 shows that the defined compressibility curve is followed closely, though the pressures generated in the model (400 MPa) far exceed the experimentally measured pressures ($< 250$ MPa), which suggests that the material has insufficient resistance to shear forces. This is confirmed by Figure 6.11, which shows that the modelled sand deviates from the experimental response at low mean stresses and generates very little shear resistance, despite being far from the yield surface. The reason for this is that the shear modulus defined in the model does not increase as the soil compacts, as is expected, but remains constant throughout the loading. A constant shear modulus causes the Poisson's ratio of the specimen to increase rapidly as the bulk modulus increases during soil compaction, as shown by Figure 6.12.

### Conclusion

While the model is simple to populate with experimental data, due to a fixed shear modulus, any large changes in bulk modulus will cause *Soil and Foam* to deviate significantly from the expected soil behaviour. As a result it is not suitable for modelling soil behaviour at high pressures.

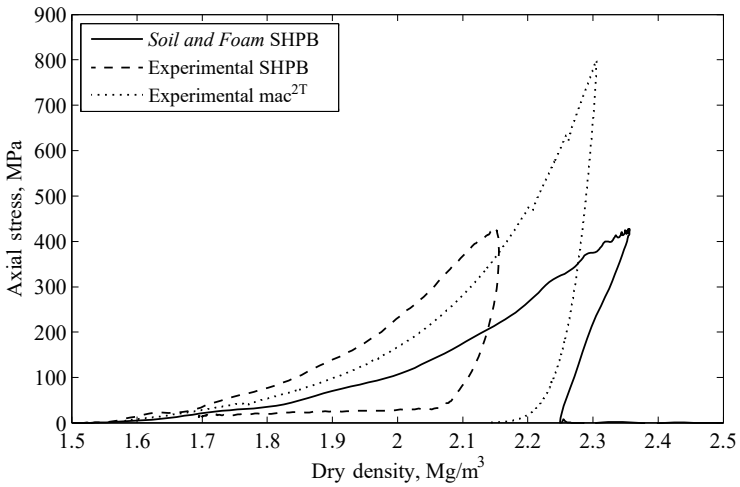


**Figure 6.9:** Axial stress–dry density behaviour of *Soil and Foam* SHPB specimen compared to mean experimental data.

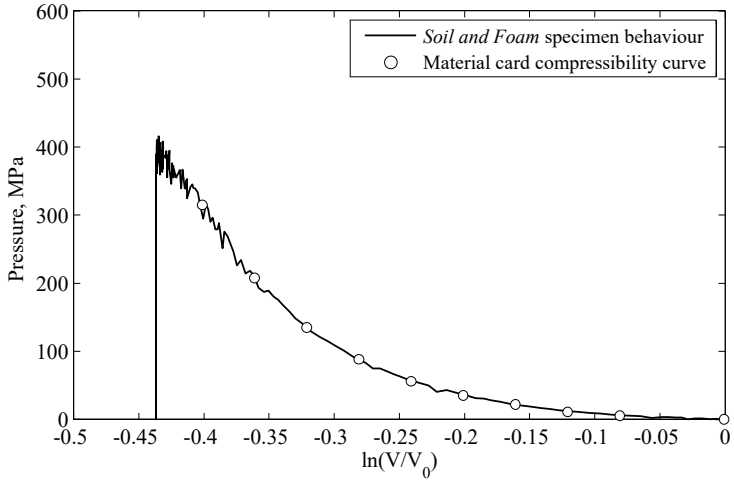


**Figure 6.10:** Pressure–volume behaviour of *Soil and Foam* SHPB specimen, and defined compressibility curve.

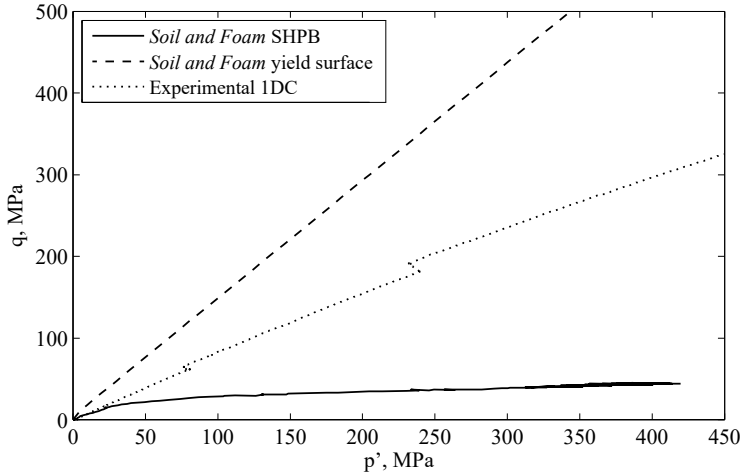


**Figure 6.11:** Shear behaviour of *Soil and Foam* SHPB specimen compared to experimental one-dimensional compression.

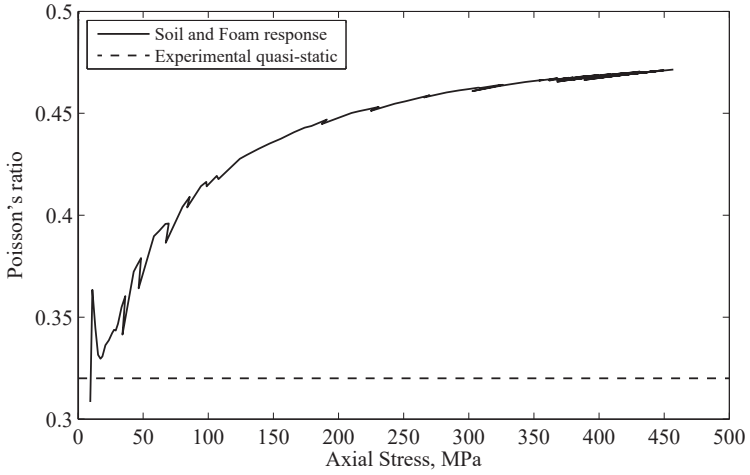


**Figure 6.12:** Effect of fixed shear modulus on Poisson' ratio of *Soil and Foam* specimen.

| Variable | Description |
|---|---|
| `ro` | Initial density. [$\mathrm{kg\,m^{-3}}$] |
| `g` | Shear modulus. [Pa] |
| `pr` | Poisson's ratio. |
| `sigf` | Tensile cutoff. [Pa] |
| `x1-x10` | Yield surface: pressures. [Pa] |
| `ys1-ys10` | Yield surface: yield stresses. [Pa] |

**Table 6.6:** Variables for definition of LS-DYNA *Pseudo-Tensor* in Mode 1.

### 6.5.2 Pseudo-Tensor

#### Calibration

*Psuedo-Tensor* (`*MAT_016`) is a simple model for concrete, but by removing the terms for steel reinforcement (Mode 1) can be used to model soils, and in this format is similar to *Soil and Foam*, but with an explicitly defined Poisson's ratio. Definition of the material in Mode 1 requires the variables in Table 6.6.

Compressibility of the soil is defined using the *Tabulated Compaction* equation of state, which defines pressure as

$$P = C(\epsilon_{eps}) + \gamma T(\epsilon_{eps})E \tag{6.3}$$

Neglecting the temperature terms, pressure can be defined using the bulk modulus parameter, $C$, which is a function of volumetric strain, $\epsilon_{eps} = \ln(V/V_0)$. The parameters `ev1-ev10` and `c1-c10` were populated using the same pressure–volumetric strain data used for *Soil and Foam*, as shown in the test card in Figure B.2. The shear modulus and Poisson's ratio are defined using the data in §6.2.1 as `rnu` $= 0.32$ and `g` $= 13\,\mathrm{MPa}$.

The yield surface is defined in $q$–$p'$ space using tabulated pairs of pressure and yield stress. As the yield surface is linear in $q$–$p'$ space (Figure 6.5), two points were defined using the data in §6.2.2: the origin and $p' = 380\,\mathrm{MPa}$, where $q = 570\,\mathrm{MPa}$. The calibrated LS-DYNA material card is shown in Figure B.2.

#### Validation

The axial stress–volumetric strain behaviour of the *Pseudo-Tensor* specimen is shown in Figure 6.13. Although stiffer than the *Soil and Foam* behaviour, the specimen still behaves less stiffly than both the quasi-static and dynamic experimental specimens. Unlike *Soil and Foam*, the shear modulus is permitted to

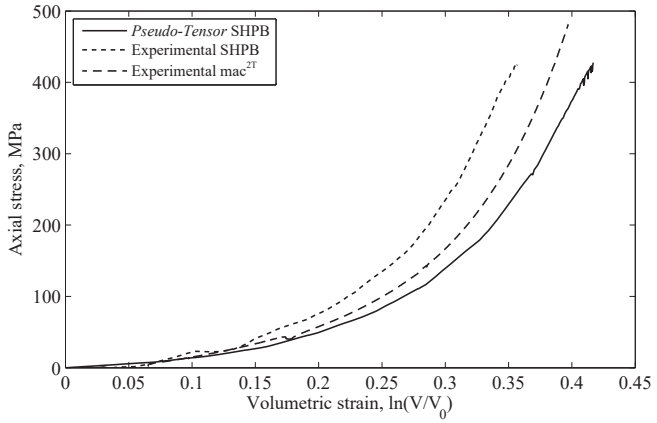


**Figure 6.13:** Axial stress–volumetric strain behaviour of *Pseudo-Tensor* SHPB specimen.

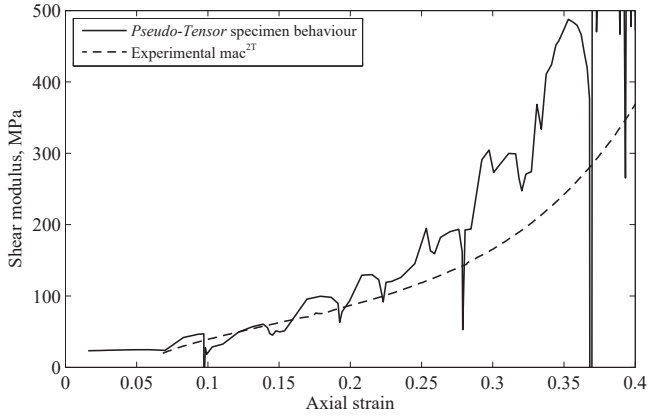


**Figure 6.14:** Shear modulus behaviour of *Pseudo-Tensor* SHPB specimen.

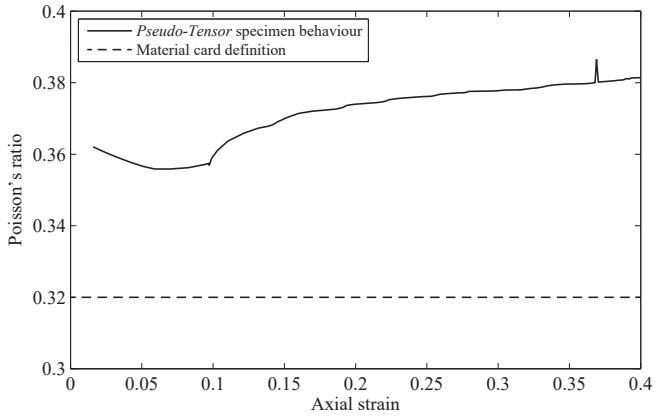


**Figure 6.15:** Poisson's ratio behaviour of *Pseudo-Tensor* SHPB specimen.

increase throughout the compaction process, although this occurs more rapidly than in the experiments (Figure 6.14). While the Poisson's ratio is explicitly defined, the specimen behaviour exceeds this value throughout the entire experiment (Figure 6.15), leading to the reduced stiffness observed above. The Poisson's ratio of the specimen remained at a similar value when the defined Poisson's ratio was altered to values of 0.1 and 0.4. It is not clear why *Pseudo-Tensor* fails to maintain the defined value, although this cannot be due to the inertial effects discussed in §3.6.2, as this would result in a lower rather than higher Poisson's ratio. Analysis of the variation of radial stress across the specimen also shows that no significant inertial effect occurs in the current model.

#### Conclusion

*Pseudo-Tensor* is easily populated with experimental data, and improves on *Soil and Foam* by allowing shear modulus to develop during compaction and by defining Poisson's ratio explicitly. However, as the defined value of Poisson's ratio is not adhered to in the model, the axial stiffness of the specimen is not representative of the experimental data.

### 6.5.3 Mohr–Coulomb

#### Calibration

*Mohr–Coulomb* (`*MAT_173`) is an implementation of the Mohr–Coulomb constitutive model for soils, which has a yield criterion of the form

$$\tau = \sigma' \tan \phi' + c' \tag{6.4}$$

where $\tau$ is the shear strength, $\sigma'$ is the effective normal stress, $\phi'$ is the angle of shearing resistance and $c'$ is the intercept of the yield surface with the $\tau$ axis. Definition of the yield function and plastic potential function requires the variables in Table 6.7: other parameters for the definition of joints in rocks and variation of properties with depth have been omitted.

The angle of shearing resistance can be found by plotting Mohr's circles of stress using the data in §6.2.2, as shown in Figure 6.16. This provided a value of `phi` $= 36.6° = 0.639$ rad. As the sand is cohesionless, `c` $= 0$, and as the dilation angle reduces to zero above small strains and at high stresses, `psi` $= 0$. The Poisson's ratio and elastic shear modulus were defined using the quasi-static data in §6.2.1, providing values of `rnu` $= 0.32$ and `g` $= 13$ MPa, however no compaction response or EOS input is provided in the model. The calibrated LS-DYNA material card is shown in Table B.3.

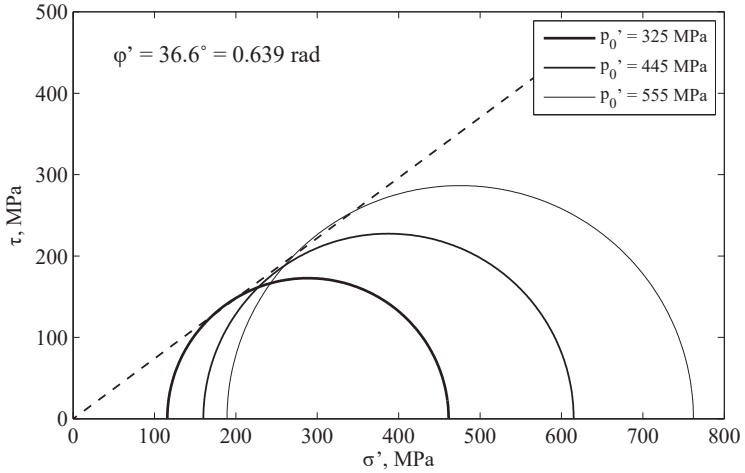


**Figure 6.16:** Angle of shearing resistance of medium sand.

| Variable | Description |
|---|---|
| `ro` | Initial density. [kg m$^{-3}$] |
| `gmod` | Elastic shear modulus. [Pa] |
| `rnu` | Poisson's ratio. |
| `phi` | Angle of shearing resistance. [rad] |
| `cval` | Cohesion. [Pa] |
| `psi` | Dilation angle. [rad] |

**Table 6.7:** Variables for definition of LS-DYNA *Mohr–Coulomb*.

### Validation

*Mohr–Coulomb* failed with negative volume errors at low stresses in the SHPB model, as the lack of a compaction response leads it to behave linear-elastically throughout the loading.

### Conclusion

The use of common geotechnical parameters and the ability to define a Poisson's ratio make *Mohr–Coulomb* attractive as a soil model, but as it cannot be accompanied with a compaction response, it is inappropriate for modelling the behaviour of medium sand at high pressures.

### 6.5.4 Cap models

#### Calibration

*Geologic Cap* (*MAT_25) is a two-invariant cap model, composed of yield, cap and tension cut-off surfaces (Figure 6.17a), which are defined using the variables in Table 6.8. In a cap model, interaction with the cap surface results in plastic compaction according to the defined hardening law, and the cap expands to accommodate the new stress state.

The initial bulk and shear moduli were defined using the quasi-static data in §6.2.1, providing values of k = 30.5 MPa and g = 13.5 MPa. The yield surface is defined in $\sqrt{J_2}$–$I_1$ space as the sum of linear and exponential functions of $I_1$:

$$\sqrt{J_2} = \alpha - \gamma e^{-\beta I_1} + \theta I_1 \tag{6.5}$$

The data from §6.2.2 was used to define this as a linear surface with theta = 0.28 and alpha, gamma and beta equal to zero. As the sand is cohesionless the tension cut-off was set to toff = 0.

The cap surface is defined as

$$\sqrt{J_2} = \frac{1}{r}\sqrt{(x(\kappa) - l(\kappa))^2 - (I_1 - l(\kappa))^2} \tag{6.6}$$

where $x(\kappa)$ is the intersection of the cap surface with the $I_1$ axis,

$$x(\kappa) = \kappa + r(\alpha - \gamma e^{-\beta\kappa} + \theta\kappa) \tag{6.7}$$

$l(\kappa)$ is defined as

$$l(\kappa) = \begin{cases} \kappa, & \text{if } \kappa > 0 \\ 0, & \text{if } \kappa \leq 0 \end{cases} \tag{6.8}$$

and the hardening parameter $\kappa$ is related to the plastic volumetric strain, $\epsilon_v^p$. High-pressure hydrostatic compression data is not available for the medium sand, and so an assumption of the shape of the cap must be made before the hardening law can be calibrated using one-dimensional compression data. The simplest cap definition is that of a spherical surface centred on the origin, and so this is approximated by setting r = 1.55. The development of this cap surface during a one-dimensional compression test is shown in Figure 6.18.

The hardening law is defined as an exponential function

$$\varepsilon_v^p = w(1 - e^{-d[x(\kappa) - x_0]}) \tag{6.9}$$

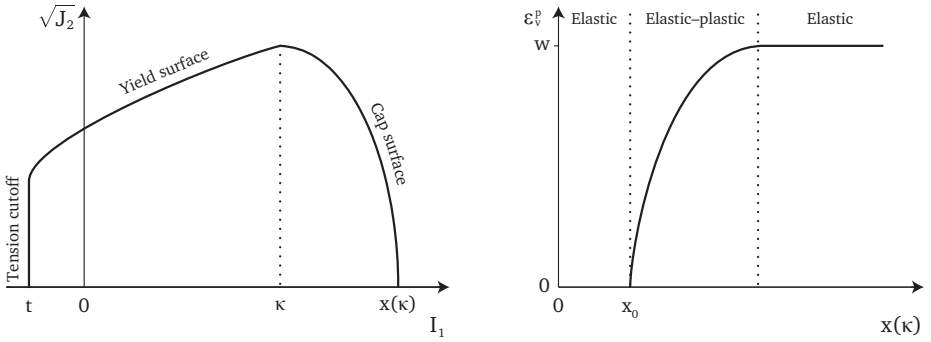


**Figure 6.17:** *Geologic Cap* model a) yield surfaces and b) cap hardening function.

| Variable | Description |
|---|---|
| `ro` | Initial density. [kg m$^{-3}$] |
| `k` | Initial bulk modulus. [Pa] |
| `g` | Initial shear modulus. [Pa] |
| `alpha` | Failure envelope parameter, $\alpha$. |
| `theta` | Failure envelope linear coefficient, $\theta$. |
| `gamma` | Failure envelope exponential coefficient, $\gamma$. |
| `beta` | Failure envelope exponent, $\beta$. |
| `r` | Cap surface axis ratio, $r$. |
| `d` | Hardening law exponent, $d$. |
| `w` | Hardening law coefficient, $w$. |
| `x0` | Hardening law exponent $x_0$. |
| `toff` | Tension cut-off, t ($< 0$). [Pa] |

**Table 6.8:** LS-DYNA variables for *Geologic Cap*.

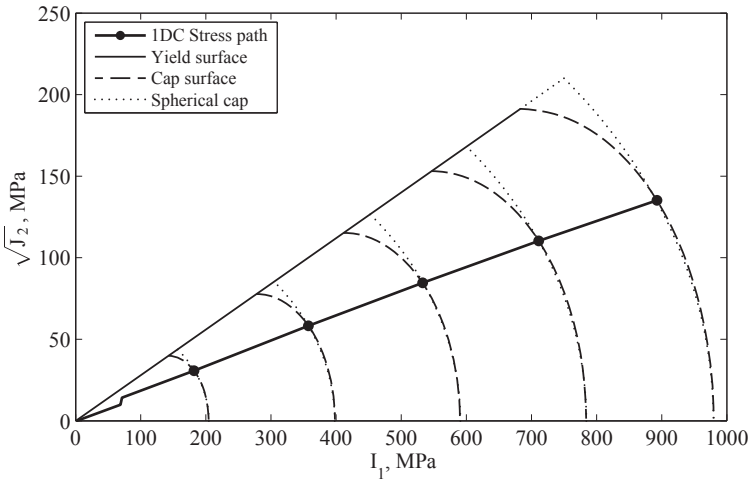


**Figure 6.18:** Development of the *Geologic Cap* cap surface during a one-dimensional compression test.

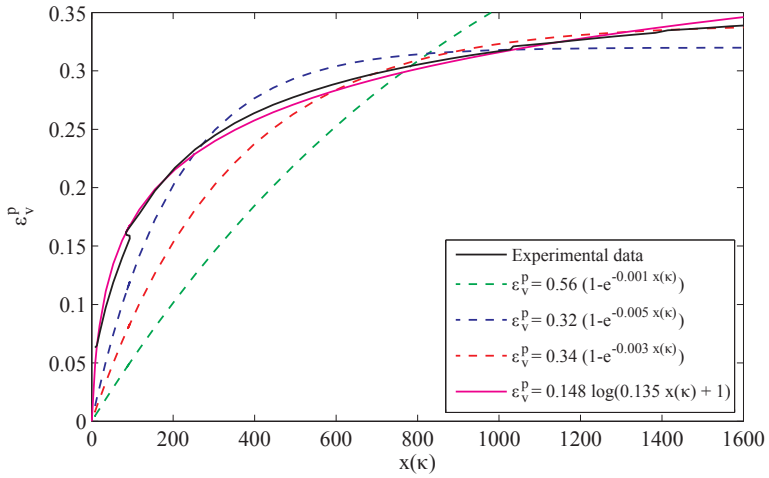


**Figure 6.19:** Attempts to fit the *Geologic Cap* hardening law to experimental data.

where $x_0$ is the elastic limit in the material and $w$ is the plastic strain at which all void spaces in the material are closed (Figure 6.17b). This exponential function is impossible to fit accurately to the experimental data in §6.2.1, as soils under one-dimensional compression follow a logarithmic relationship of the form $e = e_0 - \log \sigma'_v$ where $e$ is void ratio. Figure 6.19 shows possible exponential fits to the experimental data over the stress range experienced in the SHPB tests.

- The first fit (green dash) uses the value of $w$ in its strictest sense as the strain at which all voids are closed ($\varepsilon_v^p = 0.56$). This quickly deviates from the experimental data regardless of the value chosen for $d$.
- The second fit (blue dash) follows the experimental data as closely as possible throughout loading, but implies that no plastic strain occurs above $I_1 = 800\,\text{MPa}$: $w$ is set artificially low to allow the fit. The fit also deviates by approximately 50 MPa from the experimental data at low stresses, making it unsuitable for investigating both low- and high-stress regimes.
- The third fit (red dash) attempts to improved the fit at higher stresses, but causes increased stiffness at low stresses, so that it deviates from the experimental data by as much as 200 MPa.
- The final fit (magenta) shows an example of a logarithmic fit which would closely match the experimental data throughout.

#### Conclusion

No validation of the *Geologic Cap* model was carried out due to the known limitations of the hardening function, which could not be calibrated to the experimental data. *Schwer–Murray Cap* (`*MAT_145`) uses a similar exponential hardening function, and so both are unsuitable for modelling soils where a large amount of compaction is expected to occur.

### 6.5.5 Nested Surface

#### Calibration

*Hysteretic Soil* (`*MAT_79`) is a nested-surface model composed of up to ten elastic–perfectly-plastic surfaces, which allow the modelling of hysteretic soil behaviour. The yield surfaces are nested inside each other, and are engaged in turn as the shear stress increases, so that the material behaviour represents the combined effect of the active surfaces. The bulk and shear moduli are pressure sensitive,

| Variable | Description |
|---|---|
| `ro` | Initial density. [$\mathrm{kg\,m^{-3}}$] |
| `k0` | Initial bulk modulus. [Pa] |
| `p0` | Cut-off/datum pressure. [Pa] |
| `b` | Exponent for pressure-sensitive moduli. |
| `a0, a1, a2` | Yield function constants. |
| `df` | Damping factor. |
| `rp` | Reference pressure. [Pa] |
| `lcid` | Load curve id defining shear stress against shear strain. |
| `sfld` | Scale factor to apply to shear stress in `lcid`. |
| `dil_a` – `dil_d` | Dilation parameters A, B, C, D. |
| `gam1` – `gam5` | Shear strains $\gamma_1$–$\gamma_5$ (alternative to `lcid`). |
| `tau1` – `tau5` | Shear stresses $\tau_1$–$\tau_5$ (alternative to `lcid`). [Pa] |

**Table 6.9:** LS-DYNA variables for *Hysteretic Soil*.

and define the compaction response of the material. Dilatancy can also be incorporated. Definition of the model requires the variables in Table 6.9.

The pressure-dependent bulk modulus, $K$, is defined as

$$K(P) = K_0 \frac{(P - P_0)^b}{(P_r - P_0)^b}$$

where $P$ is pressure, $K_0$ is the initial bulk modulus, $P_r$ is the reference pressure and $P_0$ is the datum pressure. Assuming that $P_0$ is small enough to be neglected, the pressure in compression can be expressed as

$$P = \left[ -\frac{K_0}{P_r^b} \ln(V) \right]^{\frac{1}{(1-b)}}$$

where V is the relative volume.

Values for $K_0$, $P_r$ and $b$ were calculated by the method of least squares to fit the experimental data in §6.2.1, as shown in Figure 6.20. A fit over the full stress range produces a very poor result, with deviation from the experimental results of over 100 MPa. Another fit to the response below mean stresses of 100 MPa produces a good fit at these stresses, but quickly deviates at higher stresses.

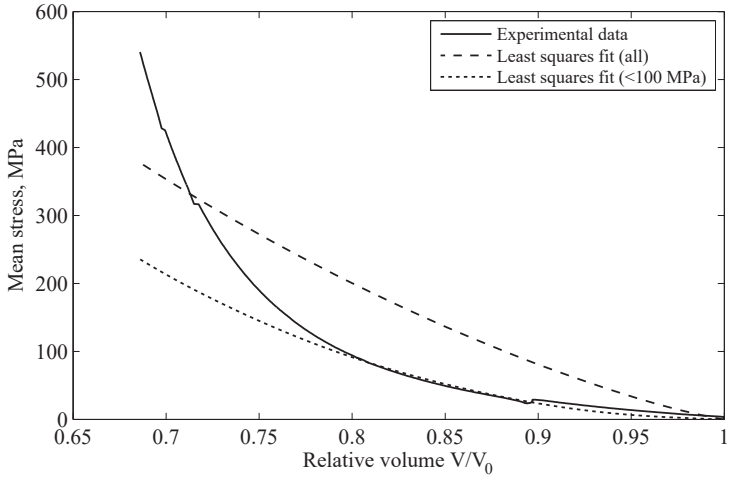


**Figure 6.20:** Attempts to calibrate *Hysteretic Soil* compressibility response to experimental data.

### Conclusion

As the compressibility of the sand cannot be accurately represented in *Hysteretic Soil* above 100 MPa, it is unsuitable for modelling the sand at the high stresses experienced in a SHPB test.

## 6.6 Recommendations for a high-pressure soil model

In each of the models considered above, the yield surface of the sand was successfully defined using a tabulated or quadratic input, but were not engaged due to the one-dimensional compression loading conditions. None of the models, however, could accurately simulate the compaction of the soil, due to either:

- the lack of a compaction mechanism;
- an exponential, rather than a logarithmic, compaction mechanism; or
- an inability to accurately model the lateral behaviour through the shear modulus or Poisson's ratio.

It is noted that models were validated using the experimental setup and results of the dry SHPB tests in Chapter 3, which showed greater variation than the improved experiments in Chapter 5. However, both *Soil and Foam* and *Pseudo-Tensor* returned results which were even less stiff than the quasi-static experi-

ments, and so the modelled results lie well outside the range of experimental error.

As a result of the poor compaction behaviour, none of the constitutive models included in LS-DYNA are suitable for modelling the behaviour of medium sand at high pressures, and so it is not currently possible to meaningfully explore the internal stress state of the SHPB sand specimens. To do so would require the development of a modified soil constitutive model for LS-DYNA, which would incorporate a compaction response based on the soil mechanics relationship $e = e_0 - \log \sigma_v$, and would allow the Poisson's ratio to be defined directly to control the lateral response.

*Pseudo-Tensor* came closest to modelling the compaction behaviour of the sand. However, there is growing scientific interest in the shear behaviour of soils at high strain rates (Martin et al. 2013, Barr et al. 2016), and so it would be advisable for any new model to be sufficiently robust to also model unconfined or partially-confined specimens. This could be achieved by modifying an existing cap model, such as *Geologic Cap*, to remove concrete-specific components and introduce soil mechanics parameters. The main changes would be to:

- provide accurate predictions of compaction behaviour using the relationship $e = e_0 - \log \sigma_v$, using a piecewise function to account for the bi-linear NCL behaviour observed in Chapter 3;
- allow Poisson's ratio to be defined to control lateral response during compaction;
- enable modelling of partially-saturated soils by introducing geotechnical parameters to identify full saturation and the loading of pore water as observed in Chapter 5, *e.g.* $w$, $\rho_s$ and $K_{\text{water}}$; and
- enable more general definitions of cap shape, so that models can respond to new data about the high-pressure behaviour of soils.

*Geologic Cap* currently uses an elastic–perfectly-plastic yield surface, which may also need to be modified depending on the development of research into the high-pressure shear response of soils.

## 6.7 Summary

This chapter demonstrated the ability of the mac$^{2T}$ apparatus to generate high-pressure calibration data for soil models. For the first time in the literature the

yield surface of a soil was characterised to pressures of over 400 MPa. When combined with high-pressure compression data, this eliminates the uncertainty associated with the extrapolation of low-pressure geotechnical tests in the calibration of numerical models.

The ability of LS-DYNA's 'soil' constitutive models to accurately represent soil behaviour in SHPB experiments was assessed through comparison with experimental data. It was found that none could accurately simulate the compaction behaviour of the sand, and so were unsuitable for modelling the behaviour of soils at high pressures. As a result it was not possible to analyse the internal stress state of the experimental SHPB sand specimens, and recommendations were made on the development of an alternative high-pressure soil model.

Chapter 7

# Summary and conclusions

## 7.1 Summary

This thesis aimed to compare the high-pressure, quasi-static compaction behaviour of sandy soils, and to investigate how this behaviour was affected by changes in strain rate and moisture content.

High-pressure quasi-static compression tests in mac$^{2T}$ were used to investigate the behaviour of three sands, quantifying the compaction behaviour to axial stresses of 800 MPa. Decreased uniformity and increased mean particle size were found to decrease the stiffness, and hence the protective capability, of the soil. High-strain-rate SHPB experiments were carried out on the same soils, and measurements of radial stress were used to show that an apparent increase in stiffness at high strain rates was likely due to the effects of radial inertia.

Potential sources of error were identified in the SHPB stress measurements, and resulted in the implementation of a dispersion-correction algorithm, which greatly improved the measurement of axial stresses. An analysis of the electromagnetic activity around the specimen isolated the contribution of the accelerating pressure bars.

Quasi-static experiments were used to investigate the effect of moisture content on soil stiffness at high pressures, and SHPB experiments at the same moisture contents were used to consider the effect of strain rate on the quasi-static behaviour. Recovery SHPB experiments were designed to enable reliable post-test particle size analyses to be performed. A range of moisture contents were tested to allow a comparison of specimens which remained partially saturated throughout the experiment and specimens which reached full saturation.

The mac$^{2T}$ apparatus was used to produce the first high-pressure yield surface for a soil in the literature, using reduced triaxial compression experiments to

define the surface to a mean stress of 400 MPa. The high-pressure compression and yield strength data collected for the medium sand were used to calibrate soil models in LS-DYNA, which were validated using the SHPB experiments. Recommendations were made on the development of a new constitutive model which can more accurately represent the behaviour of soils at high pressures.

## 7.2 Conclusions

### 7.2.1 Quasi-static compression

- Following quasi-static compression to 800 MPa all three soils could be removed from the test box as a solid block of sandstone-like material, with significant cohesion. A block of medium sand could sustain a uniaxial stress of 3.2 MPa before failure, without additional lateral support.
- The well-graded sandy loam behaved less stiffly than the more uniform medium and coarse sands, as the large range of particle sizes aided compaction. The coarse sand behaved less stiffly than the medium sand, as the probability of particle breakage is increased for soils with larger particles. This replicated behaviour commonly observed at lower stresses.
- Each soil followed an approximately bi-linear normal compression line when plotted in $e$–$\log \sigma_x$ space, with an intersection at a void ratio of approximately 0.3 in each case. At this point the compressibility index of the three soils reduced to similar values.
- The unloading bulk modulus of all three soils increased with peak stress.

### 7.2.2 Strain rate effects

For SHPB experiments on three soils with peak strain rates of 5200 $s^{-1}$:

- Coarse sand, medium sand and sandy loam all behaved more stiffly at $10^3\,s^{-1}$ than at $10^{-3}\,s^{-1}$ when axial stresses were considered, but this apparent strain rate effect disappeared when considering mean stresses.
- At high strain rates the measured radial stresses were much lower, leading to an apparent decrease in the Poisson's ratio of the soils. This change in stress distribution showed evidence of radial inertial confinement in

the specimen at high strain rates, and indicates that the increased axial stiffness is not a true strain-rate effect.

- The three soils exhibited similar relative stiffnesses as during quasi-static testing, although inertial effects dominated the behaviour at lower stresses.
- The fracture of sand particles at high strain rates was ruled out as a significant source of electromagnetic interference in the SHPB radial stress measurements: this was instead attributed to the movement of magnetised pressure bars.

For SHPB experiments on medium sand with peak strain rates of $3500\,s^{-1}$:

- The calculation of mean axial stress in the specimens was greatly improved through the implementation of a dispersion-correction algorithm, which corrected the phase angle and amplitude of frequency components.
- The medium sand displayed little increase in stiffness at $10^{3}\,s^{-1}$ compared to $10^{-3}\,s^{-1}$, except during the initial part of the SHPB experiments where inertial forces dominate the response.

### 7.2.3 Moisture effects

Under quasi-static loading, between moisture contents of 0.0% and 5.0%:

- The stiffness of the medium sand reduced as the moisture content increased, and was attributed to the lubricating effect of the water during particle rearrangement.
- In tests at 5.0% moisture content the specimens reached full saturation at high pressures. As loading in the quasi-static experiments occurred under drained conditions, this resulted in water being expelled from the specimen.

For SHPB experiments with peak strain rates of $5200\,s^{-1}$, between moisture contents of 0.0% and 5.0%:

- There was no significant change in the behaviour of the sand with changing moisture content.
- The difference in quasi-static and high-strain-rate behaviour resulted in an increasing strain rate effect on stiffness with increasing moisture content, even when considering mean stresses.

For SHPB experiments with peak strain rates of $3500\,s^{-1}$, between moisture contents of 0.0% and 15.0%:

- At moisture contents up to 7.5%, specimens remained partially-saturated throughout the experiment, and increases in moisture content led to a decrease in the stiffness of the sand and a small increase in particle breakage.
- This decrease in stiffness was similar to that observed in the quasi-static experiments, and so there appeared to be little dependence on strain rate between the SHPB and quasi-static tests.
- At moisture contents above 7.5% the specimens reached full saturation during the experiment. The pre-saturation stiffness was similar to the 7.5% specimens, and increased to the stiffness of water on reaching saturation, indicating that further volume changes were dominated by the compression of pore water.
- The loading of pore water indicates that the strain rate was sufficiently high that the experiments approximated undrained conditions.
- Full saturation occurred at lower dry densities as moisture content was increased, leading to a decrease in particle breakage.
- At low moisture contents full saturation could occur when the stiffness of the soil is greater than that of the pore water, and in these cases the soil would follow the regular soil compaction curve rather than the stiffness of water.

### 7.2.4 Numerical modelling

- The mac$^{2T}$ apparatus was successfully used to perform high-pressure reduced triaxial compression experiments, defining the high-pressure yield surface for dry medium sand to a mean stress of 400 MPa.
- The data produced in mac$^{2T}$ was easily converted into the compressibility curves and yield surfaces required to calibrate constitutive models, along with other necessary elastic constants.
- The ability of mac$^{2T}$ to provide high-pressure characterisation of soils in both compression and shear therefore removes the need to rely on large extrapolations from standard geotechnical tests.

- The existing soil models in LS-DYNA model the compaction of soils poorly due to assumptions of exponential compaction mechanisms and poor control over lateral behaviour.

- Modelling of soils at high pressures could be achieved by modifying the *Geologic Cap* model to incorporate a logarithmic compaction behaviour, pore water parameters and increased control over the shape of the cap surface.

## 7.3 Contributions to the FPE research programme

This research forms part of the Dstl-sponsored and QinetiQ-led Force Protection Engineering (FPE) research programme, which aims to improve the understanding of soil behaviour in defensive structures (see Chapter 1). This thesis investigated the behaviour of sand at high pressures, and how this behaviour is affected by strain rate and moisture content: these results have been incorporated into the Military Engineering Volume covering force protection, and will guide the decisions made by military engineers.

One of the goals of the FPE programme is to develop robust models of material behaviour, so that solutions can be designed to defend against new threats quickly and cost-effectively. The quasi-static compression and yield data in this work have been used by QinetiQ's modellers to develop a constitutive model for soils, which has also been validated using simulations of the split Hopkinson pressure bar experiments.

## 7.4 Future research

The results above have identified several areas which would benefit from additional research, which would lead to an improved understanding of the mechanisms behind soil behaviour at high pressures and strain rates.

### 7.4.1 High-pressure compression

- The three sandy soils investigated in this thesis were used to demonstrate general trends relating to particle size distribution. Further experiments are required to assess whether this behaviour extends to other common soil types, such as silt and clay.

- Although all three soils tested in Chapter 2 were initially cohesionless, they developed significant cohesion during quasi-static compression to 800 MPa. Potential locking of soil particles could be identified using x-ray tomography (XRT), and the effect of peak stress on cohesion investigated.
- In all three soils the two linear NCLs intersected at a void ratio of approximately 0.3, after which the compressibility indices fell to similar values. This may indicate that the soils achieve similar PSDs at this point, which could be assessed through particle size analysis of specimens compressed to the same void ratio.
- Particle size analysis could also be used to investigate the strain-rate dependence of particle breakage by loading specimens quasi-statically to the stresses achieved in the SHPB experiments.
- If particle breakage was found not to be strain-rate dependent, the hypothesis in Chapter 5 that significant particle breakage only occurs up to the point of saturation could be investigated under quasi-static loading. If the hypothesis is correct, it may be possible to use particle size analyses forensically, and infer the peak stress experienced in a blast or impact event using only the particle breakage and knowledge of the initial moisture content.

### 7.4.2 High-pressure shear

- The high-pressure yield surface presented in this thesis is the first of its kind in the open literature, and so some further work is required to refine the methodology to ensure a critical state is reached.
- The evolution of similar PSDs at high pressures could indicate that soils with initially different PSDs have similar yield surfaces at high pressures: this could be assessed using RTC experiments on the three soils tested in Chapter 3.
- Similarly, the effects of moisture content on shear behaviour at these pressures is unknown, and could be investigated through RTC experiments.
- It was noted in Chapter 2 that assessing the dynamic shear behaviour of soils in blast or impact events would require a departure from the CTC method to properly consider the effects of inertia. This work has already begun in the development of a SHPB with partial lateral confinement (Barr et al. 2016). This apparatus permits lateral restraint to

develop throughout the axial loading, enabling the shear behaviour to be characterised under conditions which are more representative of dynamic events.

### 7.4.3 Inertial effects

- The SHPB experiments have shown that radial inertial effects have a significant influence on the behaviour of soil at high strain rates. Study of this effect using FE modelling was not possible due to the shortcomings of the available soil constitutive models. The development of an updated soil model, as described in Chapter 6, would enable this work.
- All measurements taken in the SHPB experiments are taken at some distance from the specimen, and have to be used to infer a mean response. An x-ray method could be used to assess the spatial variation of density during SHPB tests on sand, and could be used in conjunction with the numerical study above in quantifying radial effects.
- Closed-form solutions exist for the contribution of radial inertia in linear-elastic SHPB specimens (Forrestal et al. 2007). With some simplifying assumptions it may be possible to develop similar solutions for the dynamic compaction of soils, which could be used to provide a first estimate of the radial inertia expected for a given specimen geometry.

### 7.4.4 Dispersion correction

- The dispersion correction algorithm implemented in Chapter 4 resulted in a significant improvement in the interpretation of the SHPB strain gauge signals, although the correction bandwidth was limited by the inability to correct dispersion in higher modes. When multiple modes are propagating the proportion of energy travelling in each mode must be known in order to apply a correction. Work is underway to investigate these higher modes using FE analyses of wave propagation in cylindrical bars (Rigby, Barr and Clayton 2016).

# Bibliography

An, J., Tuan, C. Y., Cheeseman, B. and Gazonas, G. (2011), 'Simulation of soil behavior under blast loading', *International Journal of Geomechanics* **11**(4), 323–334.

Atkinson, J. H. and Bransby, P. (1978), *Mechanics of Soils*, McGraw Hill, Maidenhead.

Bancroft, D. (1941), 'The velocity of longitudinal waves in cylindrical bars', *Physical Review* **59**, 588–593.

Barr, A. D., Clarke, S. D., Petkovski, M., Tyas, A., Rigby, S. E., Warren, J. and Kerr, S. (2016), 'Effects of strain rate and moisture content on the behaviour of sand under one-dimensional compression', *Experimental Mechanics* **56**(9), 1625–1639.

Barr, A. D., Clarke, S. D., Rigby, S. E., Tyas, A. and Warren, J. (2016), 'Design of a split Hopkinson pressure bar with partial lateral confinement', *Measurement Science and Technology* **27**(12).

Been, K. and Jefferies, M. G. (1985), 'A state parameter for sands', *Géotechnique* **35**(2), 99–112.

Ben-Nun, O. and Einav, I. (2010), 'The role of self-organization during confined comminution of granular materials', *Philisophical Transactions of the Royal Society of London, Series A* **368**, 231–247.

Bischoff, P. and Perry, S. (1991), 'Compressive behaviour of concrete at high strain rates', *Materials and structures* **24**(6), 425–450.

Bjerrum, L. (1967), 'Engineering geology of Norwegian normally-consolidated marine clays as related to settlements of buildings', *Géotechnique* **17**(2), 83–118.

Bragov, A. M., Lomunov, A. K., Sergeichev, I. V., Tsembelis, K. and Proud, W. G. (2008), 'Determination of physicomechanical properties of soft soils from medium to high strain rates', *International Journal of Impact Engineering* **35**.

BSI (1990*a*), 'BS 1377-2:1990. Methods of test for soils for civil engineering purposes. Part 2. Classification tests'.

BSI (1990*b*), 'BS 1377-4:1990. Methods of test for soils for civil engineering purposes. Part 4. Compaction-related tests'.

BSI (1990*c*), 'BS 1377-5:1990. Methods of test for soils for civil engineering purposes. Part 5. Compressibility, permeability and durability tests'.

Charlie, W. A., Ross, C. A. and Pierce, S. J. (1990), 'Split-Hopkinson pressure bar testing of unsaturated sand', *Geotechnical Testing Journal* **13**(4), 291–300.

Chen, W. and Ravichandran, G. (1997), 'Dynamic compressive failure of a glass ceramic under lateral confinement', *Journal of the Mechanics and Physics of Solids* **45**(8), 1303–1328.

Chree, C. (1889), 'The equations of an isotropic elastic solid in polar and cylindrical co-ordinates their solution and application', *Transactions of the Cambridge Philosophical Society* **14**, 250.

Church, P., Cornish, R., Cullis, I., Gould, P. and Lewtas, I. (2014), 'Using the split Hopkinson pressure bar to validate material models', *Philosophical Transactions of the Royal Society A: Mathematical, Physical and Engineering Sciences* **372**(2023).

Clarke, S. D., Fay, S. D., Warren, J. A., Tyas, A., Rigby, S. E., Reay, J. J., Livesy, R. and Elgy, I. (2015), 'Geotechnical causes for variations in output measured from shallow buried charges', *International Journal of Impact Engineering* **86**, 274–283.

Cress, G., Brady, B. and Rowell, G. (1987), 'Sources of electromagnetic radiation from fracture of rock samples in the laboratory', *Geophysical Research Letters* **14**(4), 331–334.

Cundall, P. A. and Strack, O. D. (1979), 'A discrete numerical model for granular assemblies', *Géotechnique* **29**(1), 47–65.

Davies, E. D. and Hunter, S. C. (1963), 'The dynamic compression testing of solids by the method of the split-Hopkinson pressure bar', *Journal of the Mechanics and Physics of Solids* **2**, 155–179.

Davies, R. M. (1948), 'A critical study of the Hopkinson pressure bar', *Philisophical Transactions of the Royal Society of London, Series A* **240**, 375–457.

Fang, Q., Zhang, J., Chen, L., Liu, J., Fan, J. and Zhang, Y. (2014), 'An algorithm for the grain-level modelling of a dry sand particulate system', *Modelling and Simulation in Materials Science and Engineering* **22**(5).

Farr, J. V. (1986), Loading rate effects on the one-dimensional compressibiliy of four partially saturated soils, Technical report, US Army Engineer Waterways Experiment Station.

Farr, J. V. (1990), 'One-dimensional loading-rate effects', *Journal of Geotechnical Engineering* **116**(1), 119–135.

Felice, C., Brown, J., Gaffney, E. and Olsen, J. (1987), An investigation into the high strain-rate behavior of compacted sand using the split Hopkinson pressure bar technique, *in* 'Proceedings of the 2nd Symposium on the Interaction of Non-nuclear Munitions with Structures', pp. 391–396.

Felice, C. W. (1986), The response of soil to impulse loads using the split-Hopkinson pressure bar technique, Technical report, DTIC Document.

Feynman, R. P., Leighton, R. B. and Sands, M. (1964), *The Feynman Lectures on Physics*, Vol. 2.

Fiserova, D. (2006), 'Numerical analysis of buried mine explosions with emphasis on effect of soil properties on loading'.

Follansbee, P. and Frantz, C. (1983), 'Wave propagation in the split Hopkinson pressure bar', *Journal of Engineering Materials and Technology* **105**(1), 61–66.

Forrestal, M., Wright, T. and Chen, W. (2007), 'The effect of radial inertia on brittle samples during the split Hopkinson pressure bar test', *International Journal of Impact Engineering* **34**(3), 405–411.

Fraser, D. A. (1986), *The physics of semiconductor devices*, Clarendon Press.

Frew, D., Akers, S., Chen, W. and Green, M. L. (2010), 'Development of a dynamic triaxial Kolsky bar', *Measurement Science and Technology* **21**(10).

Frew, D. J., Forrestal, M. J. and Chen, W. (2005), 'Pulse shaping techniques for testing elastic-plastic materials with a split Hopkinson pressure bar', *Experimental Mechanics* **45**(2), 186–195.

Fukumoto, T. (1992), 'Particle breakage characteristics of granular soils', *Soils and Foundations* **32**(1), 26–40.

Gorham, D. A. (1983), 'A numerical method for the correction of dispersion in pressure bar signals', *Journal of Physics E: Scientific Instruments* **16**, 477–479.

Gray III, G. T. (2000), *Classic split-Hopkinson pressure bar testing*, ASM International.

Grujicic, M., Pandurangan, B., Qiao, R., Cheeseman, B., Roy, W., Skaggs, R. and Gupta, R. (2008), 'Parameterization of the porous-material model for sand with different levels of water saturation', *Soil Dynamics and Earthquake Engineering* **28**(1), 20–35.

Hagerty, M. M., Hite, D. R., Ullrich, C. R. and Hagerty, D. J. (1993), 'One-dimensional high-pressure compression of granular material', *Journal of Geotechnical Engineering* **119**(1), 1–18.

Hallquist, J. O. (2007), LS-DYNA keyword user's manual, Technical report.

Heymsfield, E., Fasanella, E. L., Hardy, R. C. and Boitnott, R. L. (2010), 'Assessment of soil modeling capability for Orion contingency land landing', *Journal of Aerospace Engineering* **25**(1), 125–131.

Hopkinson, B. (1914), 'A method of measuring the pressure produced in the detonation of high explosives or by the impact of bullets', *Philosophical Transactions of the Royal Society of London. Series A, Containing Papers of a Mathematical or Physical Character* pp. 437–456.

Huang, J., Xu, S. and Hu, S. (2013), 'Effects of grain size and gradation on the dynamic responses of quartz sands', *International Journal of Impact Engineering* **59**, 1–10.

ISO (2002), '14688-1: 2002: Geotechnical investigation and testing – Identification and classification of soil – Part 1 Identification and description', *British Standards Institution* .

Jayasinghe, L. B., Thambiratnam, D. P., Perera, N. and Jayasooriya, J. H. A. R. (2013), 'Computer simulation of underground blast response of pile in saturated soil', *Computers and Structures* **120**(0), 86–95.

Kabir, M. E., Martin, B. E. and Chen, W. (2010), Compressive behavior of fine sand, Technical report, Sandia National Laboratories.

Kolsky, H. (1949), 'An investigation of the mechanical properties of materials at very high rates of loading', *Proceedings of the Physical Society, Section B* **62**, 676–700.

Kolsky, H. (1963), *Stress waves in solids*, Dover Publications, New York.

Laine, L. and Sandvik, A. (2001), Derivation of mechanical properties for sand, *in* '4th Asia-Pacific Conference on Shock and Impact Loads on Structures'.

LSTC (2012), LS-DYNA keyword users' manual, Technical report.

Luo, H., Cooper, W. and Lu, H. (2014), 'Effects of particle size and moisture on the compressive behavior of dense Eglin sand under confinement at high strain rates', *International Journal of Impact Engineering* **65**, 40–55.

Luo, H., Lu, H., Cooper, W. L. and Komanduri, R. (2011), 'Effect of mass density on the compressive behavior of dry sand under confinement at high strain rates', *Experimental Mechanics* **51**, 1499–1510.

Martin, B. E., Chen, W., Song, B. and Akers, S. A. (2009), 'Moisture effects on the high strain-rate behavior of sand', *Mechanics of Materials* **41**, 786–798.

Martin, B., Kabir, M. E. and Chen, W. (2013), 'Undrained high-pressure and high strain-rate response of dry sand under triaxial loading', *International Journal of Impact Engineering* .

McDowell, G. (2002), 'On the yielding and plastic compression of sand', *Soils and foundations* **42**(1), 139–145.

McDowell, G., Bolton, M. and Robertson, D. (1996), 'The fractal crushing of granular materials', *Journal of the Mechanics and Physics of Solids* **44**(12), 2079–2102.

McDowell, G. and de Bono, J. P. (2013), 'On the micromechanics of one-dimensional normal compression', *Géotechnique* **63**(11), 895–908.

Meitzler, A. H. (1956), 'Effect of strain rate on the behavior of iso-elastic wire strain gauges', *The Review of Scientific Instruments* **27**(56).

Neal, W. D., Appleby-Thomas, G. J. and Collins, G. S. (2014), 'Meso-scopic deformation in brittle granular materials', *Journal of Physics: Conference Series* **500**(11).

Nemat-Nasser, S., Isaacs, J. B. and Starrett, J. E. (1991), 'Hopkinson techniques for dynamic recovery experiments', *Proceedings of the Royal Society of London, Section A* **436**, 371–391.

O'Sullivan, C. (2014), Advancing geomechanics using DEM, *in* 'Geomechnanics from Micro to Macro', Taylor and Francis Group, London.

Perry, J., Braithwaite, C., Taylor, N., Pullen, A. and Jardine, A. (2016), 'The significance of grain morphology, moisture, and strain rate on the rapid compaction of silica sands', *Applied Physics Letters* **109**(17), 174103.

Petkovski, M., Crouch, R. S. and Waldron, P. (2006), 'Apparatus for testing concrete under multiaxial compression at elevated temperature (mac2t)', *Experimental Mechanics* **46**, 387–398.

Pochhammer, L. (1876), 'Ueber die fortpflanzungsgeschwindigkeiten kleiner schwingungen in einem unbegrenzten isotropen kreiscylinder', *Journal für die reine und angewandte Mathematik* **81**, 324–336.

Powrie, W. (2013), *Soil mechanics: concepts and applications*, CRC Press.

Rigby, S. E., Barr, A. D. and Clayton, M. (2016), 'A numerical study of higher mode Pochhammer-Chree dispersion', *In preparation for the International Journal of Impact Engineering* .

Rigby, S. and Tyas, A. (2012), Experiments on the mechanical properties of Leighton Buzzard and sandy loam soils at static and dynamic strain rates, Technical report, prepared for Dstl Porton Down.

Ross, C. A., Nash, P. T. and Friesenhahn, G. J. (1986), Pressure waves in solids using a split Hopkinson pressure bar, Technical Report ESL-TR-86-29, Air Force Engineering and Services Centre.

Song, B. and Chen, W. (2004), 'Dynamic stress equilibration in split Hopkinson pressure bar tests on soft materials', *Experimental Mechanics* **44**(3).

Song, B., Chen, W. and Luk, V. (2009), 'Impact compressive response of dry sand', *Mechanics of Materials* **41**, 777–785.

Stephens, R. C. (1970), *Strength of materials: theory and examples*, Hodder Arnold.

Tyas, A. and Pope, D. J. (2005), 'Full correction of first-mode Pochammer-Chree dispersion effects in experimental pressure bar signals', *Measurement Science and Technology* **16**, 642–652.

Tyas, A. and Rigby, S. (2012), Experiments on the mechanical properties of Leighton Buzzard and sandy loam soils at static and dynamic strain rates, Technical report, QinetiQ.

Tyas, A. and Watson, A. J. (2000), 'Experimental evidence of Pochammer-Chree strain variations in elastic cylinders', *Experimental Mechanics* **40**(3).

Tyas, A. and Watson, A. J. (2001), 'An investigation of frequency domain dispersion correction of pressure bar signals', *International Journal of Impact Engineering* **25**, 87–101.

Veyera, G. E. (1994), Uniaxial stress-strain behavior of unsaturated soils at high strain rates, Technical report, Wright Laboratory Flight Dynamics Directorate, AFMC.

Vigness, I. (1956), 'Magnetostrictive electricity in strain gauges', *The Review of Scientific Instruments* **27**(12).

Wang, J. (2001), Simulation of landmine explosion using LS-DYNA 3D software: benchmark work of simulation of explosion in soil and air, Technical report, DTIC Document.

Warren, J., Kerr, S., Tyas, A., Clarke, S. D., Petkovski, M., Jardine, A., Church, P., Gould, P. and Williams, A. (2013), 'Briefing: UK Ministry of Defence Force Protection Engineering Programme', *Proceedings of the ICE - Engineering and Computational Mechanics* **166**(3), 119–123.

Wood, D. M. (1990), *Soil behaviour and critical state soil mechanics*, Cambridge University Press.

Yamamuro, J. A., Bopp, P. A. and Lade, P. V. (1996), 'One-dimensional compression of sands at high pressures', *Journal of Geotechnical Engineering* **122**(2), 147–154.

Young, C. and Powell, C. (1979), Lateral inertia effects on rock failure in split-Hopkinson-bar experiments, *in* '20th US Symposium on Rock Mechanics (US-RMS)', American Rock Mechanics Association.

Appendix A

# Analysing SHPB data with dispersion correction in MATLAB

## A.1 Introduction

Section 4.2 introduced a MATLAB script (`dispersion.m`) for first-mode dispersion correction based on the work of Tyas and Pope (2005). This script and its dependents are presented and annotated here along with `shpb.m`, which demonstrates how the dispersion correction was implemented in the analysis of the results in Chapter 5.

## A.2 dispersion.m

`dispersion.m` automates the application of phase angle and amplitude corrections to pressure bar signals, manipulating individual frequency components to correct for the effects of dispersion over a defined propagation length. Further information on the theory and MATLAB implementation of these corrections is provided in § 4.2.

```
% dispersion() - First-mode dispersion correction of a finite
% arbitrary signal in a cylindrical bar
%
%
% OPERATION:
% - Finds FFT of the signal
% - Corrects phase velocity and amplitude of each frequency
%   using method described by Tyas & Pope (2005)
% - Reconstructs signal using IFFT
% - (Frequencies above fa/c0 = 0.2619 stripped (d/L = 0.6)
%   due to limitations of M1 correction)
%
% INPUTS:
% x         Zero-padded strain signal in time domain
%           (1xN numeric)
% fs        Sampling frequency, Hz
% a         Bar radius, m
% c0        One-dimensional wave velocity of the bar, m/s
% E         Young's modulus of the bar, GPa
% z         Distance to correct over, m
%           (+ve in direction of propagation)
%
% OUTPUTS:
% xStrain   Dispersion-corrected strain signal
% xStress   Dispersion-corrected stress signal, MPa


function [xStrain xStress] = dispersion(x,fs,a,c0,E,z)

    % Input signal
    N = length(x); % Number of elements in signal
    dt = 1/fs; % Time step, s
    t = 0:dt:dt*(N-1); % Time base, s
    f = (0:N-1)*(fs/N); % FFT frequencies, Hz
    fMax = 0.2619*c0/a; % Max correctable frequency due ...
       to factor M1 limitations, Hz
```

```
% FFT the signal
X = fft(x);
XStrain = X; % Create a copy for strain correction
XStress = X; % Create a copy for stress correction

% Phase shift, adjust magnitude of frequency components
numberOfBins = length(X);
DCbin = 1; % DC frequency bin

if(mod(numberOfBins,2)==0)
    % N is even
    positiveBins = 2:numberOfBins/2; % Positive ...
        frequency bins
    nyquistBin = numberOfBins/2+1; % Nyquist ...
        frequency bin
    binsToEdit = [positiveBins nyquistBin]; % Total ...
        bins to edit individually
    negativeBins = numberOfBins/2+2:numberOfBins; % ...
        Negative frequency bins (populated through ...
        conjugation of positive bins)
else
    % N is odd
    positiveBins = 2:(numberOfBins+1)/2; % Positive ...
        frequency bins
    binsToEdit = positiveBins; % Total bins to edit ...
        individually
    negativeBins = (numberOfBins+1)/2+1:numberOfBins; ...
        % Negative frequency bins (populated through ...
        conjugation of positive bins)
end

for b = binsToEdit
    if f(b) <= fMax
        % Edit phase and amplitude of positive bins
        [angleMod M1 M2] = ...
            dispersionFactors(f(b),a,c0,z); % Find ...
            phase shift and factors M1 and M2 for ...
            current freq
        XStrain(b) = M1*abs(X(b)) * exp(1i * ...
            (angle(X(b))-angleMod)); % Apply phase ...
            shift and factors M1 to obtain corrected ...
            strain
        XStress(b) = M1*M2*abs(X(b)) * exp(1i * ...
            (angle(X(b))-angleMod)); % Apply phase ...
            shift and factors M1 and M2 to obtain ...
            corrected stress(/E)
    else
        % Above fMax zero X data (apply perfect ...
            low-pass filter)
```

```
            XStrain(b) = 0;
            XStress(b) = 0;
        end
    end

    XStrain(negativeBins) = ...
        conj(XStrain(positiveBins(end:-1:1))); % Correct ...
        negative bins by taking complex conjugate of ...
        positive bins
    XStress(negativeBins) = ...
        conj(XStress(positiveBins(end:-1:1))); % Correct ...
        negative bins by taking complex conjugate of ...
        positive bins

    % Convert the corrected frequency components back ...
        into the time domain
    xStrain = ifft(XStrain); % Corrected strain
    xStress = ifft(XStress)*E*1000; % Corrected stress, MPa

end

% dispersionFactors() - Calculate corrections to amplitude
% and phase angle to account for dispersion at a particular
% frequency
%
% REQUIRES:
% <dataTable>  A .mat file containing pre-calculated vectors
%              for a particular Poisson's ratio
%              - normFreqs: normalised frequencies (f*a/c0)
%              - vRatios: normalised velocities (c/c0)
%              - M1: amplitude factor M1
%              - M2: normalised amplitude factor M2 (M2/E)
%
% INPUTS:
% f            Frequency, Hz
% a            Bar radius, m
% c0           One-dimensional wave velocity of the bar, m/s
% z            Distance to apply correction over, m
%
% OUTPUTS:
% angleMod  Phase angle correction, rad
% M1        Correction for variation in response across bar
%           cross-section
% M2        Correction for variation in ratio of axial stress
%           and axial strain (dynamic Young's modulus)

function [angleMod M1 M2] = dispersionFactors(f,a,c0,z)
    load('PhaseVelocity_PR29.mat'); % File containing ...
        phase velocity data
```

```
    normFreq = f*a/c0; % Normalised frequency

    % Find change in phase angle
    phaseVelocity = ...
        interp1(normFreqs,vRatios,normFreq)*c0; % ...
        Interpolated phase velocity value
    angleMod = 2 * pi * f * z / phaseVelocity; % Change ...
        in phase angle at normFreq

    % Find amplitude factors M1 and M2
    M1 = interp1(normFreqs,M1,normFreq); % Interpolated ...
        value of M1 at normFreq
    M2 = interp1(normFreqs,M2,normFreq); % Interpolated ...
        value of M2/E at normFreq
end
```

## A.3 `shpb.m`

`shpb.m` processes SHPB strain gauge data to find dispersion-corrected specimen stresses and strains, including radial stresses measured on the surface of a stiff confining ring:

a) Reads oscilloscope data from SHPB and confining ring strain gauges.

b) Converts voltage signals into pressure bar strains, and identifies the incident, reflected and transmitted waves.

c) Uses `dispersion.m` to calculate dispersion-corrected stresses and strains for each wave.

d) Calculates the axial stresses and strains in the specimen using the incident, reflected and transmitted waves.

e) Calculates the radial stress in the specimen from the circumferential strain in the ring using thick-walled pipe theory.

f) Calculates the specimen density and dry density.

g) Saves the data to an m-file.

```
% Processes SHPB strain gauge data with dispersion correction
%
%
% REQUIRES:
% dispersion.m  Implementation of Tyas & Pope (2005)
%               'Full correction of first-mode Pochhammer
%               Chree dispersion effects in experimental
%               pressure bar signals'
%
% INPUTS:
% rawFile       Path to csv file containing oscilloscope data
%               Columns: Time, Ch1, Ch2, Ch3, Ch4
%               (string)
% sampleData    Length (mm), mass (g) and dry mass (g) data
%               for the sample
%               (cell array) {initialLength, mass, dryMass}
%
% OUTPUT:
% <fileName>    A .mat file containing the processed data.
```

```
function shpb(rawFile, sampleData)

    % ------------------------------------------------- %
    %                     VARIABLES                     %
    % Sample
    sample.InitialLength = sampleData{1};
    sample.Mass = sampleData{2};
    sample.DryMass = sampleData{3};

    % Incident bar
    inBar.Density = 7850; % Bar density, kg/m^3
    inBar.Diameter = 25; % Bar diameter, mm
    inBar.WaveSpeed = 5000; % Bar wave speed, m/s
    inBar.GaugeChannel = 1; % Input bar oscilloscope channel
    inBar.GaugeFactor = 100; % Input bar gauge factor
    inBar.GaugeAmp = 1;  % Input bar signal amplification
    inBar.GaugeVoltage = 5; % Input bar signal voltage, V
    inBar.GaugeOffset = 1000; % Distance from strain ...
        gauge to sample face, mm

    % Transmitter bar
    outBar.Density = 7850; % Bar density, kg/m^3
    outBar.Diameter = 25; % Bar diameter, mm
    outBar.WaveSpeed = 5000; % Bar wave speed, m/s
    outBar.GaugeChannel = 2; % Output bar oscilloscope ...
        channel
    outBar.GaugeFactor = 100; % Output bar gauge factor
    outBar.GaugeAmp = 1;  % Output bar signal amplification
    outBar.GaugeVoltage = 5; % Output bar signal voltage, V
    outBar.GaugeOffset = 500; % Distance from strain ...
        gauge to sample face, mm

    % Confining ring
    ring.OutsideDiameter = 35; % Outside diameter, mm
    ring.InsideDiameter = 25; % Inside diameter, mm
    ring.Length = 5; % Length, mm
    ring.YoungsMod = 200 % Young's modulus, GPa
    ring.GaugeChannel = 3; % Oscilloscope channel
    ring.GaugeFactor = 120; % Gauge factor
    ring.GaugeAmp = 1;  % Signal amplification
    ring.GaugeVoltage = 5; % Signal voltage, V

    % ------------------------------------------------- %
    %                     RAW DATA                      %
    rawData = dlmread(rawFile, ';',10,0); % Read the csv file
    timestep = rawData(2,1) - rawData(1,1); % Time step, s
    inBar.GaugeSignal = rawData(:,inBar.GaugeChannel+1); %V
    outBar.GaugeSignal = ...
        rawData(:,outBar.GaugeChannel+1); %V
```

```
% ------------------------------------------------ %
%                  AXIAL PROCESSING                %
% Strains
inBar.GaugeZero = mean(inBar.GaugeSignal(1:1000));   ...
    % Mean input bar "no signal" voltage, V
outBar.GaugeZero = mean(outBar.GaugeSignal(1:1000)); ...
    % Mean output bar "no signal" voltage, V
inBar.Strain = (inBar.GaugeSignal - ...
    inBar.GaugeZero)*2 / (inBar.GaugeFactor * ...
    inBar.GaugeVoltage * inBar.GaugeAmp);
outBar.Strain = (outBar.GaugeSignal - ...
    outBar.GaugeZero)*2 / (outBar.GaugeFactor * ...
    outBar.GaugeVoltage * outBar.GaugeAmp);

% Detect stress waves
triggerStrain = 0.0001; % Absolute strain indicating ...
    start of a pulse
zeroStrain = 0.00001; % Absolute strain for "zero" ...
    envelope

incidentTrigger = find(abs(inBar.Strain) > ...
    triggerStrain, 1); % Find when signal first larger ...
    than triggerStrain;
if inBar.Strain(incidentTrigger) < 0 inBar.Strain = ...
    -inBar.Strain; end % If incident wave is negative, ...
    invert signal.
incidentStart = ...
    find((inBar.Strain(1:incidentTrigger-1) .* ...
    inBar.Strain(2:incidentTrigger)) < 0, 1, 'last'); ...
    % Find last change of sign before trigger (start ...
    of incident pulse);
incidentEnd = ...
    find((inBar.Strain(incidentStart+1:end-1) .* ...
    inBar.Strain(incidentStart+2:end)) < 0, 1) + ...
    incidentStart; % Find the next change of sign ...
    after trigger (end of incident pulse);
incidentLength = incidentEnd - incidentStart; % ...
    Length of the incident pulse

reflectedTrigger = ...
    find(abs(inBar.Strain(incidentEnd:end)) > ...
    triggerStrain, 1) + incidentEnd - 1; % Find when ...
    signal next has a value larger than triggerStrain;
reflectedStart = ...
    find(abs(inBar.Strain(incidentEnd:reflectedTrigger)) ...
    < zeroStrain, 1, 'last') + incidentEnd -1; % Find ...
    the last "zero" before the trigger (start of ...
    reflected pulse)
```

```
reflectedEnd = ...
    find((inBar.Strain(reflectedStart+1:end-1) .* ...
    inBar.Strain(reflectedStart+2:end)) < 0, 1) + ...
    reflectedStart; % Find the next change of sign ...
    after the trigger (end of reflected pulse);

transmittedTrigger = find(abs(outBar.Strain) > ...
    triggerStrain, 1); % Find when signal first has a ...
    value larger than triggerStrain;
if outBar.Strain(transmittedTrigger) < 0 ...
    outBar.Strain = -outBar.Strain; end; % If ...
    transmitted wave is negative, invert signal.
transmittedStart = ...
    find(abs(outBar.Strain(1:transmittedTrigger)) < ...
    zeroStrain, 1, 'last'); % Find the last "zero" ...
    before the trigger (start of transmitted pulse)
transmittedEnd = ...
    find((outBar.Strain(transmittedStart+1:end-1) .* ...
    outBar.Strain(transmittedStart+2:end)) < 0, 1) + ...
    transmittedStart; % Find the next change of sign ...
    after trigger (end of transmitted pulse);

signalcutoff = max(reflectedEnd,transmittedEnd) + ...
    incidentLength;
N = 20000; % Desired length of FFT input (pulse + ...
    zero padding)
signalcutoff = max(signalcutoff, N);

% Create signalcutoff-length stress waves
inBar.Incident = [zeros(1,incidentStart-1) ...
    inBar.Strain(incidentStart:incidentEnd)' ...
    zeros(1,signalcutoff-incidentEnd)];
inBar.Reflected = [zeros(1,reflectedStart-1) ...
    inBar.Strain(reflectedStart:reflectedEnd)' ...
    zeros(1,signalcutoff-reflectedEnd)];
outBar.Transmitted = [zeros(1,transmittedStart-1) ...
    outBar.Strain(transmittedStart:transmittedEnd)' ...
    zeros(1,signalcutoff-transmittedEnd)];

% Dispersion-corrected stresses and strains
% (see documentation for dispersion.m)
[inBar.incidentStrain inBar.incidentStress] = ...
    dispersion(inBar.Incident, 1/timestep, ...
    inBar.Diameter/2000, inBar.WaveSpeed, ...
    inBar.WaveSpeed^2 * inBar.Density/10^9, ...
    inBar.GaugeOffset/1000);
[inBar.reflectedStrain inBar.reflectedStress] = ...
    dispersion(inBar.Reflected, 1/timestep, ...
    inBar.Diameter/2000, inBar.WaveSpeed, ...
```

```
    inBar.WaveSpeed^2 * inBar.Density/10^9, ...
    -inBar.GaugeOffset/1000);
[outBar.transmittedStrain outBar.transmittedStress] = ...
    dispersion(outBar.Transmitted, 1/timestep, ...
    outBar.Diameter/2000, outBar.WaveSpeed, ...
    outBar.WaveSpeed^2 * outBar.Density/10^9, ...
    -outBar.GaugeOffset/1000);

% Specimen stresses and strains
trigger = ...
    find(abs(inBar.incidentStrain)>triggerStrain,1); % ...
    Find new position of incident pulse
go = find((inBar.incidentStrain(1:trigger-1) .* ...
    inBar.incidentStrain(2:trigger)) < 0, 1, 'last'); ...
    % Find last change of sign before  trigger (start ...
    of incident pulse)
stop = find((inBar.incidentStrain(go+1:end-1) .* ...
    inBar.incidentStrain(go+2:end)) < 0, 1) + go; % ...
    Find next change of sign after trigger (end of ...
    incident pulse)

inBar.incidentStrain = inBar.incidentStrain(go:stop);
inBar.reflectedStrain = inBar.reflectedStrain(go:stop);
outBar.transmittedStrain = ...
    outBar.transmittedStrain(go:stop);
inBar.incidentStress = inBar.incidentStress(go:stop);
inBar.reflectedStress = inBar.reflectedStress(go:stop);
outBar.transmittedStress = ...
    outBar.transmittedStress(go:stop);

sample.FrontStress = inBar.incidentStress + ...
    inBar.reflectedStress; % Stress at incident bar ...
    specimen face, MPa
sample.BackStress = outBar.transmittedStress; % ...
    Stress at transmitter bar specimen face, MPa
sample.MidStress = (sample.FrontStress + ...
    sample.BackStress)/2; % Mean axial specimen ...
    stress, MPa

% Bar displacements, sample strains
inBar.Displacement(1) = 0;
outBar.Displacement(1) = 0;
for i=2:stop-go+1
    inBar.Displacement(i) = inBar.Displacement(i-1) + ...
        ((inBar.incidentStrain(i)-inBar.reflectedStrain(i)) ...
        * 1000 * timestep * inBar.WaveSpeed); % ...
        Cumulative input bar displacement, mm
    outBar.Displacement(i) = outBar.Displacement(i-1) ...
        + (outBar.transmittedStrain(i) * 1000 * ...
```

```
        timestep * outBar.WaveSpeed); % Cumulative ...
        output bar displacement, mm
    sample.Strain(i) = (inBar.Displacement(i) - ...
        outBar.Displacement(i)) / ...
        sample.InitialLength; % Sample axial strain
end
sample.Length = (1 - sample.Strain) * ...
    sample.InitialLength; % Sample length

% Sample axial strain rate
relTime = timestep*(0:stop-go); % Relative time, s
sample.StrainRate = zeros(2,length(sample.Strain));
for i = 1:length(sample.Strain)-1
    sample.StrainRate(1,i) = (relTime(i) + ...
        relTime(i+1)) / 2;
    sample.StrainRate(2,i) = ((sample.Length(i) - ...
        sample.Length(i+1)) / sample.Length(i)) / ...
        timestep;
end

% ------------------------------------------------- %
%                  RADIAL STRESSES                  %
sample.InitialVolume = sample.InitialLength * pi() * ...
    (inBar.Diameter/2)^2*10^-3; % Sample initial ...
    volume, cm^3
ring.GaugeSignal = rawData(1:N, ...
    ring.GaugeChannel+1)'; % Confining ring signal, V

[maxval maxloc] = max(abs(ring.GaugeSignal));
if ring.GaugeSignal(maxloc) < 0; ring.GaugeSignal = ...
    -ring.GaugeSignal; end; % If signal is negative, ...
    flip it
ring.GaugeZero = mean(ring.GaugeSignal(1:1000));
sample.RadialStrain = (ring.GaugeSignal(go:stop) - ...
    ring.GaugeZero)*4 / (ring.GaugeFactor * ...
    ring.GaugeVoltage * ring.GaugeAmp);

ring.ThickWalledPipeFactor = ...
    ((ring.OutsideDiameter/2)^2 - ...
    (ring.InsideDiameter/2)^2) / ...
    (2*(ring.InsideDiameter/2)^2); % Ratio of internal ...
    radial stress on the specimen to circumferential ...
    stress in the ring
sample.RadialStress = (ring.ThickWalledPipeFactor * ...
    (ring.YoungsMod*1000) * sample.RadialStrain) .* ...
    (ring.Length./sample.Length); % Radial stress from ...
    ring, MPa
```

```
    sample.Volume = sample.InitialVolume * ...
        (1-sample.Strain); % Soil sample volume, cm^3
    sample.Density = sample.Mass./sample.Volume; % Sample ...
        density, Mg/m^3
    sample.DryDensity = sample.DryMass./sample.Volume; % ...
        Sample dry density, Mg/m^3

    % ------------------------------------------------- %
    %                     SAVE DATA                     %
    dataDir = 'Data'; % Directory to save .mat file ...
        (relative to raw data)

    % Create save directory, if necessary
    [filePath, fileName, fileExt] = fileparts(rawFile);
    if isdir(fullfile(filePath, dataDir)) == 0
        mkdir(fullfile(filePath, dataDir));
    end

    % Save data
    save (fullfile(filePath, dataDir, fileName), ...
        'relTime', 'inBar', 'outBar', 'sample', 'ring', ...
        'rawFile');
end
```

**Appendix B**

# LS-DYNA material cards

## B.1 Introduction

This appendix contains the LS-DYNA material cards used in the evaluation of the models *Soil and Foam*, *Pseudo-Tensor* and *Mohr–Coulomb*. The calibration and validation of these models are presented in §6.4.

## B.2 Soil and Foam

```
*MAT_SOIL_AND_FOAM
$#     mid        ro         g      bulk        a0        a1        a2        pc
         X  1500.000  1.300E+7 2.200E+10     0.000     4.510     0.693     0.000
$#     vcr       ref      lcid
     0.000     0.000         0
$#    eps1      eps2      eps3      eps4      eps5      eps6      eps7      eps8
     0.000    -0.080    -0.120    -0.160    -0.200    -0.240    -0.280    -0.320
$#    eps9     eps10
    -0.360    -0.400
$#      p1        p2        p3        p4        p5        p6        p7        p8
     0.000  6.000E+6  1.200E+7  2.100E+7  3.600E+7  5.600E+7  8.600E+7  1.320E+8
$#      p9       p10
  2.070E+8  3.200E+8
```

**Table B.1:** Material card for *Soil and Foam*, calibrated for use with medium sand. (See §6.5.1)

## B.3 Pseudo-Tensor

```
*MAT_PSEUDO_TENSOR
$#     mid        ro         g        pr
         X  1500.000 6.3850E+7      0.32
$#    sigf        a0        a1        a2       a0f       a1f        b1       per
       1E0
$#      er       prr      sigy      etan       lcp       lcr
     0.000     0.000     0.000     0.000         0         0
$#      x1        x2        x3        x4        x5        x6        x7        x8
     0.000   3.80E+8
$#      x9       x10       x11       x12       x13       x14       x15       x16

$#     ys1       ys2       ys3       ys4       ys5       ys6       ys7       ys8
     0.000   5.70E+8
$#     ys9      ys10      ys11      ys12      ys13      ys14      ys15      ys16
```

```
*EOS_TABULATED_COMPACTION
$#   eosid            gama              e0              vo
         X           0.000           0.000        1.000000
$#     ev1             ev2             ev3             ev4             ev5
     0.000           -0.08           -0.12           -0.16           -0.20
$#     ev6             ev7             ev8             ev9            ev10
     -0.24           -0.28           -0.32           -0.36           -0.40
$#      c1              c2              c3              c4              c5
     0.000       6.000E+6        1.200E+7        2.100E+7        3.600E+7
$#      c6              c7              c8              c9              c1
  5.600E+7        8.600E+7        1.320E+8        2.070E+8        3.200E+8
$#      t1              t2              t3              t4              t5
     0.000           0.000           0.000           0.000           0.000
$#      t6              t7              t8              t9             t10
     0.000           0.000           0.000           0.000           0.000
$#      k1              k2              k3              k4              k5
  0.126E+9        1.127E+9        3.178E+9        5.060E+9        7.303E+9
$#      k6              k7              k8              k9             k10
  9.597E+9       19.599E+9       23.855E+9       57.363E+9       60.127E+9
```

**Table B.2:** Material card for *Pseudo-Tensor* and the *Tabulated Compaction* EOS, calibrated for use with medium sand. (See §6.5.2)

## B.4 Mohr–Coulomb

```
*MAT_MOHR_COULOMB
$#     mid        ro      gmod       rnu                phi      cval       psi
         X  1500.000  1.300E+7     0.320              0.639     0.000       0.0
$#           nplanes             lccpdr     lccpt    lccjdr     lccjt    lcsfac
                   0                  0         0         0         0         0
$#  gmoddp    gmodgr    lcgmep   lcphiep   lcpsiep   lcgmst   cvalgr     aniso
       0.0       0.0      0.00       0.0       0.0       0.0       0.0       1.0
$#     dip    dipang    cplane   frplane    tplane    shrmax    local
       0.0       0.0       0.0       0.0       0.0       0.0       0.0
```

**Table B.3:** Material card for *Mohr–Coulomb*, calibrated for use with medium sand. (See §6.5.3)

**Appendix C**

# Stress spaces and invariants

## C.1 Introduction

This appendix contains derivations of the stress spaces and invariants used to define material behaviour in LS-DYNA constitutive models. An overview of the models and the stress spaces used can be found in Table 6.2.

## C.2 Volumetric stress

$P$, $p$ and $I_1$ are measures of the volumetric part of the stress tensor $\boldsymbol{\sigma}$, such that

$$P = p = I_1/3. \tag{C.1}$$

$P$ and $p$ are equivalent measures of pressure, or mean normal stress,

$$P = p = \frac{\sigma_1 + \sigma_2 + \sigma_3}{3} \tag{C.2}$$

where $\sigma_1$, $\sigma_2$ and $\sigma_3$ are the major, intermediate and minor principal stresses, respectively. $p$ is often used in geotechnical engineering when $\sigma_2 = \sigma_3$ and the equation takes the form

$$p = \frac{\sigma_1 + 2\sigma_3}{3} \tag{C.3}$$

$I_1$ is the first basic invariant, or trace, of the stress tensor,

$$I_1 = \mathrm{tr}(\boldsymbol{\sigma}) = \sigma_1 + \sigma_2 + \sigma_3. \tag{C.4}$$

## C.3 Deviatoric stress

$J_2$, $J_3$, $q$ and $\tau$ are measures of the deviatoric part of the stress tensor, and are used to define shear strength. The deviatoric invariants $J_2$ and $J_3$ are defined with reference to the deviatoric tensor $\boldsymbol{s}$:

$$\boldsymbol{s} = \boldsymbol{\sigma} - \sigma_v \boldsymbol{\delta} \tag{C.5}$$

where $\sigma_v = I_1/3$ and $\boldsymbol{\delta}$ is the Kronecker delta. They are defined as

$$J_2 = \frac{1}{2}(s_1^2 + s_2^2 + s_3^2) \tag{C.6}$$

and

$$J_3 = s_1 s_2 s_3. \tag{C.7}$$

The deviator stress $q$ is preferred in geotechnical engineering and, when $\sigma_2 = \sigma_3$, is defined as the stress difference $q = \sigma_1 - \sigma_3$. In more general cases, it takes the form

$$q = \sqrt{\frac{(\sigma_1 - \sigma_2)^2 + (\sigma_2 - \sigma_3)^2 + (\sigma_3 - \sigma_1)^2}{2}} = \sqrt{3J_2}. \tag{C.8}$$

The shear stress $\tau$ is also used in geotechnical engineering problems, and where $\sigma_2 = \sigma_3$,

$$\tau = \frac{\sigma_1 - \sigma_3}{2}. \tag{C.9}$$